NAWI Graz
Natural Sciences

TU Graz

Evaluation of the utility of radio occultation data for monitoring the Hadley cell under climate change

Annika Reiter, BSc

MASTER'S THESIS

to achieve the university degree of
Master of Science

Master's degree programme:
Environmental System Sciences / Climate Change and Environmental Technology

submitted to
Graz University of Technology

Supervisor
Mag. Dr.rer.nat. Julia Danzer
Wegener Center for Climate and Global Change
University of Graz, Austria

Graz, May 2024

Abstract

Research generally agrees that the Hadley cell circulation has and will continue to expand poleward due to anthropogenic climate change and increased atmospheric greenhouse gases. Radio occultation (RO) provides a promising dataset to analyze the Hadley cell, using different metrics to determine its latitudinal edges and their change over recent decades. This thesis focuses on exploring the possible added value of RO data in this context, thereby considering its limited record length of less than 15 years. The present work examines the time changes of the Hadley cell based on the eddy drive jet (EDJ) metric and two tropopause break (TPB) metrics. A focus is set on the seasonal cycle and the decadal trend, which indicates an equatorward shift of the latitudinal edges for the investigated 15-year period in both hemispheres. This trend is contrary to previous studies. The findings of the RO dataset are compared with ERA5 reanalysis data of the same length, and additionally, with a longer record from 1980 to 2022. The results of the metrics correlate well for the shorter 15-year period and the trend results for the two datasets are consistent. However, for the long period of ERA5, the trend values do not agree. An investigation of rolling trends shows stronger trends for shorter time windows and suggests that the trend of the Hadley cell change does not emerge from natural variability during the limited length of the RO record. A second line of investigation explored a multiple linear regression model to remove possible influences of natural variability and ozone changes from the Hadley cell trend. In this study, natural variability indices were included for the El Niño-Southern Oscillation (ENSO) and the Pacific Decadal Oscillation (PDO). The results remain inconclusive on the trends, although the trend for the northern hemisphere suggests that the Hadley cell has narrowed over recent decades and thus the global warming trend is still concealed by other influences.

Kurzzusammenfassung

Die Wissenschaft ist sich generell einig, dass sich die Hadley-Zelle zu den Polen hin ausgedehnt hat und sich weiter ausdehnen wird, aufgrund des anthropogenen Klimawandels und der Zunahme von Treibhausgasen in der Atmosphäre. Ein vielversprechender Datensatz, mit dem man die Hadley-Zelle analysieren kann, stammt von der Radio-Okkultations (RO) Methode. Anhand der RO-Daten können mittels verschiedener Metriken die latitudinalen Ränder der Hadley-Zelle und deren Veränderungen über die letzten Jahrzehnte bestimmt werden. Der Fokus dieser Arbeit liegt dabei speziell auf dem Mehrwert, den die RO-Daten in diesem Zusammenhang bieten können. Darüber hinaus wird die zeitlich begrenzte Aufzeichnungsdauer der RO-Daten, von weniger als 15 Jahren, kritisch betrachtet. Die vorliegende Arbeit untersucht die Zeitreihen der Hadley-Zelle auf der Basis der Polarfront-Jet-Metrik (Eddy Drive Jet, EDJ) und zweier Tropopausen-Metriken (Tropopause Break, TPB). Im Mittelpunkt stehen dabei der Jahresgang und der dekadische Trend, der für den Untersuchungszeitraum von 15 Jahren eine äquatoriale Verschiebung der Zirkulationsränder beider Hemisphären anzeigt. Dieser Trend steht im Widerspruch zu früheren Studien. Die Ergebnisse des RO-Datensatzes werden mit ERA5-Reanalysedaten der gleichen Zeitlänge und zusätzlich mit dem längeren ERA5 Datensatz von 1980 bis 2022 verglichen. Die Ergebnisse der Metriken korrelieren gut für den kürzeren Untersuchungszeitraum und die Trendergebnisse für beide Datensätze sind konsistent. Für die gesamte ERA5-Länge zeigen die Trendwerte jedoch ein anderes Ergebnis, das den früherer Studien entspricht. Eine weitere Untersuchung dieser Arbeit, betrachtet gleitende Trends. Diese zeigen, dass für kürzere Zeitfenster der Trend stärker ist. Das deutet darauf hin, dass der Trend der Hadley-Zellenveränderung für die begrenzte Länge der RO-Aufzeichnung, nicht aus der natürlichen Variabilität hervorgeht. Eine weitere Untersuchungsrichtung dieser Arbeit betrachtet ein multiples lineares Regressionsmodell. Dieses soll mögliche Einflüsse der natürlichen Variabilität und des stratosphärischen Ozon Verlustes aus dem Trend der Hadley-Zelle entfernen. Dafür werden Indizes der natürlichen Variabilität für die El Niño-Southern Oscillation (ENSO) und die Pazifische Dekaden-Oszillation (PDO) gewählt. Die Ergebnisse der Analyse sind nicht eindeutig. Dennoch deutet der Trend für die Nordhemisphäre daraufhin, dass sich die Hadley-Zelle in den letzten Jahrzehnten zusammengezogen hat und der globale Erwärmungstrend durch andere Einflüsse überlagert wird.

Acknowledgments

First of all, I would like to express my deepest gratitude to Mag. Dr. Julia Danzer. She was the best supervisor for my thesis and without her this process would not have been the same. I would like to thank her sincerely for the initial suggestion of the topic and the great opportunity to work on a funded master's thesis at the Wegner Center for Climate and Global Change. I appreciate the warm welcome in the office and all the constructive feedback. In this respect, I would also like to thank the StratoClim group, and especially Univ.-Prof. Dr. Gottfried Kirchengast, for the helpful discussions and advice that contributed to the development of my research.

A special thanks goes to my family and friends, without whom my studies would not have been possible. I would also like to recognize some of the best fellow students I could have wished for - thank you for the wonderful years at university and beyond!

Last but not least, I would like to thank my husband Johannes for supporting me in everything I do. Thank you especially for all the detailed discussions we had on our daily dog walks during this writing process.

Contents

List of acronyms

AO	Arctic Oscillation
CFCs	Chlorofluorocarbons
DJF	December, January, February (boreal winter, austral summer)
ECMWF	European Centre for Medium-Range Weather Forecasts
EDJ	Eddy Driven Jet
ENSO	El Niño – Southern Oscillation
ERA5	ECMWF Reanalysis Version 5
GHG	Greenhouse Gases
GNSS	Global Navigation Satellite System
ITCZ	Intertropical Convergence Zone
JJA	June, July, August (boreal summer, austral winter)
KNMI	Royal Netherlands Meteorological Institute
MAM	March, April, May (boreal spring, austral autum)
MEI	Multivariate ENSO Index
NH	Northern Hemisphere
OLS	Ordinary Least Squares
OMD	Ozone Mass Deficit
OPSv5.6	Occultation Processing System version 5.6
PDO	Pacific Decadal Oscillation
PSI	Mean meridional mass stream function
RO	Radio Occultation
SH	Southern Hemisphere
SOI	Southern Oscillation Index

SON	September, October, November (boreal autumn, austral spring)
SST	Sea Surface Temperature
STJ	Subtropical Jet
TPB	Tropopause Break
TropD	Tropical-width Diagnostics code package
UTLS	Upper Troposphere Lower Stratosphere
WEGC	Wegener Center for Climate and Global Change

1 Introduction

According to observations, reanalyses and climate models, the Hadley cell circulation has been and will continue to expand poleward due to anthropogenic climate change and the increase in greenhouse gases in the atmosphere (e.g., Chemke and Polvani, 2019; Davis and Rosenlof, 2012; Grise et al., 2019; Hu et al., 2018; Staten et al., 2018; Waugh et al., 2018). This widening will possibly alter the water cycle and temperature patterns of subtropical regions, where the subsidence branches of the Hadley circulation are located and consequently can threaten the livelihoods of people living in these areas (see e.g., Xian et al., 2021).

Global Navigation Satellite System (GNSS) radio occultation (RO) data provides long-term stable, multi-satellite vertical profiles of atmospheric variables such as, temperature and geopotential height. The RO method has all weather capability and supplies data with high accuracy, high vertical resolution as well as global coverage for the upper troposphere lower stratosphere region. Also, the continuation of the RO record is ensured by recently launched and prospective satellite missions. Thus, RO presents a powerful complementary data source for the analysis of climate variables (e.g., Angerer et al., 2017; Steiner et al., 2020). Wind field data can be derived from RO geopotential height fields on isobaric levels, via the geostrophic, gradient and equatorial balance approximations (Danzer et al., 2023; Nimac et al., 2024). In turn, all this information allows for various latitudinal edge-metrics of the Hadley cell to be calculated and analyzed (e.g., Davis and Birner, 2013).

Over the past 20 years, RO data have been already used to study how the Hadley cell circulation has transformed with climate change. Different metrics such as the eddy driven jet (EDJ), subtropical jet (STJ) or the tropopause break (TPB) have been utilized and compared to gain some insight. However, the results of the Hadley cell change are mixed for these previous studies and some of their trend results are in disagreement. Widening, as well as narrowing trends have been found for different record lengths and time periods over the first two decades of this century. Additionally, the magnitude of the detected trends can vary considerably (e.g., Ao and Hajj, 2013; Darrag et al., 2022; Davis and Birner, 2013; Luan et al., 2020). Thus, some results are contradicting the long-term trend and results from climate models. While there has been research suggesting that the record period for RO is not long enough (e.g., Luan et al., 2020), little focus was laid on studying what record length would suffice or how to remove natural variability to allow for a trend signal to emerge.

Hence, this thesis aims to investigate the changes of the latitudinal Hadley cell extent within the recent two decades based on RO data. Moreover, the objectives of this work are to (i) establish trend estimates for this particular record, (ii) study the influence of the chosen length of time period, (iii) aim to remove natural variability from the time series, (iv) explore whether the Hadley cell has a clear climate change signal, and to (v) evaluate the possible added value from RO data for this line of research. A comprehensive time series analysis of the monthly-mean RO OPSv5.6 data available for the period September 2006 to November 2020 is done, and a comparison to the ERA5 reanalysis is made. A rolling trend is computed, in order to visualize the impact of the selected time period including its start and end date and overall length. This information is highly interesting for the comparison of shorter records of less than 20 years, such as it is the case for the RO record used here. In addition, a multiple linear regression analysis was done, aiming to remove the influence of natural variability and possibly improve the stability of the calculated trend from these shorter time periods.

The thesis begins, in Chapter 2, with a brief theoretical basis for why the Hadley cell changes and a general overview of metrics used to determine the Hadley cell change. The next section, Chapter 3, focuses on the data and methods. The main dataset of this thesis, WEGC RO OPSv5.6 data, and the complementary ERA5 reanalysis dataset are presented, and indices of natural variability and external forcing affecting the latitudinal width of the circulation are discussed. This chapter also introduces the methods, including the selection and application of the Hadley cell latitudinal edge metrics, along with the methodology of the trend analysis, correlation analysis and multiple linear regression analysis. Chapter 4 presents the results of the detailed investigations. First, a time series analysis of the RO and ERA5 data is performed, including the seasonal cycle and the long-term trend in the Hadley cell's northern and southern latitudinal edges as well as in its overall interhemispheric width. In a next step, the results from the two datasets are compared and the trend significance for the time periods under consideration is examined in more detail. Finally, a multiple linear regression analysis is applied aiming to remove the natural variability and the influence of ozone changes from the time series. This is done in an attempt to improve the stability of the overall trend analysis and the comparability of shorter and longer data records. In this context, also the indices are inspected more closely and the correlation with the individual metrics is evaluated. Summary and conclusions of the thesis are given in Chapter 5.

2 Hadley cell

The Hadley cell describes the thermally direct mean meridional circulation. The circulation consists of rising air at the equator, which then moves poleward in the upper branches of the circulation cell, a subsidence branch in the subtropics and a return flow of air close to the surface. Initially, this motion was explained by axisymmetric theory. It was assumed that the width and total polar heat flux of the cell was constrained by angular momentum conservation and the conservation of potential temperature (Held and Hou, 1980). However, more recent findings have discovered axisymmetric theory to be incomplete, as the angular momentum flux is not ideally conserved by the poleward motion. Instead, the strength and extent of the Hadley cell is influenced by eddy momentum fluxes, reducing the Rossby numbers of the poleward branch (Schneider, 2006). Davis et al. (2016) elaborated further, that the Hadley cell edge variability is driven by changes in the static stability and properties of the eddy fluxes. The topic will be further discussed in Chapter 3.2.1 in the subsections eddy driven jet and subtropical jet.

The Hadley cell circulation has an annual cycle, where the cell located in the winter hemisphere is more pronounced than the one in the summer hemisphere and symmetry of the circulation can only be identified during the transitional months of October, November and April, May (Oort and Rasmusson, 1970). Dima and Wallace (2003) further describe that the annual cycle can be characterized by two components. The first consists of two seasonally invariant cells, with rising motion at the equator and sinking air in the subtropics. The second component depicts a single cell that varies in a sinusoidal manner, with a seasonally reversing pattern, where rising motion happens in the outer tropics of the summer hemisphere and sinking movement in the outer tropics of the winter hemisphere.

Also the year-to-year variability of the Hadley cell can be described by its symmetrical behavior. The two states are discussed by studies as the equatorial asymmetric and equatorial symmetric mode, representing the two principal components of the interannual variability of the Hadley cell. Interestingly, the predominant principal mode is the asymmetric mode and thus the principal mode is not determined by the climatological mean structure of the Hadley cell, which resembles two symmetric cells on either side of the equator (Feng et al., 2013; Guo and Tan, 2018a; Ma and Li, 2008). Both modes are strongly correlated with ENSO (e.g., Guo and Tan, 2018a), which will be further discussed in the according subchapter of the following section.

A multitude of studies show a poleward expansion of the Hadley cell circulation over the past decades for different datasets and metrics (e.g., Ao and Hajj, 2013; Davis and Birner, 2013; Davis and Rosenlof, 2012; Mantsis et al., 2017; Seidel and Randel, 2007), additionally these and other results have been thoroughly reviewed in synthesis papers such as e.g., Grise et al. (2019), Hu et al. (2018), Staten et al. (2018). Climate models suggest that this expansion will continue as a result of greenhouse gas (GHG) emissions and concomitant global warming, agreeing with the underlying theoretical understanding (Chemke and Polvani, 2019; D'Agostino et al., 2017; Kim et al., 2017; Waugh et al., 2018).

The changes of the Hadley cell circulation extent are of consequence for the human population as summarized by Xian et al. (2021). In connection with the widening of the Hadley cell, the storm tracks intensify and move pole- and upward, as the mid latitudinal weather systems have the tendency to follow the jet. This, in turn, leads to a change in the hydrological cycle, with less precipitation in the subtropical regions, as the precipitation and the temperature patterns are affected. As a result, subtropical dry zones and desert regions are expected to expand and shift poleward, potentially threatening the livelihoods of the large number of people living in these areas. Moreover, the implication of the Hadley cell circulation change extends beyond the subtropics, with an expected increased intensity and frequency of wildfires, droughts, and heat waves in the midlatitudes. Other consequences include the expansion and poleward shift of marine areas with increased salinity and low bio-productivity, such as in the Mediterranean or the western Pacific.

2.1 Reasons of Hadley cell change

There are many different factors influencing the Hadley cell width, such as external forcings like stratospheric ozone depletion, GHGs, aerosols or volcanic eruptions (e.g., Dogar, 2018; Min and Son, 2013; Zhao et al., 2020). But there is also an important attribution from modes of natural variability, such as El Niño-Southern Oscillation (ENSO), the Pacific Decadal Oscillation (PDO), or the Arctic Oscillation (AO) for instance (e.g., Rollings and Merlis, 2021; Seo et al., 2023). This work wants to focus on the human induced changes of the circulation. However, for shorter record periods of about 20 years, such as available for RO data, those trends can be concealed by the various external forcings and the natural variability. Thus, this subchapter aims to qualitatively assess the most important attributions to the Hadley cell circulation change of the past decades and will consider each in more detail to build a knowledge foundation for the following trend analyses.

2.1.1 External forcings

Results from climate models attribute parts of the Hadley cell expansion to external forcings, as has been mentioned above. Yet, to establish a clear trend of anthropogenically forced changes in observational data is difficult and the findings differ for each hemisphere (Grise et al., 2019).

Numerous external forcings attributing to the widening of the Hadley cell have been found and summarized (e.g., Staten et al., 2018; Xian et al., 2021), the most prominent ones will be discussed in the following segment.

Greenhouse gases

Since the industrial revolution, around 1750, a huge increase in well mixed GHGs in the atmosphere is apparent. The rise in the GHG concentration can be attributed to human actions, for example the burning of fossil fuels and industrial production and has led to changes in the climate system. GHGs, like CO_2 or CH_4 are infrared active gases, which contribute to the greenhouse effect. Therefore, when we humans increase their concentration in the atmosphere, we are inevitably causing global warming followed by other consequences of climate change. For example, anthropogenic CO_2 emissions over the period 1850 to 2019 sum up to a total of about 2390 ±240 Gt CO_2, which have preceded in an atmospheric CO_2 concentration of 410 ppm (parts per million) and a temperature increase of about 1°C (IPCC, 2021).

Despite the fact that studies from reanalysis and model data agree on a general widening of the Hadley cell with increasing GHGs, the mechanisms and theory behind this expansion are not fully understood and multiple explanations exist (Davis and Birner, 2022; Staten et al., 2018). A study by Davis and Birner (2022) finds, that the radiative-convective equilibrium temperature response, forces an axisymmetric increase of angular momentum in the subtropics, which shifts the eddy stresses poleward and thus causes an expansion of the Hadley cell. They further find that eddies do not force changes of angular momentum, but instead dampen it. Also, baroclinic instability is not the driver of widening the circulation.

Nonetheless, the influence of GHGs extends beyond the temperature response of the atmosphere. Climate change is causing increased sea surface temperature (SST), this in turn also effects the Hadley circulation. Adam et al. (2014) found, that the Hadley cell extent is sensitive to variations in global warming via large-scale mean SST and the SST gradient of the midlatitudes and tropics. The cell widens for SST increase and a weakening of the meridional temperature gradient, comparable to La Niña conditions. Zhou et al. (2020) showed the importance of the underlying patterns of SST. They investigated the sensitivity of SST patterns and found, that the Hadley cell is expanding for a SST increase in the equatorial region, and narrowing for an increase in the tropical regions, excluding the western Pacific and Indian ocean. In comparison, the Hadley cell is much less affected by SST changes in the high latitudes. Furthermore, they analyzed the strength response of the circulation and found that strengthening of the Hadley circulation is induced by SST increase in the ascending regions, near the intertropical convergence zone (ITCZ). Contrary, an increase in SST in the subsidence regions, over the subtropics, leads to a weakening of the circulation. Long

term changes of the SST patterns are consistent with shorter pattern changes like ENSO (Zhou et al., 2020, 2019).

Stratospheric ozone

The Antarctic ozone hole developed due to anthropogenic emissions of ozone depleting substances, like chlorofluorocarbons (CFCs). Consequently, their usage got restricted by the 1987 Montreal Protocol and substituting substances were created, leading to a stabilization of the CFC concentration in the atmosphere in the late 1990s (World Meteorological Organization, 2022). Ozone recovery has been a slow process, nevertheless it has been steady since the new millennia (de Laat et al., 2017). By now, first signs of ozone recovery are detectable, which can be very interesting for the attribution of the Hadley cell edge trend (World Meteorological Organization, 2022).

The ozone hole does not only have an effect in the polar regions, but also influences the tropics. Kang et al. (2011) show, that ozone depletion and the consequent cooling of the lower stratosphere, have resulted in a higher tropopause at the poles and an accompanying poleward displacement of the midlatitude jet. Hu et al. (2018) further elaborate the poleward shift of the jet stream. Due to the increased meridional temperature gradient, the extratropical westerly winds accelerate, leading to faster moving baroclinic eddies in the upper troposphere. The higher phase speed prohibits the eddies to reach as far equatorward, causing a poleward shift of the transient eddy momentum flux and the eddy driven jet. In this regard, the poleward shift of the Hadley cell edge can be connected with ozone depletion and its current recovery, especially on the southern hemisphere (Hu et al., 2018; Kang et al., 2011; Kang and Polvani, 2011; Son et al., 2010).

More precisely, authors like Min and Son (2013) have separated the signal of stratospheric ozone depletion from GHGs attributing to the observed expansion of the southern Hadley cell during the austral summer season, December-January-February (DJF). Therefore, as stratospheric ozone levels recover, the effect of GHGs may be completely concealed in the first half of this century. Contrary, the trends of the southern hemisphere during the second half of the twentieth century have been dominated by the impact of ozone depletion (Polvani et al., 2011a). This information is highly important for the comparison of trends derived from different datasets and diverging time spans, as planned to be analyzed in this thesis.

Complementary to the research of the southern hemisphere, only little information is available on the possible connection of the stratospheric ozone of the northern hemisphere. Hu et al. (2019a) investigated the influence of the artic stratospheric ozone on the northern Hadley cell and found that a anticorrelated relationship exists on interannual time scales.

Lastly, also the relationship between the Hadley circulation and tropospheric ozone concentration in the southern hemisphere has been under investigation in current literature. The expansion of the Hadley cell and its strengthening subsidence branch in the southern hemisphere have caused an increased transport of stratospheric ozone into the troposphere. Additionally, the circulation lifts ozone precursors in the tropics into the upper troposphere, thereby enhancing the tropospheric production of ozone. Both processes increase the concentration of tropospheric ozone in the extratropics of the southern hemisphere. This poses as a potential positive feedback loop, where tropospheric ozone amplifies global warming and this in turn attributes to the Hadley cell circulation change. Records highlight the increase of tropospheric and surface ozone since the 1990s (Lu et al., 2019).

Volcanic eruptions

Very large volcanic eruptions can release great amounts of volcanic aerosols, which cool the troposphere and warm the lower stratosphere. This in turn decreases the height of the tropopause (Santer et al., 2003), and thus leads to a contraction of the Hadley cell width (Lu et al., 2009; Lucas et al., 2012).

Regardless of their impact, so far not many studies are available focusing specifically on the effect of volcanic eruptions on the Hadley cell circulation. Dogar (2018) has investigated the post-eruption response of the Hadley cell in the northern hemisphere summer, June-July-August (JJA), with a focus on the rising branch of the circulation. For this region he found that the volcanic aerosol radiative forcing causes a weakening and southward shift of the rising branch. Also, the subtropical jet streams are displaced equatorward, suggesting a possible connection between the Hadley cell and volcanic eruptions.

Ward et al. (2021) found a volcanically induced response of ENSO, which is dependent on the location and distribution of the volcanic aerosols. Aerosols constrained to the southern hemisphere result in anomalies representing La Niña conditions, whereas symmetrically distributed aerosols or aerosols confined to the northern hemisphere produce El Niño like anomaly values. According to the authors, these anomalies are driven by a displacement of the ITCZ due to the volcanic eruption. The effect on ENSO from eruptions lags in time, starting towards the end of the year the eruption occurred and peaking in the subsequent one.

Meng et al. (2021) showed that it can be advantages to remove this variation when analyzing the tropopause height. Similar removal of the natural trend could be of interest for the trend analysis of the Hadley cell width, as two major eruptions, El Chichón in April 1982, and Mount Pinatubo in June 1991, occurred during the available ERA5 record period.

Anthropogenic aerosol pollution

The final external forcing which will be discussed are anthropogenic aerosols. Synthesis papers summarized, that air pollution can affect earths radiation budget, through absorption and scattering of incoming solar radiation by black carbon or sulfate aerosols, respectively (e.g., Staten et al., 2018; Xian et al., 2021). Zhao et al. (2020) further elaborate that black carbon aerosols lead to an expansion of the Hadley cell via an increase in the extratropical static stability, whereas sulfate aerosols cause a decrease of extratropical static stability and thus cause contraction. Aerosols are hence an important driver of changes in the circulation width. Especially in the northern hemisphere, the expansion over recent decades can be attributed to black carbon aerosols, although only with high uncertainty. Additionally to the uncertainty which aerosols, black carbon or sulfate, and concomitant which effect, expansion or contraction, will dominate, aerosols can interact with clouds, making attribution and future projections even more complex (Allen and Ajoku, 2016; Zhao et al., 2020).

2.1.2 Natural variability

ENSO and the PDO are the most prominent modes of natural variability influencing the Hadley cell width on interannual and multidecadal time scales, respectively (Amaya et al., 2018; Mantsis et al., 2017; Rollings and Merlis, 2021). More recent studies highlight the importance of the Arctic Oscillation (AO) on the natural variability of the northern hemisphere Hadley cell extent (Seo et al., 2023), thus this mode will also be explored in the upcoming section.

El Niño-Southern Oscillation

ENSO is an ocean-atmosphere coupled phenomena in the tropical Pacific ocean. It occurs on a multi-year time scale and is characterized by its SST anomalies. Two phases can be distinguished, those are the El Niño and La Niña phase. The El Niño phase is marked by positive SST anomalies, which increase the meridional gradient of tropical SST. Contrary, the La Niña phase, leads to an intensification of the normal SST state, hence cold anomalies occur (Wang et al., 2017).

ENSO is one of the most important modes of natural variability of the climate system and has a significant effect on the global climate via teleconnections. It also has an impact on the Hadley cell. El Niño conditions for example lead to a stronger and narrower cell (Adames and Wallace, 2017; Lu et al., 2008; Nguyen et al., 2013; Schwendike et al., 2014). Interestingly the Hadley cell anomaly is not zonally uniform. Li et al. (2023), found three pairs of subcells during El Niño phases. One pair of cells is located over the central eastern Pacific and shows intensified cell behavior, whereas the cell pairs over the tropical Atlantic and Indo-Pacific showed a weakening. Compatible results were found by Wilhelmsen et al. (2020). The authors investigated the tropopause altitude and found

tropical belt narrowing during La Niña events in the Niño 3 region, so the equatorial east Pacific ocean.

Guo and Tan (2018a, 2018b) found that this impact is present for both the asymmetric mode of the Hadley cell, where one cell across the equator dominates, and the symmetric mode, where two cells flank the equator. In addition, also an opposite effect on El Niño exists. Originating from the asymmetric Hadley cell during the months March-April-May (MAM), and the central equatorial Pacific meridional wind anomaly across the equator, the onset of El Niño can be correlated, according to Li et al. (2023).

Furthermore, different types of ENSO exist. The typical ENSO pattern, also called canonical El Niño, is associated with a symmetric zonal-mean SST anomaly pattern around the equator, where the positive SST anomalies lie in the east Pacific. The second type is named El Niño Modoki. In contrast to the typical El Niño event, the zonal-mean SST anomalies are asymmetric with the maximum displaced at 10°N and warm anomalies located more in the central Pacific, with cold SST on both flanks (Behera and Yamagata, 2018). This in turn leads to a contrasting impact on the Hadley cell, in line with their dissimilar underlying thermal patterns (Feng and Li, 2013). The authors continued their research and subsequently investigating the SST structures in connection with the Asian summer monsoon, also finding a relationship between the different underlying meridional SST patterns and both the symmetric and asymmetric Hadley cell. Therefore, the importance of the meridional SST structure on the Hadley cell is further emphasized (Feng et al., 2018, 2016).

Pacific Decadal Oscillation

Studies have found an impact of the PDO, on the trend of the Hadley cell extent (Grassi et al., 2012; Lucas and Nguyen, 2015; Rollings and Merlis, 2021). The PDO can be defined as a interdecadal ENSO-like variability pattern of the north Pacific SST (Zhang et al., 1997), which describes a combination of tropical and extratropical processes, rather than one phenomena (Newman et al., 2016). Similar to ENSO, the PDO has a positive and a negative phase, where the prior one is connected to a contraction and the later one to an expansion of the Hadley cell width. A well analyzed pattern shift has occurred in 1976/1977, introducing a positive phase of the PDO which lasted until the late 1990s. These cool anomalies caused a moderated Hadley cell expansion. As the subsequent phase of the PDO is negative, the overall linear trend of the PDO is negative. This shift has caused an accelerated expansion of the Hadley cell width during the mid 1990s until the early 2010s (Amaya et al., 2018; Grassi et al., 2012). Since about 2014 a positive shift has occurred, although this has not yet been well documented in the literature.

Arctic Oscillation

The AO describes a meridional change of pressure in the atmosphere between the Arctic and the midlatitude oceans, so the north Pacific and north Atlantic (e.g., Thompson and Wallace, 2000). A connection between the spring AO and the Hadley cell edge of the northern hemisphere was identified by Hu et al. (2019b) during autumn and winter. A positive phase of the AO leads to a poleward displacement of the northern edge, a negative phase results in an equatorward shift. The relationship does not show a lag, rather it occurs during the same season, due to a connection between the eddy momentum flux divergence and equatorward wave propagation. More specifically, Hu et al. (2019b) propose, that an increased eddy momentum flux divergence can be connected to a strengthened wave propagation from the mid and high to the lower latitudes within the north Atlantic region. Additional research from Seo et al. (2023) shows that, the AO is besides ENSO, the internal cause with the biggest impact on the interannual variability of the Hadley cell extent. Furthermore, it represents the leading mode of natural variability in the extratropics.

2.2 Metrics for quantifying changes

The Hadley cell width has been determined by a multitude of different variables and data sources in previous studies. These so called metrics built on the thermal, chemical, hydrological and dynamical probertites of the variables, resulting in a variety of different results for the Hadley cell edge and the according trend over time (Xian et al., 2021). Besides the variety of metrics, also the methodology differs, resulting in an additional uncertainty (Adam et al., 2018). For this reason, this work chose to focus on the metrics identified suitable by the “International Space Science Institute (ISSI) Tropical width Diagnostic Intercomparison Project” and the “US Climate Variability and Predictability Program (US CLIVAR) Changing Width of the Tropical Belt Working Group”, which evaluated a multitude of different Hadley cell width determination options and produced a code package for more comparable method usage.

The Tropical-width Diagnostics (TropD) code package is available for the programming languages MATLAB and Python. The later one was used in this study (https://tropd.github.io/pytropd/index.html, last access: 29.5.2024). The package uses two basic calculation techniques, which are: identifying the latitude of a zero crossing and finding the latitude of a maximum. Based on these, eight categories of Hadley cell width metrics can be calculated, listed in Table 2.1. Thus, creating more standardized and reproducible methodologies (Adam et al., 2018).

Table 2.1: Hadley cell edge metrics and needed variables for calculation in TropD. The table is based on Adam et al. (2018). The column RO indicates which indices are calculatable from RO data, which is the main dataset of this investigation.

Metric		Variable	RO
PSI	Subtropical edge of the tropical circulation depicted by the zonal-mean meridional mass stream function	Divergent part of the v-component of the wind (v)	
TPB	Latitude of the subtropical tropopause break	Temperature (T)	x
STJ	Latitude of the subtropical jet	u-component of the wind (u)	x
EDJ	Latitude of the eddy driven jet	u-component of the wind (u)	x
OLR	Latitude where Outgoing longwave radiation crosses a threshold	Outgoing longwave radiation (OLR)	
P-E	Subtropical latitude where precipitation minus evaporation becomes positive	Precipitation (P), Evaporation (E)	
PSL	Latitude of subtropical sea level pressure maximum	Sea level pressure (SLP)	
UAS	Subtropical latitude where the zonal-mean near-surface wind becomes westerly	u-component of the wind at the surface (u)	

The metrics shown in Table 2.1, determine the latitudinal edge of the Hadley cell based on different variables. The most commonly used metric is the mean meridional mass stream function, PSI, which is calculated from the divergent part of the meridional wind. Two other wind-based metrics are the subtropical jet, STJ, and the eddy driven jet, EDJ, which both need zonal wind information as input. Also, the near surface zonal wind, UAS, can be applied to locate the Hadley cell edge, as the winds transition from easterlies to westerlies in the subtropical latitudes. On the basis of temperature data, the cell edge can be determined via the subtropical break of the tropopause. Yet another metric uses the outgoing longwave radiation, OLR, which features a maximum in the in the subtropics. Another conventional practice is to connect the Hadley cell edge with the subtropical dry zone, which can be located by positive values when subtracting evaporation from precipitation, P-E. Finally a ridge of high sea level pressure, PSL, can be used to define the boundary of the circulation cell (Adam et al., 2018; Waugh et al., 2018).

However, not all metrics from this list are applicable for RO data. Table 2.1 indicates the possible metrics for the dataset focused on in this thesis. RO data does not cover precipitation, evaporation or outgoing longwave radiation information. Hence, the associated metrics, P-E and OLR, will not be further regarded. And although, pressure and zonal wind data are in general available from RO, so close to the surface the RO method fails, for more detail see Chapter 3.1. Thus, the necessary information is not available and the PSL and UAS metrics will also be dropped. The PSI metric appeared applicable for RO data in the beginning of the investigation, but some insight into the metric and data revealed that it is indeed not. The PSI metric is not just calculated from the

meridional wind component as indicated by some authors and which could be approximated for the most part by the geostrophic equation. But infect the divergent part of the meridional wind holds the essential information to produce the streamfunction and calculate the PSI metric. This leaves three possible metrics for calculation from RO, which are the TPB, STJ and EDJ. A further discussion of the selected metrics and additionally the PSI metric will be given in Chapter 3.2.1.

3 Datasets and methods

The previous chapters focused on introducing the Hadley cell and different metrics to quantify its extent. In this part, the metrics are investigated further with a focus on deriving this information from RO data. The RO methodology and the utilized datasets for the time series analysis are described. Furthermore, suitable datasets for some of the attributing modes of natural variability and external forcings are discussed. This chapter also presents the methodology to investigate the two research interest of this thesis. The methods for the trend analysis of the original time series data for RO and ERA5 and the trend calculation of the residual trend after multiple linear regression analysis are elaborated.

3.1 Datasets

Global Navigation Satellite System (GNSS) radio occultation (RO) is a limb-sounding technique that produces a continuous record of atmospheric observations covering the whole globe. Moreso, the method has all weather capability, high vertical resolution and high accuracy in the upper troposphere and lower stratosphere (UTLS; e.g., Steiner et al., 2020). The resolution at low to mid-latitudes in the troposphere is about 100 m to 200 m, and about 500 m in the lower stratosphere. At high latitudes, in the middle stratosphere the resolution is close to 1.5 km (Zeng et al., 2019). RO offers long-term consistent, multi-satellite climatologies, with no inter calibration between satellite missions. In addition, RO shows long-term stability due to very accurate time measurements when processed accordingly (Steiner et al., 2020). Also, the RO method has the advantage of vertical geolocation of the atmospheric profiles. This means, precise knowledge of the position of the measured air parcel is available, which enables independent information on altitude and pressure (Scherllin-Pirscher et al., 2017). For these reasons, the application of RO data is of high interest and the focus of this thesis.

The GNSS RO technique utilizes the refraction of radio signals transmitted by GNSS satellites and received from low earth orbit (LEO) satellites after moving through the atmospheric refractivity field. Occultations occur when the GNSS satellite rises or sets behind the horizon and two signals with different frequencies propagate through Earth's atmosphere to the receiver. The phase shift and amplitude of the GNSS satellite signal at receival is measured and converted into a bending angel, which is further transformed into a vertical bending angel profile via Abel inversion. Refractivity can then be derived from the bending angle profile of the rising and setting events.

Subsequently, pressure, temperature and density can be computed for a dry atmosphere from the refractivity index using the hydrostatic equation as well as the equation of state (ideal gas law). Also geopotential height can be derived, from this information (e.g., Gleisner et al., 2022; Kursinski et al., 1997). The dry-approximation can be used when water vapor is assumed to be zero, which is largely dependent on the season and latitude. Proceeding, this means dry temperature can be used as a substitute for physical temperature, when the water vapor content of the air is negligible (Danzer et al., 2014), otherwise moist air retrieval needs to be applied (Steiner et al., 2020).

The use of RO data for climate records has been established (e.g., Gleisner et al., 2022), and the high quality and long-term stability of the data has been reviewed in the UTLS region, between approximately 5 km to 35 km altitude (e.g., Steiner et al., 2020). RO data has been successfully applied to investigate the rise of the tropopause height over recent decades, providing evidence of anthropogenic climate change (Meng et al., 2021). Furthermore, RO records have previously been utilized to analyze the Hadley cell extent with regard to climate change with varying results (e.g., Darrag et al., 2022; Davis and Birner, 2013). This work aims to improve the understanding of the utility and added value of RO data for analysis of the Hadley cell width.

3.1.1 Data for time series

Monthly averaged WEGC RO OPSv5.6 data (Angerer et al., 2017; Steiner et al., 2020) available for the time span September 2006 to November 2020 and monthly averaged ERA5 reanalysis data (Hersbach et al., 2020) for the time period 1980 to 2022 was used.

Radio occultation data

This thesis uses monthly averaged RO OPSv5.6 data. This data is derived from RO excess phase and amplitude data from the UCAR/CDAAC (University Corporation for Atmospheric Research/COSMIC Data Analysis and Archive Center), which provides input data from six satellite missions: CHAMP, GRACE, FORMOSAT-3 COSMIC, C/NOFS, SAC-C, MetOp. The UCAR/CDAAC data is then further processed by the WEGC Occultation Processing System OPSv5.6 to atmospheric variables such as geopotential height on isobaric surfaces. Climatologies are available for 147 pressure levels, from 1000 hPa to 5 hPa on a 2.5° x 2.5° latitude-longitude grid. Multi satellite data is available for the period 2001 to 2020 although this thesis only studies the period September 2006 to November 2020, as the quality of the profiles varies in the first years for some of the missions (Angerer et al., 2017; Steiner et al., 2020).

It is important to highlight the fact that the RO OPSv5.6 dataset assimilates background data from the European Centre for Medium-range Weather Forecasts (ECMWF) in the middle and upper stratosphere and lower troposphere, thus the dataset is not completely independent. The assimilation is done to be able to retrieve temperature data for moist air. The background information is included

below an altitude of 16 km, above that the dry temperature very closely resamples the physical one. In the core region from RO data, in the UTLS region, the record is independent of background information (Angerer et al., 2017; Steiner et al., 2020).

For the calculation of the EDJ metric a wind field from RO geopotential was derived. The calculation is based on the work from Danzer et al. (2023). The finite differences and interpolation method as well as the order of calculation was further investigated. The derivation of the wind field is extensively described in the Appendix A.

ERA5

ERA5 resembles the fifth generation of ECMWF reanalysis data. It is available at the Copernicus Climate Data Store (CCDS) and can be easily downloaded via a download script. ERA5 offers global hourly and monthly data for a multitude of variables. In this case, monthly averaged temperature, geopotential, and the u- and v-component of the wind were retrieved. The monthly averaged reanalysis data is available on a 0.25° x 0.25° grid on 37 pressure levels between 1000 hPa and 1 hPa.

This work speculates that there are discontinuities in ERA5 data due to assimilation changes. The last bigger structural alteration has occurred during 2016 (Hersbach et al., 2020) and might have resulted in inhomogeneities along the time axis. In this respect RO could be an advantageous dataset, due to its long-term stability described for example by Steiner et al. (2020).

3.1.2 Indices for regression analysis

Various influences of the Hadley cell change have been elaborated in Chapter 2.1, the concomitant indices have not been discussed yet. A final selection of the considered indices for this regression analysis is given in Table 3.1. Besides multiple ENSO indices, there are also some for the PDO to account for the natural variability. A further index of interest for natural variability would have been for the AO, as discussed in Chapter 2.1.2, though it was disregarded as to not exceed the scope of this thesis. An index for stratospheric ozone is included in the regression analysis. Ozone is an anthropogenic external forcing and hence it may seem counterintuitive to include it in this analysis. However, a great variety of literature describes that the recovery of ozone will strongly reduce or even reverse the trend of the Hadley cell on the southern hemisphere in the first half of this century (e.g., Amaya et al., 2018; Polvani et al., 2011a; Son et al., 2010). It is thus possible that ozone is one of the main drivers causing the discrepancy between the longer record of ERA5 and the shorter span of RO shown in the results section 4.1. To better compare the shorter trend series of RO with the long ERA5 data record, this work chose to account for the Antarctic ozone depletion of the past decades.

Table 3.1: Listing of indices investigated for the use in the multiple linear regression analysis.

Index	Period	dataset	Reference
Niño3.4	1980-2023	HadlSST1	https://psl.noaa.gov/gcos_wgsp/Timeseries/Nino34/
Niño3.4	1982-2024	ERSST.v5	https://www.ncei.noaa.gov/access/monitoring/enso/sst
Relative Niño3.4	1980-2024	ERSST.v5	http://climexp.knmi.nl
MEI.v2	1979-2024		https://psl.noaa.gov/enso/mei/
PDO	1884-2021	HadlSST3	https://climexp.knmi.nl/getindices.cgi?WMO=UWData/pdo_hadsst3
PDO	1854-2024	ERSST.v5	https://www.ncei.noaa.gov/access/monitoring/pdo/
Antarctic stratospheric ozone	1979-2020		http://climexp.knmi.nl
Antarctic stratospheric ozone	1979-2024		https://ozonewatch.gsfc.nasa.gov/meteorology

ENSO index

The effect of ENSO on the Hadley cell extension has been previously discussed in one of the subchapters of section 2.1.2. In order to account for the effects, different ENSO indices where considered. The oldest index is the Southern Oscillation Index (SOI), which is based on the surface pressure difference between Tahiti and Darwin. This pressure difference of the tropical central Pacific and the western one was first found by Sir Gilbert Walker (1924). However, the SOI only describes the atmospheric anomaly, whereas the ENSO is an ocean-atmosphere coupled phenomena. Hence, a better suitable index of ENSO are the sea surface temperature anomalies, first described by Rasmusson and Carpenter (1982).

Many ENSO SST indices are available, differing by the area they are averaged over. One of the most common ENSO indices is the Niño3.4 SST index, displayed in Figure 3.1a. The Niño3.4 is a monthly available index based on SST anomalies over the tropical Pacific (5°S to 5°N and 170°W to 120°W) calculated with the HadISST1 or ERSST v5 dataset (Huang et al., 2017; Rayner et al., 2003). According to the Niño3.4, an El Niño and La Niña event occurs when the three-month average exceeds the NOAA threshold of +0.5°C or -0.5°C, respectively.

As the Niño3.4 index is based on temperature anomalies one has to be aware, that the long-term data records include information of global warming, which means the index includes a trend. Though, a relative index excluding the trend can be calculated. Moreover, a relative Niño3.4 index based on the ERSST v5 dataset, is available at the Royal Netherlands Meteorological Institute (KNMI) Climate Explorer website (van Oldenborgh et al., 2021).

Another ENSO index is the MEI.v2, which is the multivariate ENSO index version 2, shown in Figure 3.1b. In comparison to the Niño3.4 index, it does not only rely on the one variable SST, but instead is also based on four more variables, those are sea level pressure (SLP), surface zonal winds (U), surface meridional winds (V) and Outgoing Longwave Radiation (OLR). The methodology of this index is based on its predecessor MEI by Wolter and Timlin (1993, 1998, 2011), where a time series of the leading principal component analysis for an empirical orthogonal function is calculated for the standardized anomalies of the variables on a 2.5° x 2.5° grid. The reference period for the standardization is 1980 to 2018. The empirical orthogonal function analysis is performed on twelve overlapping bimonthly "seasons". The resulting MEI values indicate El Niño and La Niña events, with great positive and negative values, respectively (Zhang et al., 2019).

Besides small deviations in the magnitude, all Niño3.4 indices follow the same pattern as can be seen in Figure 3.1. Contrary the MEI.v2 index deviates slightly. Yet the peaks for all still coincide over the time span 1980 to 2024.

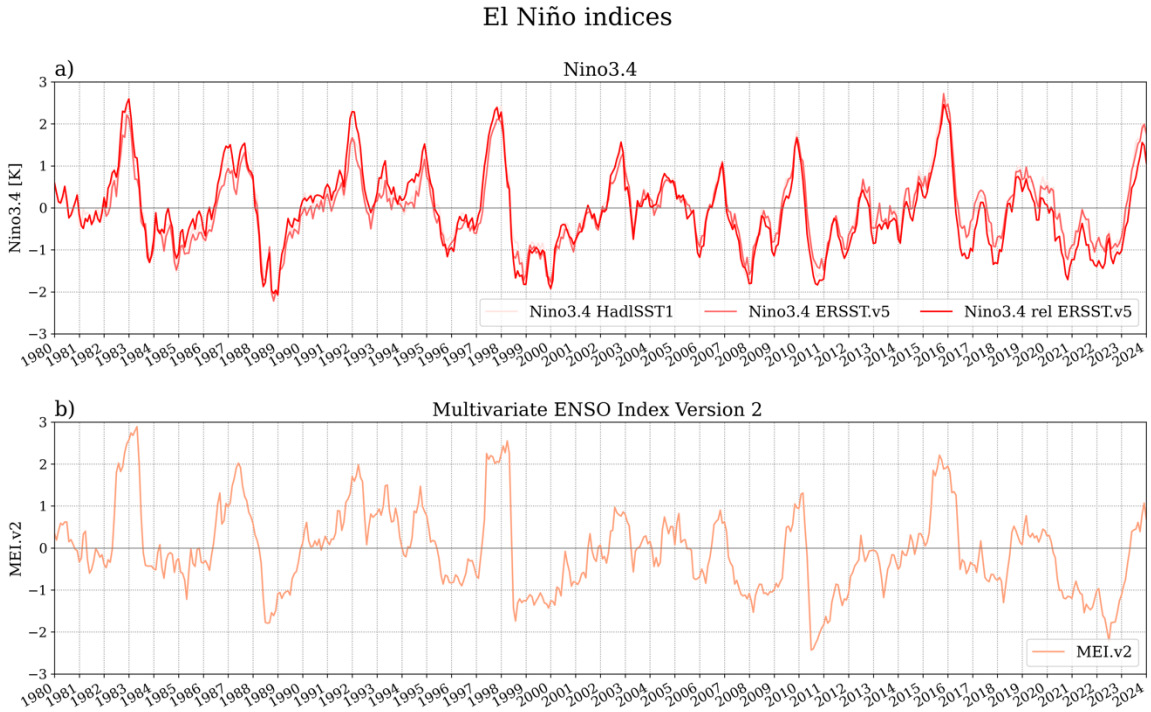

Figure 3.1: ENSO indices over the time period 1980 to 2022. Plot (a) shows the three different Niño3.4 indices. plot (b) displays the time series of MEI.v2.

PDO index

Another impact on the trend of the Hadley cell extent to be accounted for, comes from the Pacific decadal Oscillation, as mentioned in a subsection of Chapter 2.1.2. The PDO is an established climate index, which was first found by Mantua et al. (1997) by performing a principle component analysis of the leading empirical orthogonal function. Different PDO indices are available for

multiple SST datasets, similar to the Niño3.4 those are e.g., the HadISST3 and ERSST v5, shown in Figure 3.2.

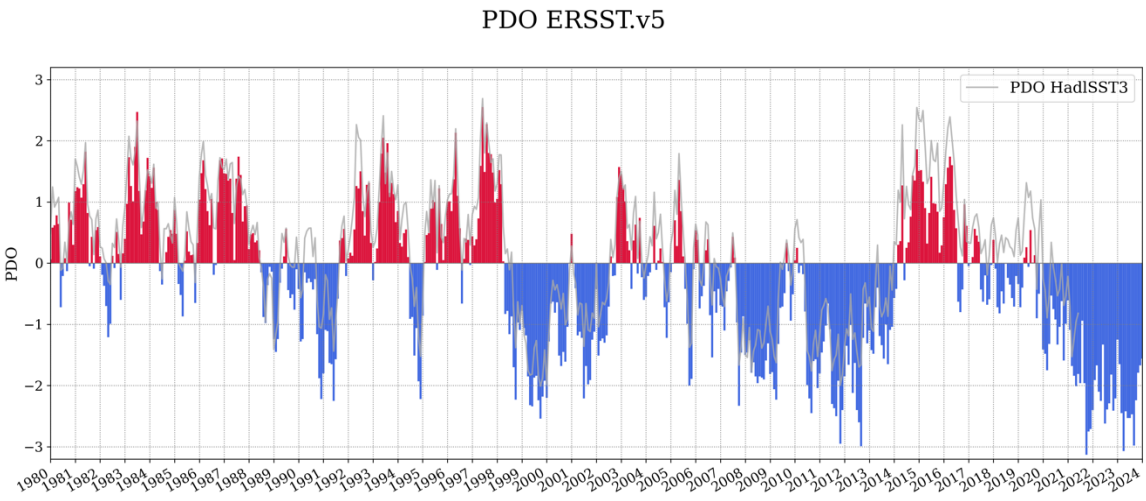

Figure 3.2: PDO index over the time period 1980 to 2024. Red marks positive phases of the PDO, blue marks the negative ones. Additionally, the PDO index for the HadSST3 dataset is plotted in grey.

Ozone index

The last index explored in this analysis shows the development of ozone in the stratosphere, its impact previously explained in a subchapter of 2.1.1. An index for the Antarctic ozone hole is selected, as it is a prominent feature effecting the Hadley cell width (Polvani et al., 2011b). The ozone hole appears during southern hemisphere spring as it takes polar stratospheric clouds and sunlight for the breakdown of ozone. Stratospheric clouds develop during the very cold temperatures of the winter months and sunlight in spring allows for the chemical catalytic reaction of bromine and chlorine to set in (e.g., World Meteorological Organization, 2022).

The ozone mass deficit (OMD) indicated in mega tons from Nasa's Ozone Watch is used as a variable to describe the ozone depletion and its current recovery over the past decades. OMD denotes the gap between the total ozone column and reference value of 220 Dobson Units (DU). Previous to the early 1980s, values for the total ozone column of 220 DU or less were not recorded, as they did not occur. Thus, 220 DU represents the historical minimum level. In comparison to other ozone hole metrics, like the ozone hole area or the ozone minimum, the OMD shows less variation attributed to atmospheric dynamics or the mixing and chemistry. The OMD is measured during the end of September and mid-October, when the ozone hole reaches its largest extent (de Laat et al., 2017).

The time series of the OMD from Nasa has some data gaps, those are especially apparent around the year 1996. A second OMD dataset from the KNMI was investigated in comparison to the Nasa record. The two data records are nearly identical except that the Nasa dataset shows missing values

and the KNMI record ends in the year 2020. As a result the longer record from Nasa was chosen. However, the missing values are filled with the information from KNMI to get a continuous record.

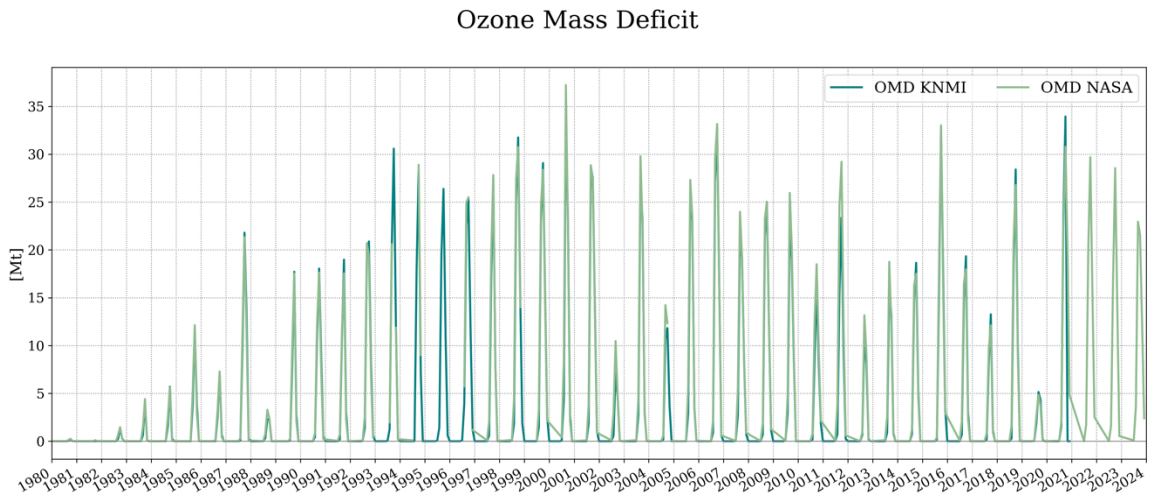

Figure 3.3: Time series of the ozone mass deficit over the period 1980 to 2024 in mega tons for the Nasa Ozone Watch and the KNMI dataset.

3.2 Methods

The methods section is separated into three parts. The first focuses on describing the selected metrics used throughout this thesis. The second part explains the application of the metrics and the time series analysis of the Hadley cell with climate change, which forms the first big analysis section of this work. Thirdly, the regression analysis done to extend the time series analysis and gain further inside into the trend is elaborated. This part presents the second major analysis segment of this thesis.

3.2.1 Metric selection

Of the eight metric categories presented in Chapter 2.2, three are suitable for RO data, which is the focus dataset of this thesis. Therefore, these get investigated further in the upcoming sections. The metrics identified for RO are the Tropopause break (TPB), the subtropical jet (STJ) and the eddy driven jet (EDJ). Initially, also the meridional mass stream function (PSI) seemed applicable and will hence be described briefly. For further information of the calculation method see Adam et al. (2018).

Tropopause break

One metric to determine the Hadley cell edge is the TPB, which describes the sudden change in tropopause altitude between the tropics and extratropics (Martin et al., 2020). The TPB has been widely studied in previous work, using multiple definitions and methods (e.g., Davis and Birner,

2016; Davis and Rosenlof, 2012; Martin et al., 2020; Seidl and Rammer, 2016). Here, two definitions of the TPB are picked and studied, both implementing the tropopause definition of the World Meteorological Organization (WMO). According to the WMO (1957), the tropopause is defined as "the lowest level at which the lapse-rate decreases to 2°C/km or less, provided that the average lapse-rate between this level and all higher levels within 2 km does not exceed 2°C/km. After the tropopause is identified, the TPB can be located".

The first method used in this study to define the TPB, is the maximum gradient $\partial Z/\partial\varphi$. This method defines the TPB as the latitude where the meridional tropopause gradient has its maximum (e.g., Davis and Rosenlof, 2012). An example of this method is seen in Figure 3.4a, which shows the tropopause height in meters and the according TPB indicated at the maximum gradient.

The second method identifies the TPB via the maximum tropospheric dry bulk static stability $\Delta\theta$. It is located at the latitude of the maximum potential temperature of the tropopause height and the minimum value of the column, which is expected to be at the surface. This difference is used to account for the bulk stability within a layer, in this case the troposphere (Davis and Birner, 2013). Figure 3.4b. visualizes an example of this method. The graph shows the potential temperature difference along the latitudinal axis, the TPB is marked.

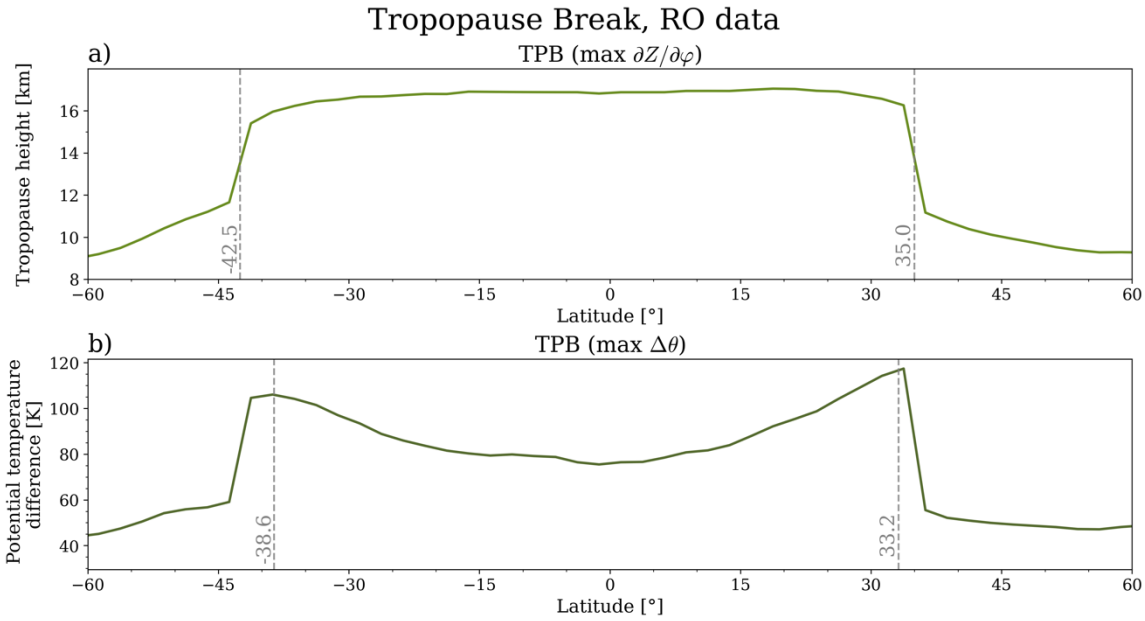

Figure 3.4: Tropopause break determined for two metrics. TPB (max $\partial Z/\partial\varphi$) from the tropopause height in kilometers (a) and TPB (max $\Delta\theta$) from the potential temperature difference in Kelvin (b) are displayed. Both are calculated with the TropD package using monthly-mean RO temperature data for January 2009. The TPB is marked by the gray dashed lines and the according latitudes.

Both metrics are very similar to one another. Concern for the sensitivity of the maximum gradient $\partial Z/\partial\varphi$ method to noise and grid spacing has been raised, as the latitude values are restricted to the horizontal resolution (Adam et al., 2018; Davis and Birner, 2017; Davis and Rosenlof, 2012).

In comparison to other TPB metrics, the two metrics studied in this thesis, are objectively based. In contrast, other TPB metrics are often threshold-based, which introduces a sensitivity to the subjective choice of a threshold. For example, one TPB metric identifies the latitude at which the tropopause height equals to 15 km. Another, locates the tropopause break at the latitude where the tropopause height drops 1.5 km below the tropical average tropopause height measured between ±15° of the equator (Adam et al., 2018; Davis and Rosenlof, 2012).

Eddy driven jet

Another metric for analyzing the Hadley cell edge is the eddy driven jet. Previous studies found, that the eddy momentum flux has an important impact on the structure of the general circulation (Caballero, 2007; Kim and Lee, 2004), especially in the austral summer, DJF (Kang and Polvani, 2011; Polvani et al., 2011b). Although the eddy momentum fluxes are stronger in the austral winter season, JJA, the correlation with the Hadley cell during this season is rather small. The core of the Hadley cell circulation seems to be isolated from the extratropical eddy fluxes and the variability of the Hadley cell in austral winter shows angular-momentum conserving dynamics (Zurita-Gotor and Álvarez-Zapatero, 2018).

EDJ is calculated as, the latitude at which the maximum of the zonal wind closest to the 850 hPa level can be found. The TropD software uses a linear interpolation of the zonal-mean zonal wind gradient at 850 hPa, and the EDJ is defined as the latitude of the maximum of that polynomial. Figure 3.5 shows the calculated zonal wind field for RO data and the Hadley cell edge as determined by the EDJ and STJ metric. As expected, the EDJ results lie further poleward than other metrics. This is in line with the general understanding of atmospheric dynamics, as the EDJ lies outside the Hadley cell. Still, according to the literature, the EDJ correlates well with its extension (Menzel et al., 2024; Waugh et al., 2018; Xian et al., 2021). Thus, it can be a good indirect measure for Hadley cell edge position changes.

According to Waugh et al. (2018), who studied climate models for a quadrupling CO_2 concentration scenario, the magnitude of width change of the EDJ metric in comparison to PSI differs. In some models, they find that the Hadley cell edge according to the PSI moves half the distance of the EDJ (1:2). Whereas in other models the metrics show similar changes (1:1). Also, Staten and Reichler (2014) found a interannual ratio between the EDJ and Hadley cell edge of 1.58:1 for the DJF in the southern hemisphere in climate models. Previously, Kang and Polvani (2011) found a 1:2 ratio for austral summer southern hemisphere. To the best of my knowledge a ratio between these metrics has not yet been investigated for reanalysis or observational data and the comparison of the calculated trends is hence to be interpreted with caution.

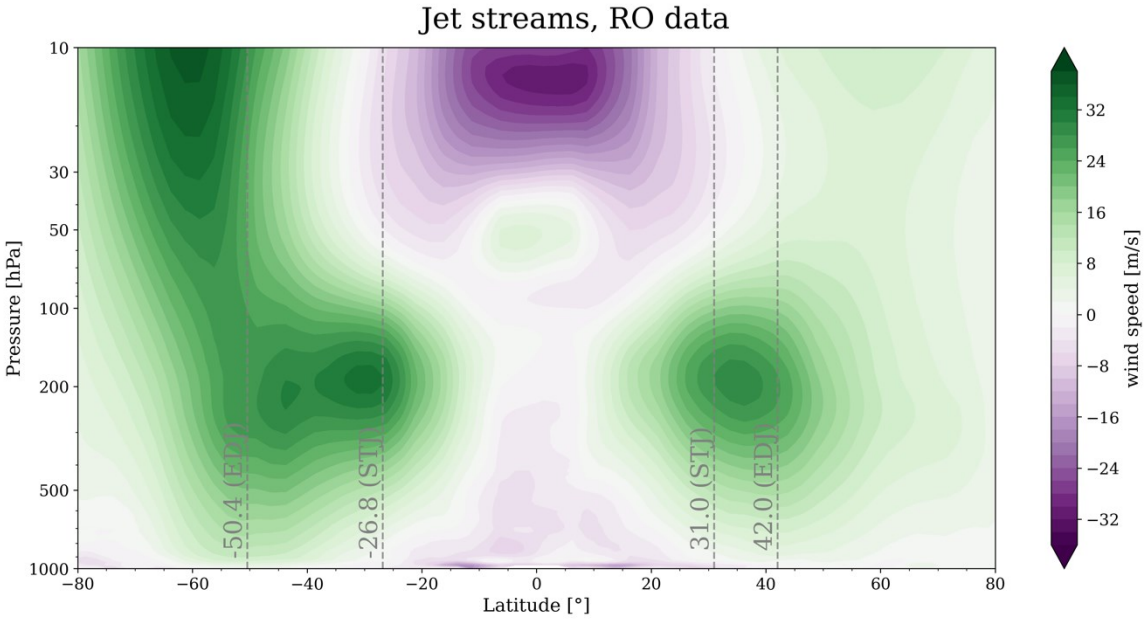

Figure 3.5: Annual average RO wind field 2009 of the u-component for monthly-mean RO data. The gray lines represent the location of the subtropical jets and the eddy driven jets calculated with the TropD package.

Subtropical jet

One metric frequently analyzed in studies to determine the tropical width is the Subtropical Jetstream (Davis and Birner, 2013). The STJ is a thin band of strong winds in the upper troposphere, which is attributed to the angular momentum fluxes within the Hadley circulation. Its location is at the edge of the descending branch of the Hadley cell, as explained by the axisymmetric circulation theory of Held and Hou (1980). Previous studies assumed that the poleward shift of the STJ can be related to the expansion of the Hadley cell width and therefore be used as an indicative metric. This jet metric can be calculated from the maximum wind speed of the zonal-mean zonal wind (e.g., Adam et al., 2018; Davis and Birner, 2013) trends of 0.1° per decade (Davis and Rosenlof, 2012) to 0.6° per decade were identified (Davis and Birner, 2013).

However, Waugh et al. (2018) discard the use of the STJ as an indicator for the Hadley cell edge expansion, based on their study of coupled climate models. In order to test different edge-metrics, they analyzed a simulation of quadrupled atmospheric CO_2 concentration as well as preindustrial control simulations and found a none to weak correlation between the STJ and the expansion of the Hadley cell edge. Yet, they identified changes in the magnitude of the winds of the STJ related to the Hadley cell width (Waugh et al., 2018). Based on these results, Menzel et al. (2019) conducted a similar analyses, agreeing with previous findings. In addition, they further investigated the correlation of the STJ strength and Hadley cell edge and showed that interannually, a weak to moderate negative correlation exist, whereas increased CO_2 concentrations lead to a positive correlation. They further studied the time frame of response to a CO_2 increase and found varying

time scales, which let them conclude that the location of the Hadley cell edge and the STJ is not induced by the same physical processes (Menzel et al., 2019). These findings are supported by results from Chemke and Polvani (2019), who observed that the Hadley cell expansion is connected to a poleward shift in the subtropical eddy momentum fluxes and the increase of the subtropical static stability.

Maher et al. (2020) found that the magnitude of the poleward shift trends differs for the STJ and the Hadley cell edge in reanalysis data. Considering natural variability as a reason for smaller shifts of the STJ in comparison to other Hadley cell edge metrics, they show that trends could consistently be identified. Thus, natural variability is rejected as an explanation for the different trends. Further they argue, that there is weak evidence describing the overall trends for the STJ shifting poleward on both hemispheres, especially for monthly-mean data, which is used in many studies (Maher et al., 2020).

A recent study by Menzel et al. (2024) underlines the correlation between the Hadley cell edge and the latitude of maximum eddy momentum flux, whereas the STJ shows different sensitivities. In contrast, the latitude of the STJ can be related to the meridional temperature gradient, this was first suggested by Davis and Birner (2017). Further investigations by Menzel et al. (2019) found, similar time scales for both the increase of STJ strength and the meridional temperature gradient under quadrupled CO_2 scenarios, therefore highlighting this connection. Moreso, the STJ is closely connected to the upper tropospheric upwelling in regard to their seasonality, axis symmetry and response time to CO_2 increase. Increased CO_2 leads to a strengthening and narrowing of the upper tropospheric upwelling and a strengthening of the STJ, caused by an increased poleward advection of the circulation's angular momentum (Menzel et al., 2023).

As a result, the STJ metric is not suitable as an indicator for the Hadley cell edge and therefore not further investigated in this thesis, although it would have been suitable for analyses with RO data, as shown for example by Davis and Birner (2013).

Meridional mass stream function

The tropical edge, according to the PSI metric, is the latitude poleward of its maximum in the tropics, at which the zonal-mean meridional mass stream function ψ changes its sign. The method for its exact location varies. One option is to locate the latitude of the zero-crossing at the 500 hPa level, an example is displayed in Figure 3.6. The PSI is a very commonly used metric in the literature (e.g., Davis and Birner, 2017; Waugh et al., 2018).

This metric can be calculated with the vertical integral of the zonal-mean meridional wind. Yet, it must be mentioned that the zonal-mean meridional wind, for the geostrophic approximation is zero, as it is non divergent (Holton and Hakim, 2012). Therefore, RO data is not suitable. However,

ERA5 data includes divergent information in their v-component of the wind, thus for comparative purposes, the PSI will be calculated for this dataset.

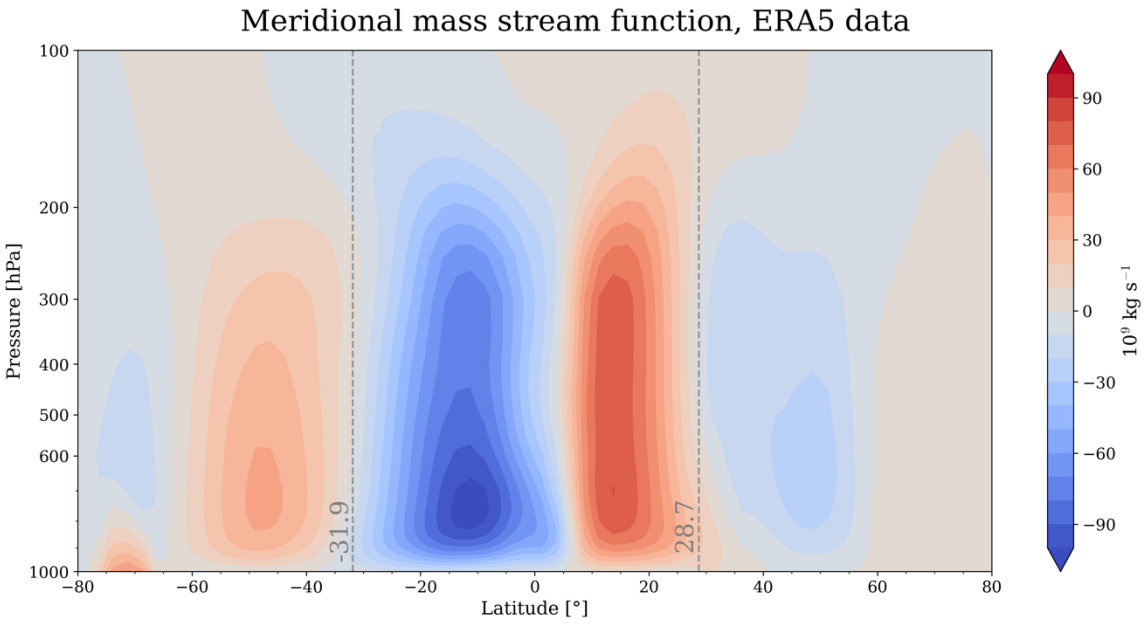

Figure 3.6: Mean meridional mass stream function for the annual average 2009 for monthly ERA5 data in 10^9 kg/s. The Hadley cell edge derived from the PSI metric is marked by the gray dashed lines and the according latitudes.

3.2.2 Applied metrics

To start the ERA5 data is binned onto a 2.5° x 2.5° spatial grid, via cosine weighted binning, for better comparability with RO and a wind field is established for RO data. Both datasets now include temperature and wind field information on pressure levels and a uniform spatial grid. From this input data, the three metrics identified to be most suitable for RO input data and one additional one for ERA5 get calculated using the Tropical-width Diagnostics TropD computational package previously discussed. Again the selected metrics are the Tropopause break (see Chapter 3.2.1), calculated from the maximum poleward gradient (max $\partial Z/\partial \varphi$) and the maximum potential temperature difference between the tropopause and the minimum value (max $\Delta\theta$), which is assumed to be at the surface. Both these metrics are derived from temperature data. The third metric which was chosen is the eddy drive jet (see also Chapter 3.2.1), which actually lies outside the Hadley cell, although according to the literature correlates well with its extension (Waugh et al., 2018; Xian et al., 2021). The EDJ is calculated from the maximum zonal mean zonal wind.

Based on the information established in Chapter 3.2.1 about the EDJ and Chapter 3.1 discussing the RO data, the use of the EDJ as a Hadley cell metric for RO data is not ideal. As previously mentioned, RO data has a core region of high quality data between 8 km to 35 km and assimilates ECMWF short-range forecast data in the lower levels (Steiner et al., 2020). The EDJ is measured

at 850 hPa, which corresponds to a height of approximately 1.5 km. The EDJ thus lies clearly outside the optimal region of RO data and is strongly dependent on the background information. Nevertheless, the EDJ metric is still calculated and investigated in this thesis.

Additionally to the metrics selected for RO, the meridional mass stream function (PSI) will be calculated for ERA5 data. The PSI metric is a very commonly investigated measure of the Hadley cell extent and hence is of interest for better comparability of the results.

3.2.3 Time series analysis

At the beginning, my analysis focuses on the RO dataset. First, similar to the approach by Davis and Birner (2013), the mean Hadley cell edge and its standard deviation are calculated for monthly data and the seasonal cycle is regarded for each metric. It must be noted that throughout the analysis, the northern and southern latitudinal edge and the resulting overall interhemispheric width will be investigated. However, this terminology is only true for the TPB metrics and the PSI and not valid for the EDJ. As mentioned above, the EDJ lies poleward to the Hadley cell edge and the absolute difference between the northern and southern location of the jet cannot be regarded as the Hadley cell width. Nonetheless, the EDJ metric will be shown in some of the plots, the cell edges are then to be understood as the location of the jet streams.

Secondly, anomalies, so deseasonalized data, are produced in order to reduce seasonal variation in the results and allow for better trend and correlation analysis. The deseasonalization is done as in Davis and Birner (2017), by subtracting the overall mean monthly value from the respective monthly mean. As an example, the mean of all Januarys is removed from each January. The EDJ metric can now be considered the same as the other metrics. A time series of the RO anomalies for each metrics northern cell edge, southern cell edge and cell width is plotted, and a linear regression trend is identified. Additionally, annual, and seasonal trend values for RO are investigated and compared. The statistical significance of the trend is determined by a t-test with the p-value limit set to 0.05.

In a next step, the investigation centers on a comparison of the RO and ERA5 data. The results of RO are compared to ERA5 data for the same time period, i.e., from 2006 to 2020. The Pearson correlation coefficient is computed for each metric, for annual, seasonal, and monthly data for each hemisphere. The correlation coefficient can take values between ±1, where 1 describes a very strong positive correlation and -1 a very strong negative one. A value of zero would indicate no correlation between the investigated features. This line of analysis is concluded with a focus on the long-term trend of ERA5 data. Similar to a rolling mean, a rolling trend for different time windows is calculated in order to investigate and understand the influence of the chosen time period on the trend results.

During the whole analysis a consistent color scheme will be used, where the tropopause break metrics are displayed in a green color, TPB (max $\partial Z/\partial \varphi$) in a lighter olive tone and TPB (max $\Delta\theta$) in a darker olive, and the EDJ metric in a blue tone. The PSI metric for ERA5 data is displayed in a reddish tone. The time period under investigation is always September 2006 to November 2020, except when noted otherwise.

3.2.4 Regression analysis

To investigate the trend of the Hadley cell in more detail the variability from ENSO and the PDO and the forcing from ozone change are removed from the time series. For this a multiple linear regression model similar to Rollings and Merlis (2021) and Meng et al. (2021) is applied:

$$HCW(t) = \beta_0 + \sum_{i=1}^{n} \beta_i X_i(t + \tau_i) + \epsilon_i \qquad (1)$$

where β_0 is the intercept, β_i represents the regression coefficient, X_i is the independent variable, τ_i is the time lag of each index and ϵ_i is the residual. In the context of this Ordinary Least Square (OLS) analysis, the Hadley cell diagnostics are the dependent variables, which each are explained by the independent variables for ENSO, PDO and ozone. The indices pose as predictors for the Hadley cell metrics. By transforming the equation, the residuals present the metric with the independent variables regress out. A trend excluding the influence of ENSO, PDO and ozone changes can be determined. This line of investigation is done for the three different datasets, (i) ERA5 from 1980 to 2022, (ii) ERA5 from September 2006 to November 2020, and (iii) RO from September 2006 to November 2020. The multiple linear regression model is applied individually for each dataset.

To determine the best suitable indices for the different influences on the Hadley cell, correlations between the indices and metrics, as well as the correlations of the individual indices themselves are investigated for the long time period of ERA5. The later one is done, to select indices with little to no collinearity, to improve the explanatory power of the model. Again the Pearson correlation method is utilized. Furthermore, the lag between the individual indices and the metrics was examined, for this a cross correlation was performed for a lag span of ±12 months.

The final selection of indicators is further preprocessed for the multiple linear regression. Temperature anomaly indicators like the one for ENSO are detrended, as to not include the global warming trend. Multiple approaches exist for this task. The Oceanic Niño Index (ONI) from NOAA for example subtracts a 30-year average, which is updated every five years. This detrending method, however, has its shortcomings. Besides regular discontinuities, due to the change of baseline every five years, the most recent years cannot be calculated and must be corrected later on. Thus, more

current values include trend residuals which strongly influence the detection of La Niña and El Niño events, as they can greatly add to the considered anomaly value (Rollings and Merlis, 2021; van Oldenborgh et al., 2021).

Another method to detrend these indices, is to remove the regression of global warming or the CO_2 concentration of the atmosphere from the index. This can however, lead to large uncertainties as ENSO experiences great variability (van Oldenborgh et al., 2021).

Lastly, van Oldenborgh et al. (2021) based on the work of Johnson and Kosaka (2016) propose to calculate a relative Niño3.4 index by subtracting the concurrent mean of the 20°S to 20°N SST anomalies from the Niño3.4 index. As both regions have within uncertainties a similar trend, subtracting one from the other cancels the trend. The same is true for the other El Niño index regions Niño 1+2, Niño 3, and Niño 4. The method slightly overcorrects the central value; therefore the authors propose to rescale the variability. The Relative Niño3.4 index shown in Chapter 3.1.2 is based on this approach.

Also, the indices were normalized, as in equation (2),

$$N = (X - \mu)/\sigma \tag{2}$$

where X is the indices value, μ is the mean value of the respective reference period of each index and σ is the standard deviation. By dividing the anomalies by the respective standard deviation, one gains standardized anomalies. This means the distribution of each index is converted into a standard normal distribution, which allows for better comparability of the regression coefficients in the subsequent analysis.

4 Results

The results section is divided into two parts, respective of the explained methodology in Chapter 3.2.3 and Chapter 3.2.4. At first an extensive time series analysis of the Hadley cell based on the selected metrics will be performed. Followed by a regression analysis in order to improve the results of the trend investigation.

4.1 Time series analysis of the Hadley cell width

In this section, the results of the Hadley cell edge and trend analysis for the original datasets are presented and discussed. The time series of the chosen metrics are calculated and investigated using monthly-mean RO and ERA5 temperature and wind data for the time span September 2006 to November 2020. In addition, also the long-term trend for ERA5 data, so 1980 to 2022, will be examined. The seasonal cycle is considered as well as the trend over the investigated period, and the importance of the selected time period for shorter time windows is demonstrated.

4.1.1 Hadley cell edge and seasonal cycle

This thesis first examines the average location of the northern and southern latitudinal Hadley cell edge and the associated overall interhemispheric width for each metric during the RO record period for RO data (see Table 4.1) and ERA5 data (see Table 4.2). The average northern edge is located at 38.15° and 33.97°, the average southern edge at -36.07° and 32.64° for RO data, for the two tropopause break metrics TPB (max $\partial Z/\partial\varphi$) and TPB (max $\Delta\theta$), respectively. As previously described, the EDJ metric gives the location of the jet but not the Hadley cell edge. The jet is located at 43.00°N and 50.25°S. The standard deviations of all metrics and measures are of similar magnitude, although it is slightly greater for the northern hemisphere and the calculated width, the later one was to be expected.

Table 4.1: Listing of the mean Hadley cell edge and width and location of the EDJ for RO data over the period September 2006 to November 2020 including the standard deviation. The difference between the northern and southern location of the EDJ does not describe the Hadley cell width and is thus excluded.

RO data	North	South	Width
EDJ	43.00° ±5.37°	-50.25° ±3.63°	
TPB (max $\boldsymbol{\partial Z/\partial\varphi}$)	38.15° ±4.83°	-36.07° ±3.37°	74.22° ±4.91°
TPB (max $\boldsymbol{\Delta\theta}$)	33.97° ±3.66°	-32.64° ±2.72°	66.60° ±4.64°

Table 4.2 displays the equivalent results for ERA5 data. The location of the northern and southern edge, as well as the width and location of the eddy driven jet, are very similar in their average and standard deviation to the one calculated from RO data. Additionally to the three metrics suitable for RO, also the PSI metric is calculated for ERA5 and displayed in the table. The northern edge according to the PSI lies the most equatorward from all the metrics, in comparison the southern edge corresponds approximately with the TPB (max Δθ). The PSI metric exhibits the smallest width, but again it is close to the one from the TPB (max Δθ) metric.

Table 4.2: As in Table 4.1 for ERA5 data over the time span September 2006 to November 2020.

ERA5 data	**North**	**South**	**Width**
PSI	30.79° ±5.10°	-32.34° ±3.15°	63.34° ±4.70°
EDJ	45.51° ±5.13°	-51.47° ±2.58°	
TPB (max $\boldsymbol{\partial Z/\partial \varphi}$)	38.03° ±4.97°	-35.88° ±3.41°	73.91° ±5.08°
TPB (max $\boldsymbol{\Delta\theta}$)	33.37° ±2.97°	-32.24° ±2.64°	65.61° ±4.23°

Figure 4.1 displays the time series of the Hadley cell edge metrics for monthly-mean RO data over the record period September 2006 to November 2020. The time series is plotted for the cell edges of both hemispheres and the cell width. The data seems to be quite consistent for all metrics over the observation period, with a visible seasonal cycle in all but one. No obvious trend over the years can be identified. The TPB metrics follow a very close pattern, especially on the southern half. The TPB (max ∂Z/∂φ) lie a bit poleward of the TPB (max Δθ). On the northern hemisphere, the EDJ lies just north of the TPB metrics. On the southern hemisphere both TPB metrics are located significantly further equatorward then the EDJ throughout the time series. Furthermore, the time series of the EDJ moves differently to the other metrics. The southern hemisphere jet location appears to be rather stochastic, and the seasonal cycle seems to be not well defined.

To gain some further insides into the seasonality of the Hadley cell, the annual cycle of the monthly metrics averaged over the whole period for the northern and southern edge, and the corresponding width is plotted in Figure 4.2. The seasonal cycle is more pronounced for the northern hemisphere and the TPB metrics, with an amplitude of about 10°.

When looking at the seasonal cycle of the tropical width, two clear maxima are visible for both TPB metrics. One in February and one in August, hence when the Hadley cell reaches its maximum extent in the southern and northern late summer, respectively. In contrast, the minimum extension occurs in May during northern hemispheres spring and southern hemisphere autumn. A second reduced minimum can be identified during November, which appears to be more dependent on the northern cell edge, as the minimum on the southern hemisphere is barely detectable. The width for

both TPB metrics varies with an amplitude of 15° during the seasonal cycle. The TPB (max $\partial Z/\partial \varphi$) extends between about 65° to 80° and the TPB (max $\Delta\theta$) between about 60° to 73°.

Figure 4.1: Time series of the Hadley cell metrics for RO data northern edge (a), southern edge (b) and the width resulting from the tropopause break metrics (c) over the period September 2006 to November 2020.

For comparison, the seasonal cycle for ERA5 was examined for the RO record period and the long-term, 1980 to 2022. Additionally to the RO metrics, the PSI metric was also computed. Figure 4.3 shows the seasonal cycle for ERA5 data for the long-term record. The annual course of the metrics for RO resembles the one from ERA5 very closely. Only the course of the EDJ metric, differs marginally on the northern hemisphere. It appears to be slightly smoother for the ERA5 data. Minor differences are visible for the cell width. The width for the long-term ERA5 data is just noticeably narrower than the one for RO data in Figure 4.2.

The course of the seasonal cycle of the PSI is similar to the one from the TPB metrics in the northern hemisphere. On the southern hemisphere, the PSI only presents with one maximum and one minimum during the seasonal cycle. The maximum occurs in February, as for the other metrics, the

minimum happens in the winter month, JJA, although it is not as pronounced as the other extreme points. Furthermore, the resulting PSI width values appear to be shifted by one month. Thus, the seasonal course of the width of the PSI lags the other metrics by one month. All in all, the seasonal cycle is very similar for both datasets, RO and ERA5, and all time periods. For this reason, no additional plot for the ERA5 seasonal cycle of the shorter time period is displayed.

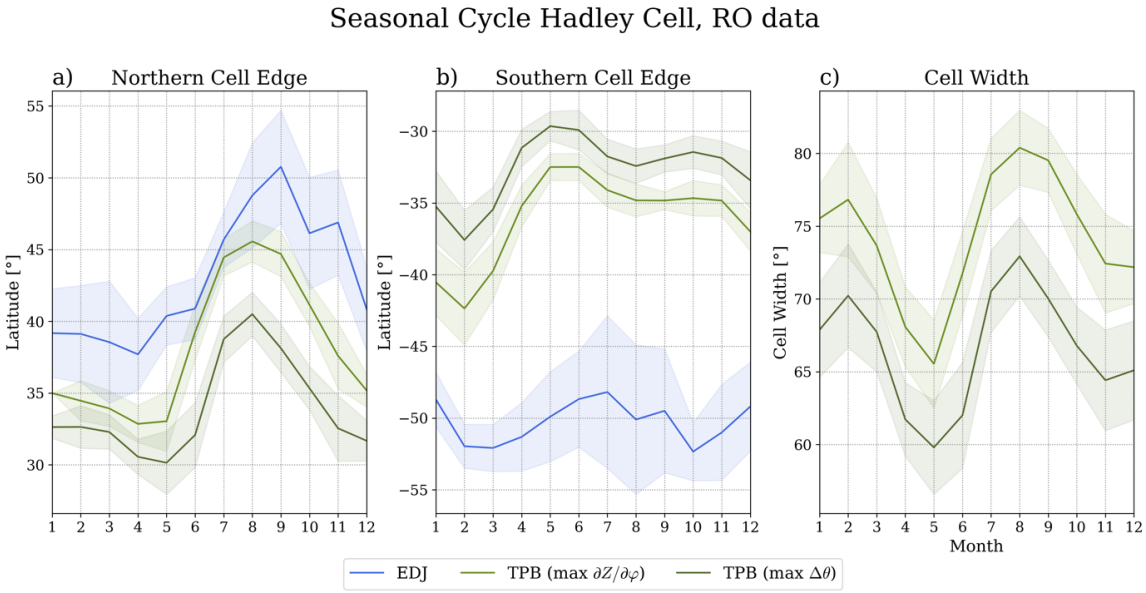

Figure 4.2: Seasonal cycle of the Hadley cell metrics for the northern cell edge (a), southern cell edge (b) and cell width (c) for averaged RO data. The shaded area marks the ±1 standard deviation.

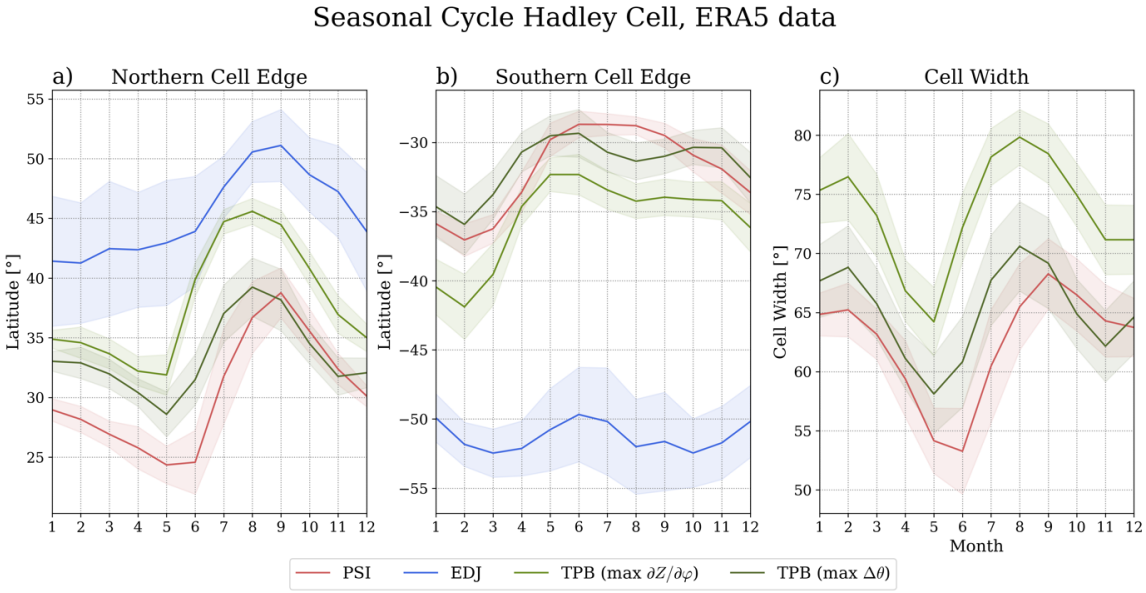

Figure 4.3: As in Figure 4.2 for averaged ERA5 data over the period 1980 to 2022.

4.1.2 Hadley cell trend – RO

Next, the monthly-mean anomaly values are considered, and a linear regression trend is calculated. The time series of the anomalies and the marked trend lines are shown in Figure 4.4, the concomitant trend values are listed in Table 4.3. The trend for all metrics shows that the northern and southern edge are shifting equatorward, this results from a negative trend on the northern hemisphere and a positive trend on the southern hemisphere. In conjunction, the width of the Hadley cell has been decreasing over the RO record period for all metrics. The strongest trend is produced by the EDJ metric. The trend for the EDJ width is -1.82° per decade, this is the only statistically significant trend in this analysis. Yet, its time series shows the greatest amplitude of anomalies compared to the other metrics. The narrowing trend lies between 0.48° and 1.82° per decade.

Table 4.3: List of the Hadley cell trend values for the northern and southern edge and the cell width, for monthly-mean deseasonalized RO data over the period September 2006 to November 2020. The trend is given in ° per decade. Statistically significance is assumed for p-values < 0.05, the congruent results are marked with an asterisk (*).

RO data	North	South	Width
EDJ	-0.631	1.193	-1.824*
TPB (max $\boldsymbol{\partial Z/\partial \varphi}$)	-0.161	0.322	-0,483
TPB (max $\boldsymbol{\Delta \theta}$)	-0.258	0.344	-0.602

To explore the Hadley cell trend from RO data some more, an annual and seasonal trend was investigated next to the monthly one, see Figure 4.5. The annual trend exhibits the same signal direction as the monthly trend, although the signal magnitude is different. The TPB metrics have a larger trend on both hemispheres for the annual estimation. In comparison, the EDJ shows a weaker narrowing trend and a standard deviation which crosses the zero line. Hence, the EDJ result for annual data does not seem reliable.

For the individual seasons the trend and standard deviation can vary greatly. On the northern hemisphere, the results indicate a narrowing for MAM and JJA, and a widening through SON. During the winter, DJF, the trend all but disappears for the EDJ and the TPB (max $\partial Z/\partial \varphi$) metrics. Contrary, the TPB (max $\Delta\theta$), still signals a strong narrowing result. As for the southern hemisphere, the trend for the different metrics only shows a uniform, distinct narrowing trend for DJF. MAM presents a small widening trend. The other two seasons, JJA and SON, are not consistent for the different metrics, a widening as well as narrowing is signaled. In terms of the width, the trend shows a narrowing, with the exception of the TPB (max $\partial Z/\partial \varphi$) metric in JJA and the TPB (max $\Delta\theta$) metric during SON. The strongest trend for the TPB metrics occurs during DJF, whereas the EDJ signals the greatest contraction in JJA.

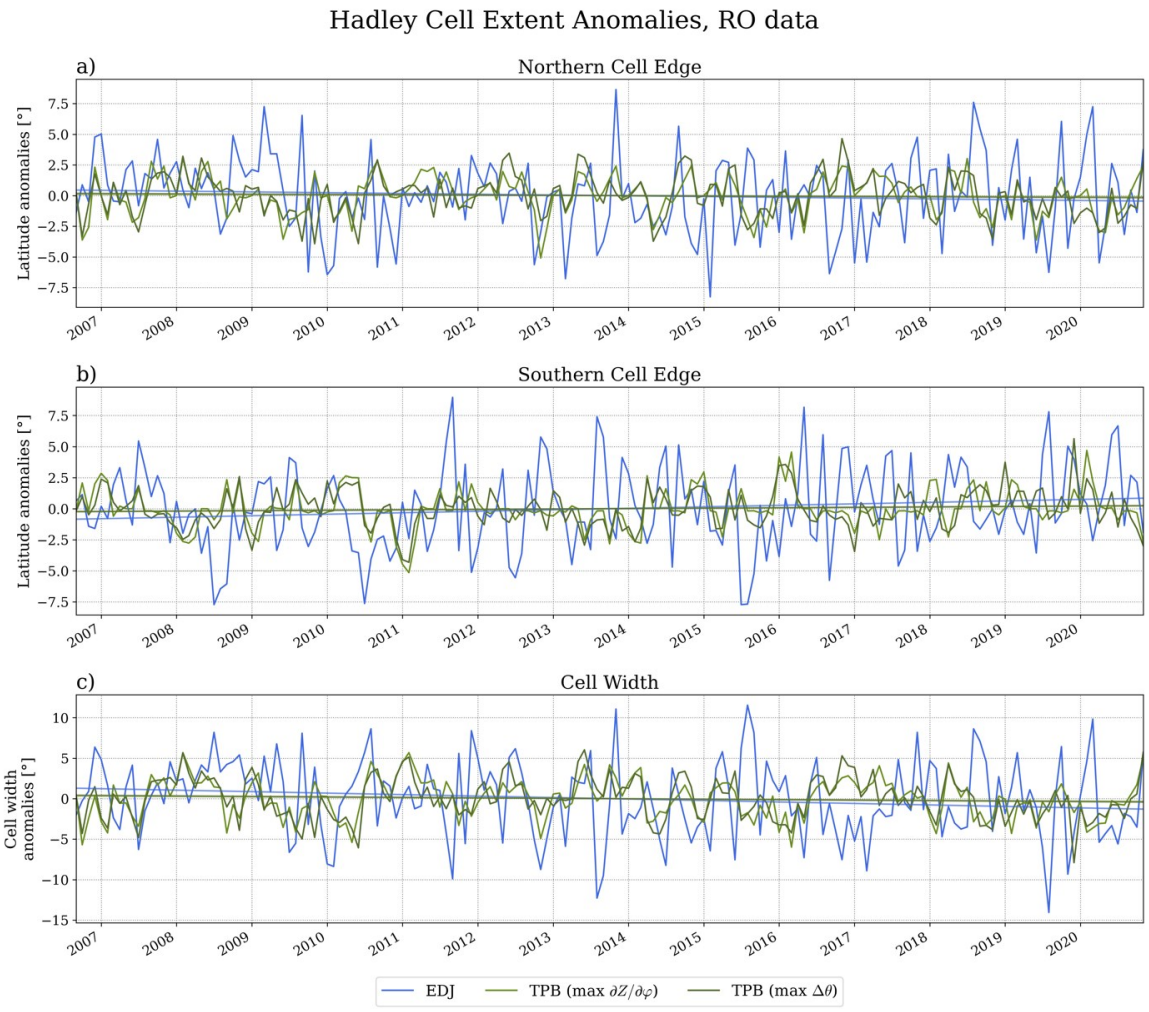

Figure 4.4: Time series and linear regression trend of the monthly Hadley cell metrics anomaly values for Ro data northern edge (a), southern edge (b) and the cell width (c) over the period September 2006 to November 2020. An anomaly value of zero indicates that the cell width corresponds to the mean over the record period.

Previous studies analyzing the Hadley cell, have explored the trends for different time averages. Figure 4.5, highlights the fact that the chosen time average, for example monthly means or annual means, can influence the results. Therefore, care must be taken, when comparing results from different studies, as the magnitude of the trend can differ significantly. Especially, for seasonal averages the trend can be distinctly increased or decreased for each metric over each season. Moreover, Figure 4.5 suggests that the comparison of different metrics for individual seasons must be done cautiously. It is necessary to first analyze the correlation between the different metrics, see for example Waugh et al. (2018).

The identified trends for RO data contrast the scientific consensus, that the Hadley cell width has been increasing over recent decades and will continue to increase as a result of climate change (see Chapter 2). As a consequence, the above results seem highly questionable and will be thoroughly examined and addressed in the concluding arguments of this thesis, see Section 4.

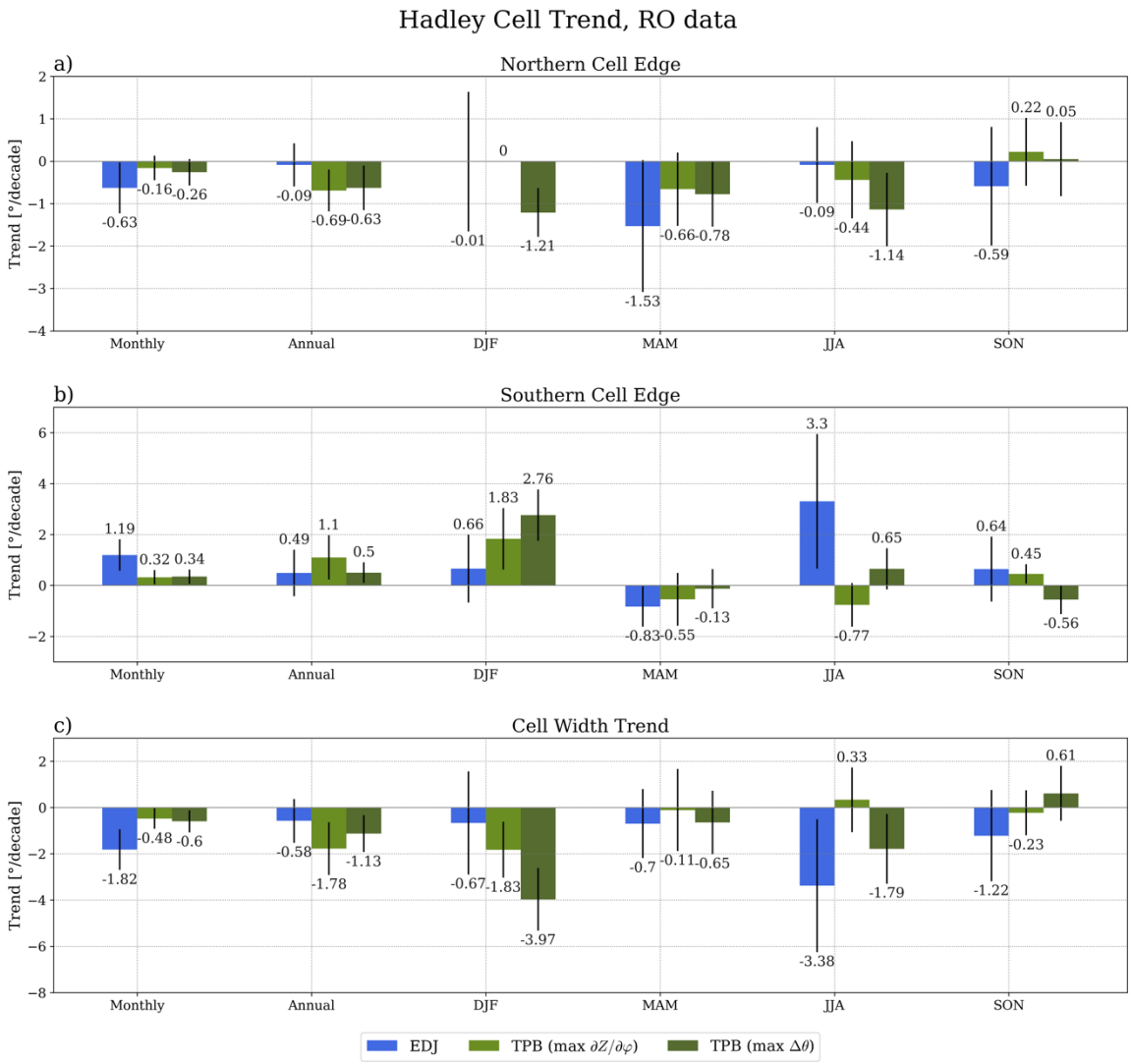

Figure 4.5: Linear regression trends for monthly, annual, and seasonal RO anomaly values for the northern edge (a), southern edge (b) and the cell width (c) over the period September 2006 to November 2020 for all metrics. The black lines indicate the ±1 standard deviation of the trend.

4.1.3 Hadley cell trend – ERA5

The first approach was to compute the trend for the same metrics and time period for ERA5 data. Besides the three metrics used for RO, also the PSI metric is applied to gain more insight. The same steps of analysis were taken as for RO. This means, initially a time series was created for all metrics, displayed in Figure 4.6. The time series of the PSI metric shows some gaps during June and July on the northern hemisphere, where the Hadley cell could not be detected by the computer program. This also leads to gaps in the cell width, and issues with the trend estimation, as the linear regression trend cannot be calculated using the same calculation method, including the missing values.

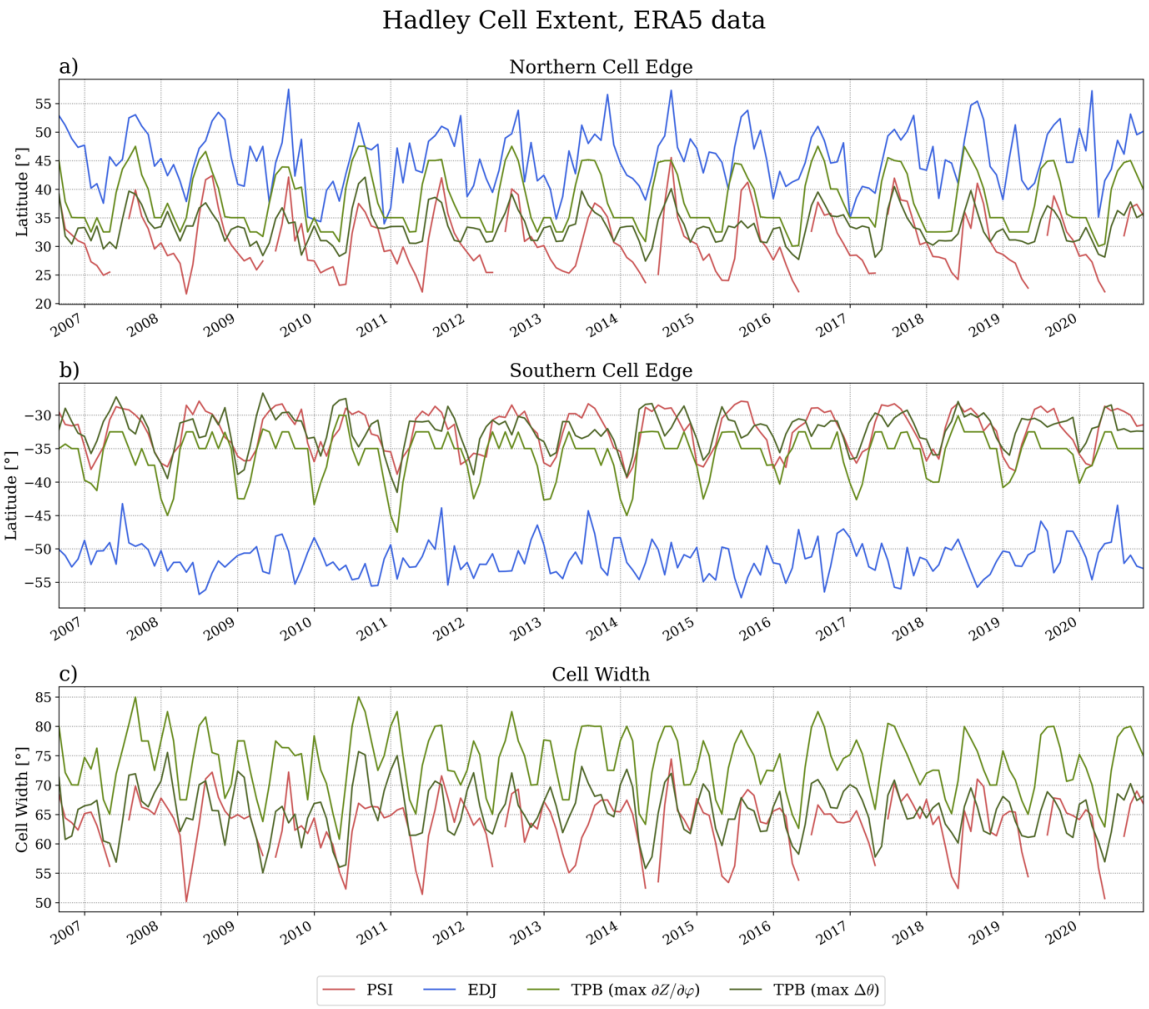

Figure 4.6: Time series of the Hadley cell metrics for ERA5 data northern edge (a), southern edge (b) and the width (c) over the period September 2006 to November 2020.

A closer inspection of the missing values was done, an example is shown in Figure 4.7. During the summer months the Hadley cell can be highly asymmetric, with a very strong circulation cell on the winter hemisphere. In case of the missing values, the summer hemisphere Hadley cell gets so weak that it is not detectable for a short while with the PSI metric. As can be seen in Figure 4.7, only the Hadley cell edge on the southern hemisphere can be located with the PSI metric. There is no clear cell structure visible on the northern hemisphere, especially at 500 hPa where this metrics tries to locate the edge of the circulation cell. The creators of the metric program indicated that this problem might occur and proposed to look at seasonal or annual mean data instead of monthly-mean data (Adam et al., 2018).

To continue this line of investigation on monthly-mean data, the time series including the missing values, so the northern cell edge and the width for the PSI metric, were linearly interpolated to fill the missing values. As mentioned above, this step was necessary to calculate a linear regression trend for the PSI metric using the same methodology as for the other trends in this thesis. It should

be noted that the trend in width does not correspond exactly to the change of the northern and southern edge, as is the case with the other metrics.

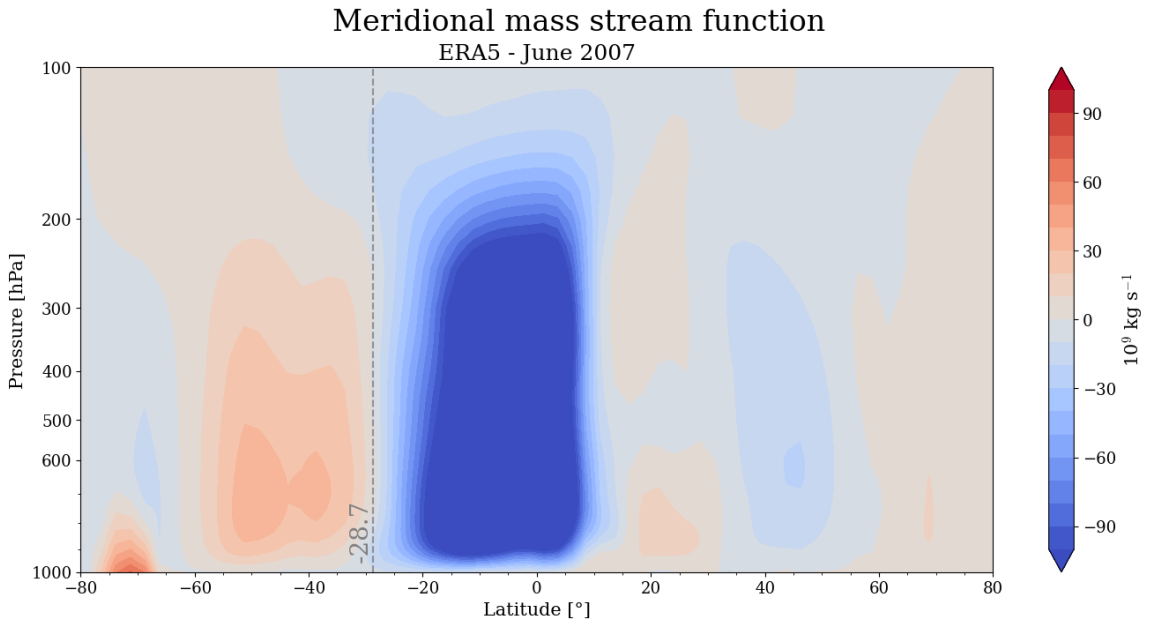

Figure 4.7: Mean meridional mass stream function for June 2007. The dashed line indicates the location of the Hadley cell edge as defined by the PSI metric. The metric was not able to identify a cell edge on the northern hemisphere.

Table 4.4, lists the linear regression trend values for monthly-mean ERA5 anomaly values, over the RO record period. On a first look, the signal and magnitude of the results appear to be alike the ones for RO, except for the EDJ metric. With this one exception for the EDJ on the northern hemisphere and the congruent width, the metrics show again an equatorward shift on the northern and southern hemisphere and a general narrowing of the width. The narrowing trend lies between 0.45° and 0.89° per decade. However, under closer inspection, besides the EDJ, also the results for the TPB (max ∂Z/∂φ) metric are quite diverse when the two datasets are compared. For example, the trend of the TPB (max ∂Z/∂φ) for ERA5 is double on each hemisphere the trend for RO. Only the results for TPB (max Δθ) are assimilable.

Table 4.4: As in Table 4.3, for monthly-mean deseasonalized ERA5 data over the period September 2006 to November 2020.

ERA5 data	**North**	**South**	**Width**
PSI	-0.285	0.181	-0.450
EDJ	0.639	0.275	0.364
TPB (max $\boldsymbol{\partial Z/\partial \varphi}$)	-0.229	0.659*	-0.888*
TPB (max $\boldsymbol{\Delta\theta}$)	-0.366	0.309	-0.675

Even though the magnitude of the results for each metric is not uniform, the signal indicates a contraction of the Hadley cell for both datasets. The results of the two investigated datasets are suggestive, that there must be a different underlying reason for the contracting trend of the Hadley cell. Thus, as a next step, the linear regression trend is calculated for an extended time period. The trend analysis is done for the whole ERA5 time span, so 1980 to 2022. The results are shown in Table 4.5. The metrics produce consistent trends for the northern and southern hemisphere as well as the width. The Hadley cell edges are moving poleward. For the northern cell edge a trend between 0.06° to 0.22° per decade can be identified, whereas the southern cell edge moves between 0.18° and 0.57° per decade. This implies that the southern cell edge is shifting more than the northern one. The resulting expansion of the Hadley cell width is between 0.25° and 0.63° per decade. The EDJ metric, which has so far delivered the most unsteady results, is now in line with the other findings. In comparison to the previous calculations, more trend results are statistically significant for the longer time period.

Table 4.5: As in Table 4.3, for monthly-mean deseasonalized ERA5 data over the period 1980 to 2020.

ERA5 data	**North**	**South**	**Width**
PSI	0.055	-0.180*	0.25*
EDJ	0.217	-0.240*	0.457*
TPB (max $\boldsymbol{\partial Z/\partial \varphi}$)	0.127*	-0.311*	0.438*
TPB (max $\Delta\boldsymbol{\theta}$)	0.060	-0.567*	0.627*

4.1.4 Trend comparison

Next the relationship between the RO and ERA5 data is considered. Figure 4.8 shows the correlation of the metrics calculated for seasonal, annual, and monthly RO and ERA5 data on both hemispheres. In general, most of the metrics and time averages are displaying a high (0.6 to 0.8), to very high (0.8 to 1), correlation. This suggest that the RO data is similarly suitable for the analysis of the Hadley cell as ERA5 and speaks for the high quality of the dataset.

On closer examination, the correlation is stronger on the southern hemisphere than the northern hemisphere. This was construed, as there are some external forcings, like for example air pollution, influencing especially the northern hemisphere (see Chapter 2.1.1) in addition to the more complex underlying topography. Hence, southern hemispheric data is supposed to be more stable in both datasets and could result in a stronger correlation. As for the different averaging periods, they appear to be performing similarly and the results are close. On the northern hemisphere monthly values correlate best, whereas on the southern hemisphere monthly values are outperformed by the annual and seasonal ones.

Two values in this plot appear suspicious, those are the ones for the annual average correlation of the TPB (max $\partial Z/\partial \varphi$) on both hemispheres. The southern outlier value seems to be exactly 1 in the graph, which suggests an error in the correlation, as a perfect correlation is most unlikely. A closer look at the data reveals that the value is not equal to one, although it is very close. The northern outlier value depicts the lowest correlation in this analysis, with a value of 0.32. In turn of these results, the input data was inspected in more detail. It appears that values for the southern half do indeed have a very high correlation. In contrast, the low correlation of the northern hemisphere results from one datapoint in the year 2008. The annual average Hadley cell edge according to the TPB (max $\partial Z/\partial \varphi$) metric is very stable at about 37.5° north for both datasets, with the exception of the year 2008 for RO data. This year has a value of close to 40° north. Another look at the longer time period for ERA5 reveals that such outliers also occur in this dataset, although in different years and not during the shorter investigation period. These types of outliers are suspected to arise from the coarse averaging to annual mean values and will not be discussed further in this thesis.

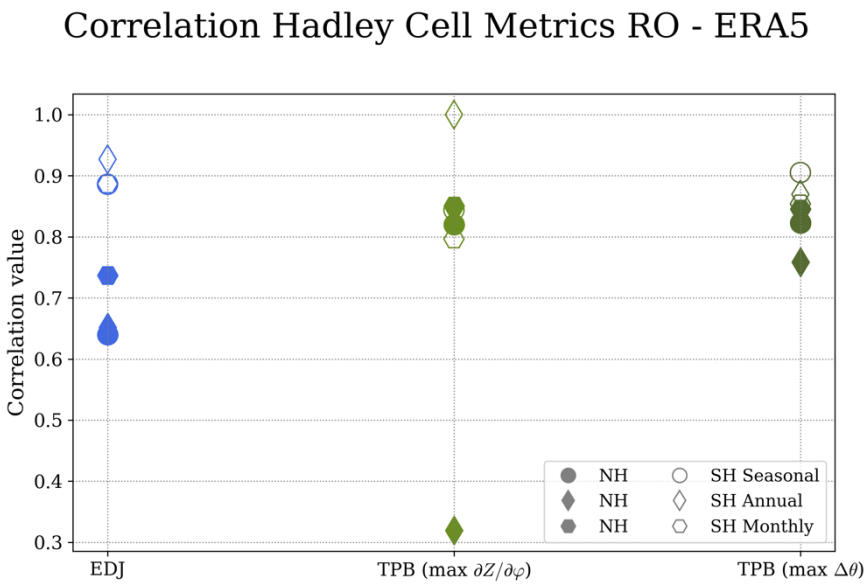

Figure 4.8: Correlation of the Hadley cell metrics for RO and ERA5 over September 2006 and November 2020, for seasonal, annual, and monthly data of both hemispheres. The time period is cut short for the annual values and does only cover the years 2007 to 2019.

4.1.5 Time period analysis

The narrowing trend of the Hadley cell width found in this analysis from RO and ERA5 data over the period September 2006 to November 2020 does not match previous findings that generally describe a widening (e.g., Staten et al., 2018, 2019; Waugh et al., 2018). Furthermore, prior RO data analysis of the Hadley cell width show varying results, ranging from a solid expansion of 1° per decade for the period 2001 to 2011 (Ao and Hajj, 2013) to slight widening trends for 2001 to 2020 data (Darrag et al., 2022). Some authors even found contracting width trends, like in this

study, although they dismissed their results for the period 2003 to 2016 and did not publish specific trend values (Luan et al., 2020). An expanding trend of the Hadley cell was found in the long-term trend for ERA5. These findings reinforce the question: is the time period of RO long enough for the trend to be distinguished from natural variability and by extension, is the trend from ERA5 stable yet. The relevance of the selected time period and its influence on the resulting trends has been previously mentioned by some authors (e.g., Xian et al., 2021) and will now be further investigated.

The stability of the trend over time for different time periods is tested by considering a rolling trend, similar to the one used by Mantsis et al. (2017). The rolling trend is comparable to a rolling mean, though instead of a series of averages, trends are calculated for a time window which shifts over the whole record period. Different window lengths are applied to comprehend the different trends from RO data investigations of the past and to speculate which record length is required to determine a stable trend.

Figure 4.9 shows the rolling trend values in ° per decade of the Hadley cell width for 10-, 15-, 20- and 30-year rolling windows. ERA5 data was used for this analysis, as it offers a longer time period, 1980 to 2022. Each datapoint represents the trend of the window concluding at this data entry. For example, the values displayed for the year 1990 for the 10-year rolling trend indicate the trend over the period 1980 to 1990. For better visualization the grid is kept at constant values of 0.5° per decade in all graphs and the time axis is kept the same. The graphs present smaller trends of the Hadley cell width change for longer time windows. Thus, the trend is getting more stable for longer time periods, this is also visualized by the zoomed in grid.

Figure 4.9 also displays how strongly the trend values change over time especially for shorter time periods. The trend windows up to 20 years show great fluctuations between smaller and greater, positive and negative trends for all metrics. Moreover, one or two additional years can influence the according trend value strongly. This can explain the great variety of trend results from past RO analysis and the contracting trend found in this investigation. Negative trends for multiple metrics are found in the late 2010s for up to 20 year rolling windows. The period for which RO data is available is about 15 years and is located in this time range.

For the 30-year rolling window the trend is starting to become more stable. TPB (max $\Delta\theta$) shows a gradually decreasing trend of 1.5° per decade to 0.75° per decade as the 30-year window is moved in time. TPB (max $\partial Z/\partial\varphi$) is less stable between 1° per decade and no change at all for the calculated 30-year trends. The PSI metric shows the most consistent trend with values around 0.25° per decade. Contrary the EDJ is still varying around zero, with more positive trend results in recent years of up to 0.75° per decade.

This analysis illustrates that the available time period for RO is not long enough to determine a trend of the Hadley cell edge change. The time series of the Hadley cell width for both datasets is presumed to be shadowed by natural variability, like ENSO and the PDO, as well as Antarctic ozone depletion. The next chapter considers a multiple linear regression to improve the trend results and identify the global warming signal.

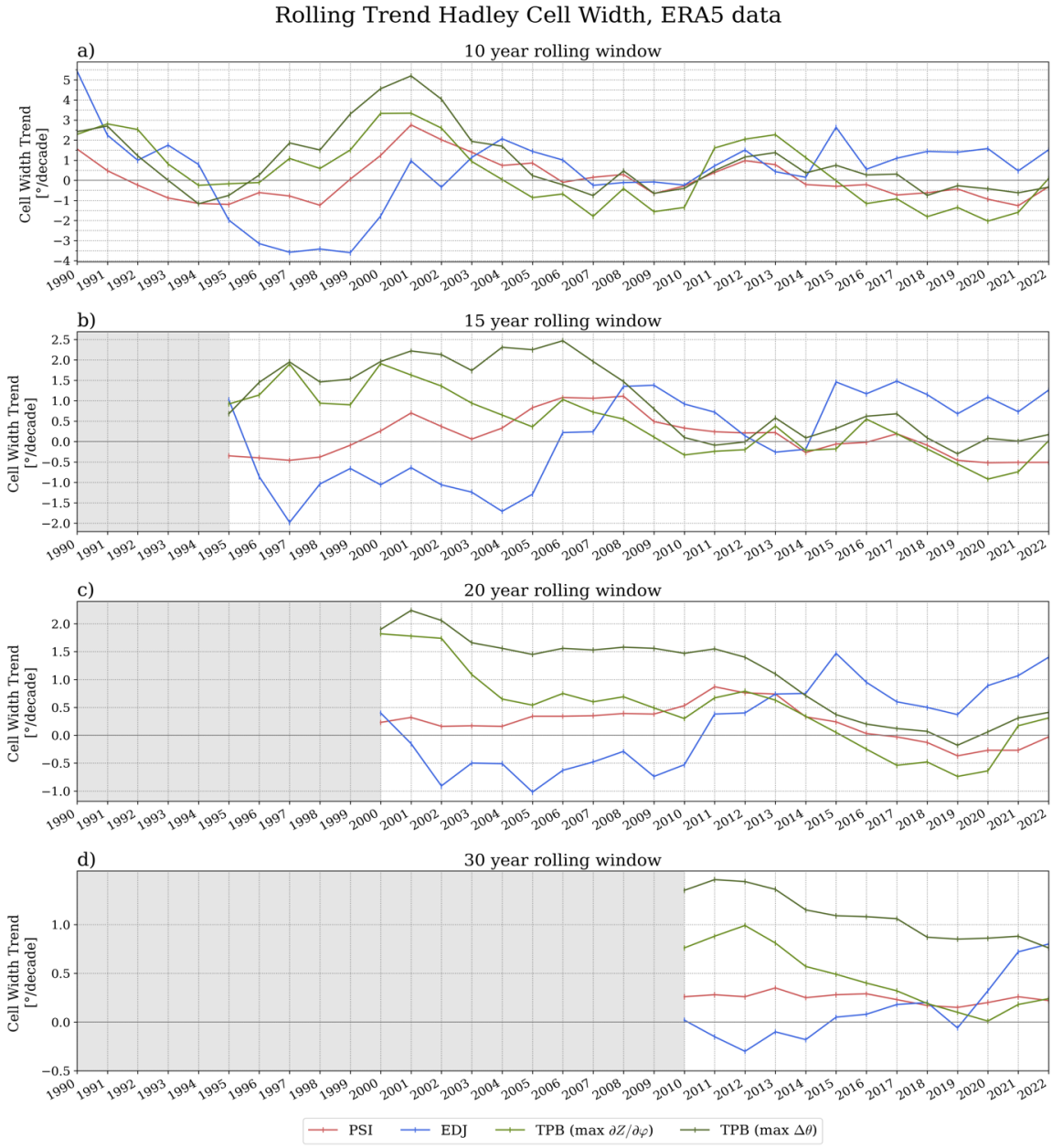

Figure 4.9: Rolling trend of the Hadley cell width for ERA5 data. A 10- (a), 15- (b), 20- (c) and 30-year (d) rolling trend for the available data 1980 to 2022 was calculated. The trend values indicate the end year of each rolling trend window. Independent of the window length the trend is given in ° per decade.

4.2 Results of the multiple linear regression

A multiple linear regression analysis is performed, with the aim to improve the stability of the Hadley cell width trend. The result section of the multiple linear regression analysis consists of three parts. First, the correlation analysis between the indices themselves and between the indices and metrics is presented. Secondly, the lead-lag analysis is discussed. On the basis of these two types of study, a decision is made as to which indices to use in the multiple linear regression that will be presented at the end.

4.2.1 Correlation analysis

Figure 4.10 displays the correlation of the identified indices. The purpose of the plot was to investigate the relationship between the individual indices for ENSO and the PDO as it is important for the multiple linear regression analysis that the independent variables are not collinear. Collinearity can result in a loss of information in the model, especially when interpreting the individual effects. Four indices for ENSO and two indices for the PDO are under consideration. On a first glance one can see that the ENSO and PDO indices correlate strongly amongst themselves, indicated by the darker turquoise color. A high positive correlation between the ENSO and PDO indices was expected and can also be seen in the graph. The correlation lies between 0.40 and 0.56. The highest value arises between the MEI.v2 and the PDO HadlSST3 index, the lowest from the Niño3.4 and PDO index from ERSST.v5 data. For these two variables, all results are statistically significant with p-values below 0.05.

The ozone index, OMD, was also tested and shows no correlation with ENSO, between -0.02 to -0.07, although these results are not statistically significant. In comparison the correlation between the PDO and OMD is statistically significant at -0.18 to -0.21, which is still a very low correlation.

A second correlation was performed between the indices and metrics, to see if any index for ENSO and PDO performs better for the individual metrics. The information is presented in Figure 4.11. The northern correlation displays negative correlation coefficients, whereas the southern half shows positive values, for the ENSO and PDO indices. This can be connected to the understanding that an expansion or contraction of the Hadley cell in the northern and southern half is associated with opposite trend values for the cell edges. In other words, ENSO and PDO correlate with a widening or narrowing of the Hadley cell on both hemispheres, where positive SST anomalies coincide with a contraction of the circulation cell.

In regard to the different metrics, the correlation varies, although the correlation values between the individual indices for ENSO and PDO are quite similar. With a focus on ENSO of the northern hemisphere, MEI.v2 has the greatest correlation, the Niño3.4 indices for HadlSST1 and ERSST.v5 perform slightly less but similarly and the relative Niño3.4 ERSST.v5 has the lowest correlation

values. On the southern hemisphere, the results are even closer together, the Niño3.4 ERSST.v5 exhibits the lowest correlation values and the MEI.v2 still shows the greatest for most metrics. For the PDO on the northern hemisphere, the HadlSST3 dataset presents marginally greater correlation coefficients, except for the EDJ. The results from the southern hemisphere are opposite, the ERSST.v5 dataset performs best for all metrics. Thus, so far, no clear preference is apparent from this line of investigation for the choice of ENSO and PDO index.

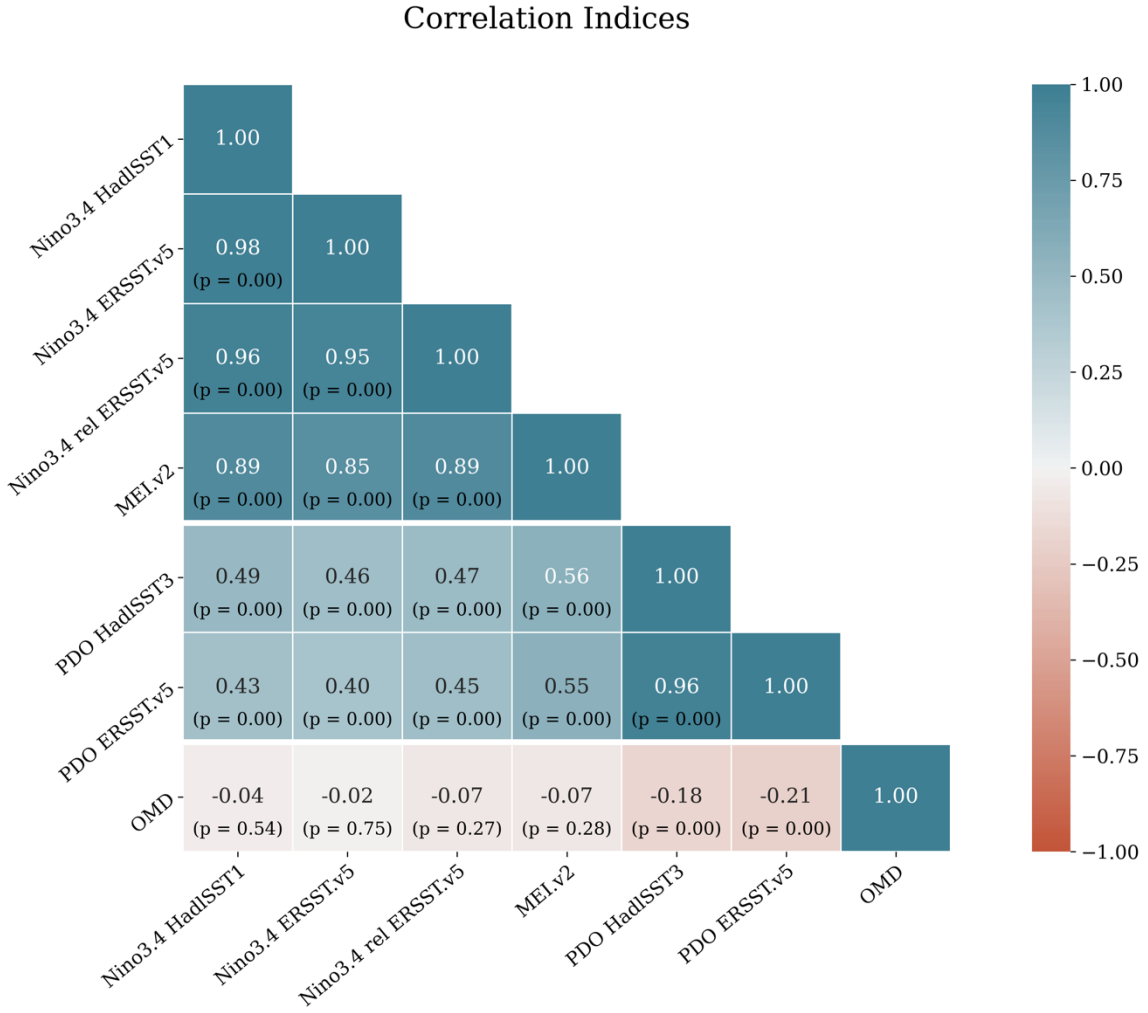

Figure 4.10: Pearson correlation coefficients for the different ENSO and PDO indices over the period 1980 to 2022 for monthly data are displayed. The p-value of each correlation is presented below the correlation coefficient.

It is also interesting to look at the correlation of ENSO and PDO with the metrics, disregarding the different indices in detail. For example, the correlation with ENSO on the northern hemisphere, the TPB metrics show the highest values, between -0.29 to -0.41. Contrary, the PSI only shows a correlation of -0.11 to -0.19. The smallest coefficients are calculated for the EDJ, -0.05 to -0.08, although none of the four correlations is statistically significant presenting p-values above 0.08. All other ENSO correlations on the northern half have a p-value below the set threshold of 0.05. The

correlation with the PDO is quite consistent over all metrics between -0.19 to -0.3, with all values being statistically significant. The highest value is produced for TPB (max $\partial Z/\partial \varphi$).

For the southern hemisphere and ENSO, the TPB (max $\Delta\theta$) has the greatest correlation, 0.31 to 0.38, followed by the PSI metric, 0.26 to 0.31, and TPB (max $\partial Z/\partial \varphi$), 0.19 to 0.25. The EDJ metric is again hardly correlated, with values of 0.06 to 0.08. For the PDO the correlations look similar to the northern ones, TPB (max $\Delta\theta$) now shows the strongest connection. One major difference is the correlation between the PDO and the EDJ, as there is none, with values of 0.02 to 0.06. Similar, to the results of the northern hemisphere, the p-values of the southern hemisphere are statistically significant for all metrics except the EDJ.

Finally, one can assess the connection between the metrics and ENSO and PDO on each hemisphere, which natural mode has the greater connection. On the northern half PSI and EDJ correlate stronger with the PDO than ENSO. Contrary, ENSO correlates more with the TPB metrics. On the southern half both ENSO and PDO show similar correlations to the individual metrics, with the exception of the PSI which slightly selects ENSO.

As for the results for the OMD, the barely existing correlation on the northern hemisphere is positive and negative on the southern hemisphere. This is in line with the understanding that an increase of the ozone hole, growing OMD values, results in a contraction of the Hadley cell, thus negative trend values on the southern hemisphere and positive ones on the northern one. The OMD index, shows no correlation with any of the metrics, a reason could be the use of monthly average values. An investigation of annual average reveals low to moderate correlations for most metrics and hemispheres, the plot is not shown. Greater correlation would also be expected from seasonal analysis, especially during the DJF season.

As a result of both correlation investigations, the Niño3.4 and PDO index from ERSST.v5 data is chosen. The analysis showed that there is not really one index better suitable for the following regression analysis. All show similar correlations with each other and with the metrics. The suitability of the OMD index for the regression analysis could not be shown in Figure 4.11, but was identified for annual values.

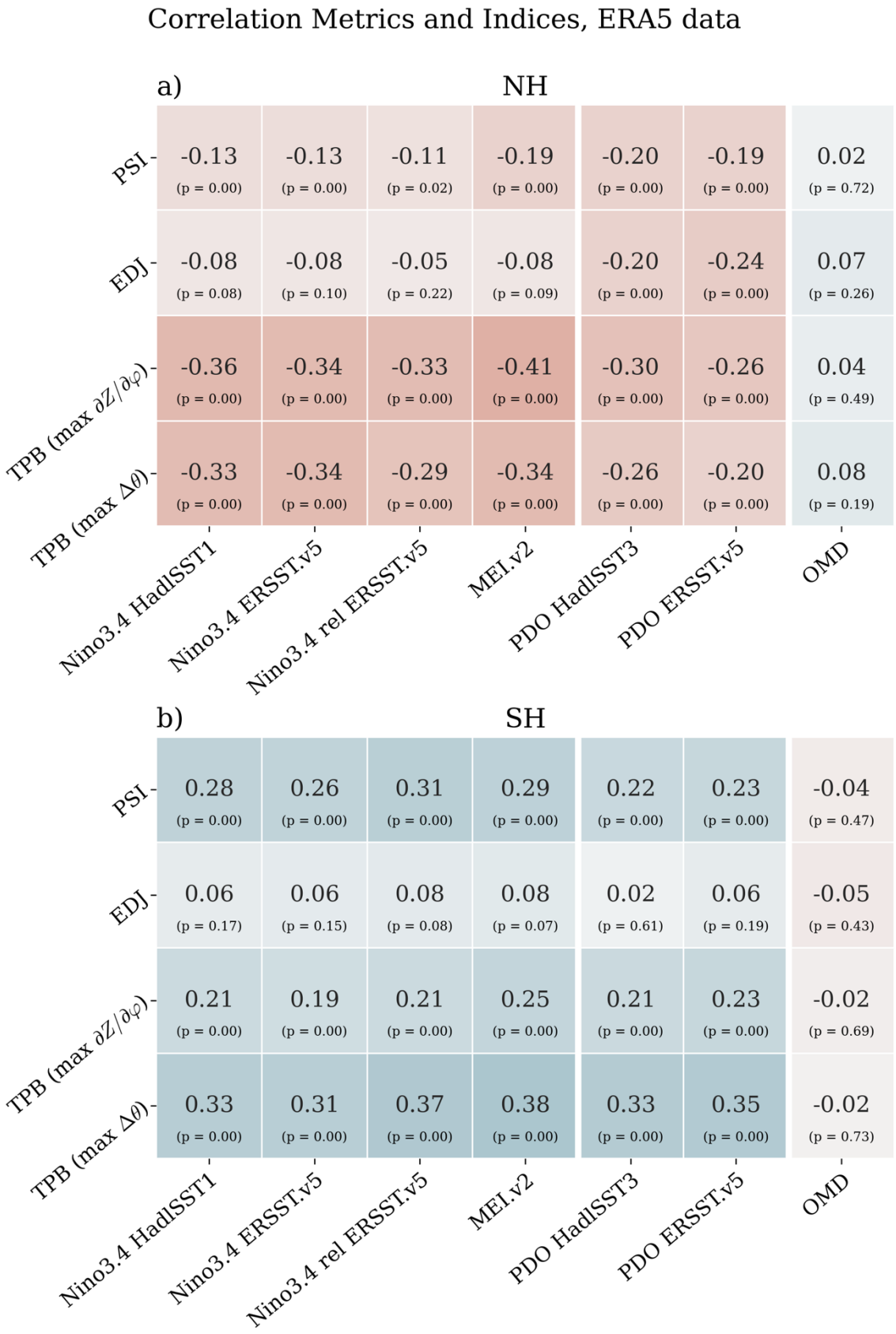

Figure 4.11: Pearson correlation coefficient for the individual Hadley cell edge metrics for the northern (a) and southern hemisphere (b) for monthly ERA5 data 1980 to 2022 and the ENSO, PDO and OMD indices. The p-value of each correlation is displayed below the correlation coefficient. The same color bar as in Figure 4.10 is used.

4.2.2 Lead-lag analysis

A lead-lag analysis, shown in Figure 4.12, for all the indices on the metrics for ERA5 data from 1980 to 2022 was performed for the northern and southern edge and the width of the Hadley cell. In other words, the correlation of the indices and metrics was investigated when the index was shifted up to twelve months into the past or future of the metric value. Again, all the different indices for the three variables were included in the investigation, to see if any one index stands out particularly at some lag. The focus lies on the Niño3.4 and PDO index from the ERSST.v5 dataset, which were singled out in the prior correlations. As in previous correlation analysis, the different indices for the variables ENSO and PDO among themselves perform very similarly. The curve over the different lags follows the same pattern for each individual variable. Additional plots of the cross correlation for ERA5 over the period September 2006 to November 2020 and RO are displayed in Appendix B.

The most interesting lead-lag relationship in this graph, Figure 4.12, is seen for ENSO. Throughout the single plots, the correlation with ENSO shows a peak for up to half a year lag of the metric, hence ENSO leads the metric up to six months. The TPB metrics appear to have a more uniform lag value for the southern and northern edge and the width in comparison to the PSI and the EDJ. The biggest discrepancies between the hemispheres can be seen for the PSI metric. The lag is six months on the northern half, whereas on the southern hemisphere the PSI reacts instantly according to the correlation.

The correlation of the metrics with the PDO shows more of a direct connection in time. The highest correlation values can be found at zero to one month lag of the index. This can probably be explained by the longer time scales of the PDO in comparison to the monthly lead-lag investigated here. Generally, the results of the southern half are less clear, with more steady results for the different lags and smaller correlation peaks spread more randomly along the lags. On the northern hemisphere, and as a result also for the width, a more definite result can be found.

Next, the OMD index is considered. In comparison to all the other indices, the OMD shows hardly any statistically significant results. Only for the TPB metrics results significant at the 95% confidence interval can be found, although they also only fully coincide for both metrics at a peak at seven to eight months leading the index. For the other metrics the correlation results fluctuate around the zero line for both edge values and the width. This is in accordance with the previously found results, which also did not really show a correlation for monthly values. As mentioned above, a stronger connection of the OMD and the metrics could be found for an investigation of annual values.

Interestingly, when comparing all the results from all the metrics, the EDJ metrics shows the plot with the least correlation and statistically significant results of all graphs for the southern

hemisphere. Only the positive lags for ENSO and a couple of negative lags for the PDO meet the p-value criteria. The EDJ has also shown less correlation to the indices in the previous figure.

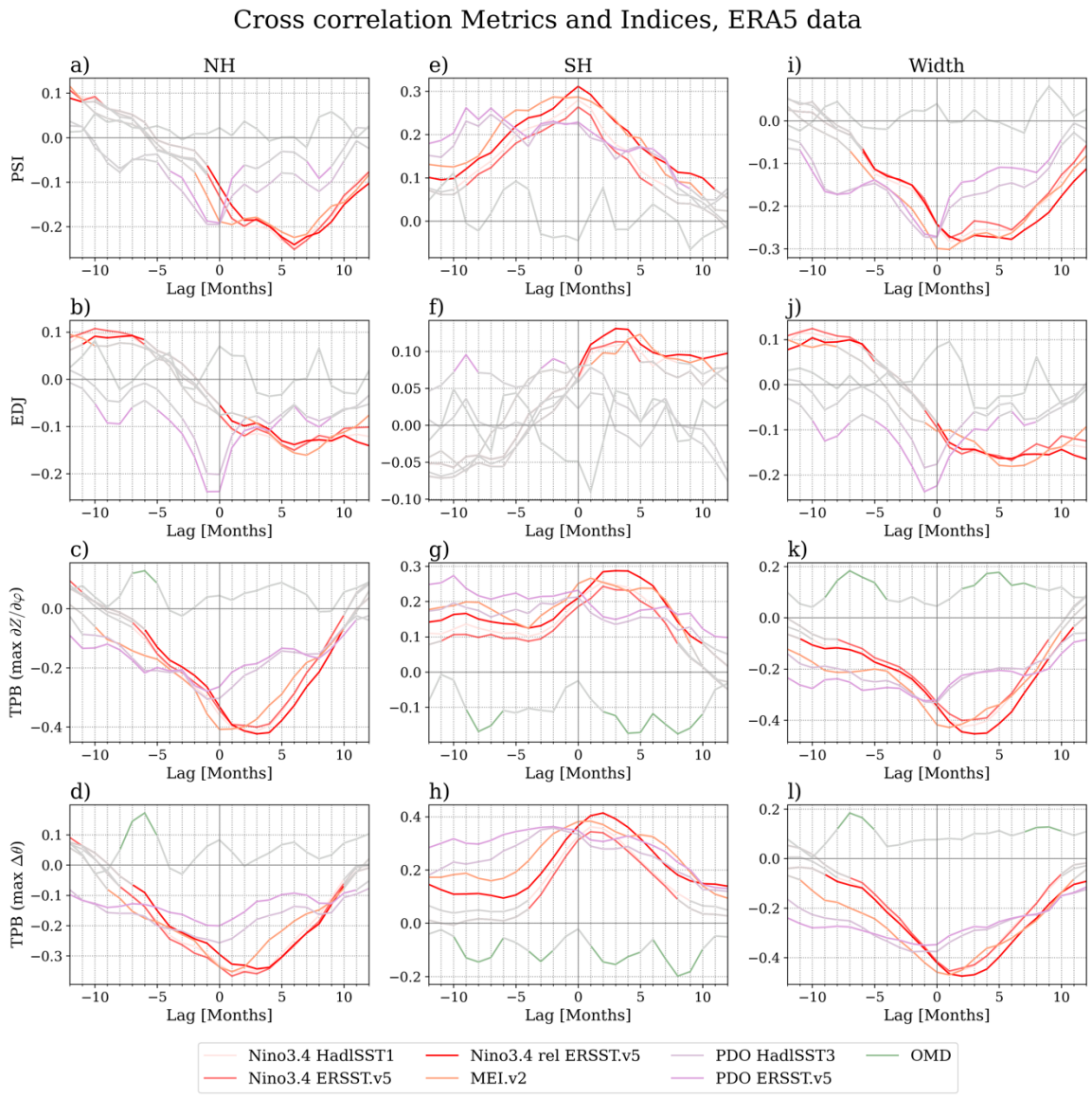

Figure 4.12: Cross correlation of the lagged indices for each metric on the northern hemisphere (a-d), southern hemisphere (e-h) and Hadley cell width (i-l). This analysis was performed on ERA5 data for the time period 1980-2022. The lag correlation span is ±12 months. A positive lag indicates that the index leads the metric, thus the metric lags the index. Correlation values which are not statistically significant at the 95% confidence interval are displayed in a gray color. The color scheme matches the previous figures, with the exception of the PDO indices which are displayed in a plum color. ENSO indices are held in a reddish tone, OMD values are in sea green.

Concluding the information gained from Figure 4.12, different lags are used for the variables in the following regression analysis for the PDO and ENSO. For the OMD no lag is chosen, as the results do not seem to be conclusive. The lags applied for ENSO and the PDO in this regression analysis are displayed in Table 4.6. Some of the lags for the PDO on the southern hemisphere do not

correspond to the maximum correlation, the reason for this is that no particular correlation values stand out, they appear to be all in the same order of magnitude.

Table 4.6: Lag values used in the regression analysis for the ENSO index Niño3.4 rel ERSST.v5 and PDO index PDO ERSST.v5, as established in Figure 4.12 for ERA5 data 1980 to 2022.

ERA5 data	**North**		**South**		**Width**	
	ENSO	PDO	ENSO	PDO	ENSO	PDO
PSI	6	0	0	-2	2	0
EDJ	6	-1	3	-2	5	-1
TPB (max $\boldsymbol{\partial Z/\partial \varphi}$)	3	-1	3	0	3	-1
TPB (max $\Delta\boldsymbol{\theta}$)	3	0	2	-2	2	-1

Table 4.7 and Table 4.8 list the lag values for ENSO and the PDO for ERA5 and RO data over the period September 2006 to November 2020, respectively. Over the analyzed lag period of ±12 months, much less results are statistically significant, and the lags were thus chosen more considerably. In particular the lags for the EDJ metric from ERA5 for the short time period and ENSO, did not appear plausible considering previous results, therefore the values from Table 4.6 were taken. Another interesting detail is, the RO data shows the least lag, the metrics seem to be connected more directly in time.

Table 4.7: Lag values used in the regression analysis for the ENSO index Niño3.4 rel ERSST.v5 and PDO index PDO ERSST.v5, as established in Figure B.1 (see Appendix B) for ERA5 data September 2006 to November 2020.

ERA5 data	**North**		**South**		**Width**	
	ENSO	PDO	ENSO	PDO	ENSO	PDO
PSI	7	0	0	0	7	0
EDJ	6	0	3	0	5	0
TPB (max $\boldsymbol{\partial Z/\partial \varphi}$)	1	-1	1	0	1	-1
TPB (max $\Delta\boldsymbol{\theta}$)	1	0	1	-1	1	0

Table 4.8: Lag values used in the regression analysis for the ENSO index Niño3.4 rel ERSST.v5 and PDO index PDO ERSST.v5, as established in Figure B.2 (see Appendix B) for RO data September 2006 to November 2020.

ERA5 data	**North**		**South**		**Width**	
	ENSO	PDO	ENSO	PDO	ENSO	PDO
EDJ	0	-1	0	0	0	-1
TPB (max $\boldsymbol{\partial Z/\partial \varphi}$)	3	0	2	0	2	0
TPB (max $\Delta\boldsymbol{\theta}$)	1	0	2	0	2	0

4.2.3 Multiple linear regression trend

Following the above investigation of the correlation, three indices for the multiple linear regression analysis were picked, those are the Niño3.4 and PDO index from the ERSST.v5 dataset and the OMD index. The next step, as described in the methods section 3.2.4 was to detrend the index for ENSO. Conveniently, a corresponding dataset is available for download and hence has been continually investigated in this assessment besides the none detrended ones, namely the Niño3.4 rel ERSST.v5. Based on these indices and lags, the variability was regressed out and the results of the remaining trend are displayed in the following tables. Table 4.9 lists the residual trend for ERA5 data over the period 1980 to 2022 and Table 4.10 and Table 4.11 show the residual trend results over the period September 2006 to November 2020 for ERA5 and RO respectively. Except for some southern edge and width trends for the long ERA5 dataset, no residual trend values are statistically significant.

Table 4.9: List of the Hadley cell trend values in ° per decade with variability regressed out for the northern and southern edge and the cell width, for monthly-mean deseasonalized ERA5 data over the period 1980 to 2022. The trend is given in ° per decade. Statistically significance is assumed for p-values < 0.05, the congruent results are marked with an asterisk (*).

ERA5 data	**North**	**South**	**Width**
PSI	-0.143*	-0.083*	-0.049
EDJ	-0.127	-0.143	0.029
TPB (max $\boldsymbol{\partial Z/\partial \varphi}$)	-0.003	-0.18*	0.179*
TPB (max $\Delta\boldsymbol{\theta}$)	-0.076	-0.36*	0.293*

Table 4.10: As in Table 4.9 for monthly-mean deseasonalized ERA5 data with the variability regressed out over the period September 2006 to November 2020.

ERA5 data	**North**	**South**	**Width**
PSI	-0.09	0.072	-0.179
EDJ	0.852	0.305	0.537
TPB (max $\boldsymbol{\partial Z/\partial \varphi}$)	-0.083	0.366	-0.464
TPB (max $\Delta\boldsymbol{\theta}$)	-0.24	0.013	-0.266

Table 4.11: As in Table 4.9, for monthly mean deseasonalized RO data with the variability regressed out over the period September 2006 to November 2020.

RO data	**North**	**South**	**Width**
EDJ	0.013	0.918	-0.798
TPB (max $\boldsymbol{\partial Z/\partial \varphi}$)	0.053	0.036	-0.006
TPB (max $\Delta\boldsymbol{\theta}$)	-0.138	0.061	-0.178

To allow for a better comparison of the results, in addition to the tables, the trend values of the linear regression analysis for the edited datasets are displayed in Figure 4.13 next to the originally calculated trend for each dataset. Generally, in most cases the residual trend is smaller than the one form the original time series. Some results, like the PSI for the long ERA5 series on the northern hemisphere, even change their direction. In this particular case, the initial result showed an expansion, whereas the newly calculated trend shows a narrowing of the cell.

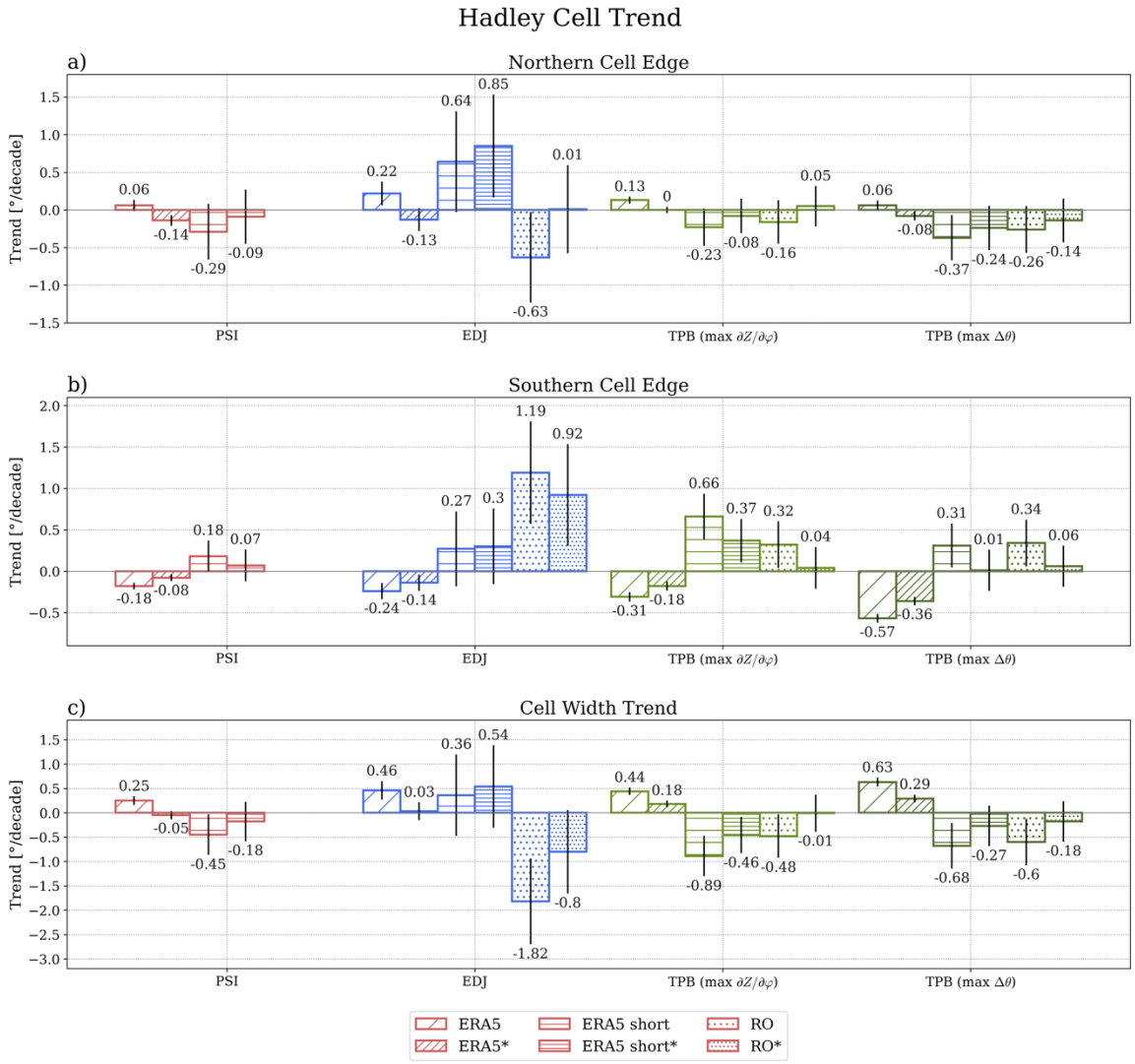

Figure 4.13: Linear trends for ERA5 over the whole and shorter time period, as well as RO data and the trend for the datasets where ENSO, PDO and ozone forcing is regressed out, indicated by an asterisk (*). The trend for each metric from each dataset is displayed for the northern (a) and southern (b) edge and the cell width (c). The black lines indicate the ±1 standard deviation of each trend result.

The spread of the trend for the residual time series and different metrics is smaller, than the one for the original trends. For the long ERA5 record the Hadley cell width change lies between an expansion of 0.29° per decade and a narrowing of 0.05° per decade. The shorter period for ERA5 stretches from a widening of 0.54° per decade to a contraction 0.46° per decade and the RO residual

shows a narrowing between 0.8° per decade and 0.01° per decade. Thus, the results for ERA5 do not show a consistent trend between the metrics for the adapted time series, as the sign of the signal varies. Nevertheless, the spread of the RO trends is also wide with great standard deviation values crossing the zero line.

For the northern hemisphere, the trend results for each metric and dataset are very diverse. For example, three out of four metrics show a change in sign for the long ERA5 dataset. All metrics indicate a narrowing for the residual trend, except TPB (max $\partial Z/\partial \varphi$) which denotes that the cell edge location remains the same, so there is no trend. For the TPB (max $\Delta\theta$) metric all datasets, but the original long ERA5 one, show an equatorward shift of the northern cell edge. This result is the most consistent one between the datasets for both hemispheres and metrics. For the residual time series, the trend for the TPB (max $\Delta\theta$) metric shows a contraction of the northern cell between 0.08° per decade to 0.24° per decade.

On the southern hemisphere the results from each dataset are more consistent. Even though the magnitude of the residual trends changed, the overall direction of the signal remains. This means for ERA5 data over the period 1980 to 2022 the Hadley cell is expanding. Contradictory, for the two shorter time periods for ERA5 and RO the cell is contracting for all metrics. Moreso, the trends on the southern hemisphere are larger for most metrics and datasets than on the northern half.

5 Summary and conclusions

In this thesis, the utility of RO data for the analysis of the Hadley cell changes along with anthropogenic climate change was investigated. A focus was set on the possible added value from high-quality RO OPSv5.6 data, despite its relatively short available time span of about 15 years. In addition to the RO dataset, ERA5 reanalysis data were used for comparative purposes and to gain further insight into the utility of datasets with shorter record periods by intercomparing also longer multi-decadal periods.

In a first step, suitable metrics were identified, those are the eddy driven jet (EDJ) and two tropopause break metrics TPB (max $\partial Z/\partial \varphi$) and TPB (max $\Delta\theta$). Another metric previously calculated from RO data is the subtropical jet (STJ); this metric was not considered in this thesis, since recent studies have shown a disconnect between the Hadley cell and the STJ (Menzel et al., 2024, 2023). Furthermore, the mass stream function was explored. Research mentions that this metric can be derived from the mean meridional wind, so the v-component (e.g., Adam et al., 2018). On closer inspection, the divergent part of the meridional wind revealed itself to be the necessary information for the calculation of the PSI. The divergent information is not included in the approximated winds derivable from RO geopotential fields thus far, so the metric cannot be computed, even though in general the (mean) meridional wind can be approximated very closely.

In a second step, the time series of the RO and ERA5 record for the northern and southern latitudinal edge of the Hadley cell as well as the overall interhemispheric width of the circulation got evaluated. A contracting trend for nearly all metrics and measures was found for RO and ERA5 over the 15-year time period, September 2006 to November 2020, with the exception of the northern edge and width trend from the EDJ metric for ERA5. For the longer multi-decadal period of the ERA5 reanalysis record, 1980 to 2022, all metrics indicated an expansion of the Hadley cell circulation on both hemispheres. This is in agreement with the results from previous long-term studies. Although, the results from the shorter and longer periods are contradicting, no conclusions can be drawn about the possible overall added value from RO based on just these results. A correlation of the metric results from the two datasets was hence calculated. The results show a high correlation between the two datasets, indicating the basic high quality of RO data.

Next, a range of different time periods was analyzed to better understand the mixed results from previous Hadley cell width studies. For this, rolling trends were computed based on the long multi-decadal record of ERA5. Specifically, the trend for the latitudinal width of the Hadley cell was

examined for 10-, 15-, 20- and 30-year rolling windows. This analysis showed that the trend becomes more stable with smaller overall values for longer time periods, although the results still differ among the various metrics. The PSI shows the most stable results, indicating a Hadley cell expansion of about 0.25° per decade for the 30-year rolling windows. Other metrics, such as the two TPB metrics, also indicate an increasing trend in the cell width, although the overall trend is decreasing for more recent time windows of this size. The results are the least stable for the EDJ metric. The earlier windows of the 30-year trend show a narrowing of the cell, while more recent periods indicate an expansion. This analysis suggests that a much longer time record for RO is required for trend significance, and even the trends based on the over-40-year reanalysis period of ERA5 since 1980 may still be partially concealed, by natural variability and other side influences like ozone changes. It is important to emphasize that RO data are continuously available since the year 2001 and that new satellite missions have been launched, such as the COSMIC-2 mission, and future ones are planned, all these favorably ensuring a growing length of the record, compared to the one used in this thesis. In addition, the processing of RO is subject to ongoing improvements (e.g., Steiner et al., 2020), which also benefits the quality of long-term trend analysis.

Finally, a multiple linear regression model was applied to remove the influence of the previously discussed modes of natural variability and of ozone change. As mentioned earlier, studies have suggested that the trend of the Hadley cell has not yet emerged from natural variability. The two most important modes in this context are ENSO and the PDO. Both modes have a significant impact on the width of the Hadley cell and therefore removing their additional trend can help stabilize the results of the trend analysis. The addition of ozone to the regression model may seem counterintuitive as it is an anthropogenic external forcing. However, the discussed literature indicates that the effect of ozone changes has caused the Hadley cell to extend more strongly in the last decades of the past century and the opposite effect of ozone recovery is affecting the trend during this century. Therefore, by removing these ozone effects, one can expected to be able to better compare the trends of the shorter and longer time periods.

The results of the residual trends, after removing the effects of ENSO, PDO and ozone changes, show slightly smaller trend values. For the width, the trends of all metrics and datasets, with the exception of the PSI for the long-term ERA5 trend, remain true to their sign. For the northern hemisphere edge, the trends of the long ERA5 time period change their signs, meaning that most trends indicate a contraction of the northern hemisphere Hadley cell. In particular, the results of the TPB (max $\Delta\theta$) metric stand out. The trend of the long ERA5 record is now more aligned with the shorter RO and ERA5 study periods, with an indicated contraction of the northern Hadley cell from 0.08° per decade to 0.24° per decade for the different datasets. This result contradicts the general understanding that the Hadley cell expands with climate change. One may speculate that this possibly indicates the importance of tropospheric ozone and anthropogenic aerosols, which are

heavily emitted from the northern hemisphere countries and could lead to a contraction of the circulation, as discussed in Chapter 2.1.1. For the southern hemisphere, the direction of sign of the residual trends remains the same, with the longer time period showing a widening trend in contrast to the narrowing trend of the shorter investigation period. Thus, the difference between the shorter and longer trends on the southern hemisphere cannot be explained by ozone changes alone, and a more detailed attribution study of the trends would be interesting. The scope of future work could also include other interesting indices to further improve the multiple linear regression model. For example, an index of the Arctic Oscillation, which has a strong influence on the northern circulation cell, and for major volcanic eruptions, could be valuable additions to a refined regression model.

As for the results of the individual metrics, the two TPB metrics performed similarly. However, the trends of the two TPB metrics from RO appear to be smaller than those from the ERA5 dataset. It is speculated that this is possibly due to the higher vertical resolution of the RO dataset. The results for RO from the EDJ metric appear questionable. The trend values are much larger than for the other metrics and datasets. One reason may be the background information influencing the RO record in the troposphere, as RO is not an independent dataset at the necessary altitude level of this metric (e.g., Steiner et al., 2020). Yet, the results from ERA5, especially from the long record, are in line with the other metrics from the same dataset. Thus, the EDJ should not be disregarded as a metric for the Hadley cell completely. Overall, the trend signal detected in this investigation is rather small, for all datasets and metrics. Moreover, the multiple linear regression analysis shows that a relatively large part of the signal can be attributed to other influences, in this case ENSO, PDO and ozone changes. This research suggests that the expansion of the Hadley cell, although theoretically explained and reported in climate model simulations, may not be the best indicator of climate change, as the global warming signal appears to be relatively small compared to the co-influence of natural variability and further forcings.

In conclusion, the available time span for RO data is too short to analyze the overall trend of expected Hadley cell widening along with anthropogenic climate change. A much longer record is needed for the trend of global warming to emerge from natural variability and the influence of less understood external forcings, such as aerosols or tropospheric ozone. However, in correlation to the results of the shorter ERA5 record, RO does still seem promising. Additionally, the application of a refined multiple linear regression model could improve the results from such trend analyses. Added value could stems from the global coverage and high vertical resolution of RO data and deserves additional future work.

A. Deriving a wind field

To analyze the previously selected Hadley cell width metrics, additional to the temperature data, wind field information is necessary. Based on the geopotential derived from RO data, wind fields can be calculated by the geostrophic and gradient wind approximation (e.g., Scherllin-Pirscher et al., 2014; Verkhoglyadova et al., 2014). The geostrophic wind is given by the exact balance between the Coriolis force and the pressure gradient force in the free atmosphere, where friction can be ignored. Hence, the horizontal velocity in the middle to high latitudes can be described with the geostrophic approximation to within 10% (e.g., Holton and Hakim, 2012; Wallace and Hobbs, 2006). Via this equation the zonal (u) and meridional (v) component of the wind can be estimated. The geostrophic and gradient wind approximation has been previously thoroughly investigated by Nimac et al. (2024, 2023). However, both approximations are only usable outside the equatorial region. Close to the equator, the term of the Coriolis force approaches zero. Thus, the balance is not valid anymore. More recently, a study by Danzer et al. (2023) presented an approach to fill the tropical wind field data gap, by applying the equatorial balance equation for the ±5° latitude scope, creating a wind field over the whole globe. The equatorial balance equation was previously suggested by Fleming and Chandra (1989) and Chandra et al. (1990), and further investigated by Scaife et al. (2000) and Healy et al. (2020).

The presented work will built on the recent findings and methods of Danzer et al. (2023) and investigate some aspects of the calculation method in more detail. After an introduction of the wind field equations, several finite difference methods will be compared. Subsequently, the interpolation method, linear or cubic spline, for the equatorial balanced wind will be examined. Finally, another approach to the calculation sequence, implemented by Healy et al. (2020), will be considered.

To maintain a similar structure to the underlying work, the calculations will be performed for the year 2009. This year was selected for its high number of RO observations. Furthermore, for parts of the analyses ERA5 data will be used instead of RO data, in order to just compare the validity of the method and not the underlying data itself. The actual wind field components available from ERA5 are subscripted by an o, for original, for example V_o, u_o and v_o, i.e., wind speed, zonal wind and meridional wind, respectively. The analysis focuses especially on the tropical and equatorial region, to emphasize and validate the use of the two wind field approximations.

A.1 Wind field equations

Geostrophic balance equation

The geostrophic zonal and meridional wind components, u_g and v_g, are calculated by equation ((3) and ((4) (e.g., Holton and Hakim, 2012):

$$u_g \simeq -\frac{1}{f(\varphi)R_e}\frac{\partial \Phi}{\partial \varphi} \tag{3}$$

$$v_g \simeq \frac{1}{f(\varphi)R_e cos\varphi}\frac{\partial \Phi}{\partial \lambda} \tag{4}$$

where $f(\varphi)$ describes the Coriolis parameter $f(\varphi) = 2\Omega \sin\varphi$, with the Earth's angular rotation rate $\Omega = 7.2921 \times 10^{-5}$ rad/s, Earth's mean radius $R_e = 6371$ km, the geopotential on isobaric levels Φ, and φ and λ describing the latitude and longitude, respectively. The geopotential Φ can be calculated from $\Phi = \mathrm{Z}\,\mathrm{g}_0$, where Z stands for the geopotential height and $g_0 = 9.80665$ m/s^2 is the standard gravity constant.

Equatorial balance equation

The equatorial balanced zonal and meridional wind components, u_{eb} and v_{eb}, are derived from equations (5 and (6 (e.g., Danzer et al., 2023; Fleming and Chandra, 1989; Scaife et al., 2000):

$$u_{eb} \simeq -\frac{1}{\beta R_e^2}\frac{\partial^2 \Phi}{\partial^2 \varphi} \tag{5}$$

$$v_{eb} \simeq \frac{1}{\beta R_e^2}\frac{\partial^2 \Phi}{\partial \varphi \partial \lambda} \tag{6}$$

where $\beta = 2\Omega/R_e$.

Wind Speed

The wind speed will be calculated by the formulation $V = \sqrt{u^2 + v^2}$, for both methods. The according wind speed V will be indicated by the appropriate subscript for the geostrophic and equatorial balance equation, g and eb, respectively.

A.2 Finite difference method

The introduced approximations include derivatives, which cannot be analytically solved but instead a numerical solution must be found. For this reason different types of finite differences are investigated for the derivative operator $\frac{\partial f(x)}{\partial x}$ and $\frac{\partial^2 f(x)}{\partial x^2}$, those include the forward, backward, central, and central higher-order finite difference. Listed in the following equation ((7) to (10), are the finite differences investigated for the first derivative used in the geostrophic equation, where h is the step size on the numerical grid and $O(h^n)$ is the error, where n describes the order of accuracy.

$$forward: \quad \frac{\partial f(x)}{\partial x} = \frac{f(x+h) - f(x)}{h} + O(h) \tag{7}$$

$$backward: \quad \frac{\partial f(x)}{\partial x} = \frac{f(x) - f(x-h)}{h} + O(h) \tag{8}$$

$$central: \quad \frac{\partial f(x)}{\partial x} = \frac{f(x+h) - f(x-h)}{2h} + O(h^2) \tag{9}$$

$$cental\ O(h^4): \quad \frac{\partial f(x)}{\partial x} = \frac{f(x-2h) - 8f(x-h) + 8f(x+h) - f(x+2h)}{12h} + O(h^4) \tag{10}$$

Equations (11) to (14) show the second derivative finite differences investigated for the equatorial balance equation.

$$forward: \quad \frac{\partial^2 f(x)}{\partial x^2} = \frac{f(x+2h) - 2f(x+h) + f(x)}{h^2} + O(h^2) \tag{11}$$

$$backward: \quad \frac{\partial^2 f(x)}{\partial x^2} = \frac{f(x) - 2f(x-h) + f(x-2h)}{h^2} + O(h^2) \tag{12}$$

$$central: \quad \frac{\partial^2 f(x)}{\partial x^2} = \frac{f(x+h) - 2f(x) + f(x-h)}{h^2} + O(h^2) \tag{13}$$

$$cental\ O(h^4): \quad \frac{\partial^2 f(x)}{\partial x^2} = \frac{-f(x+2h) + 16f(x+h) - 30f(x) + 16f(x-h) - f(x-2h)}{12h^2} + O(h^4) \tag{14}$$

In order to compare the different finite difference methods, a wind field was created for each, following the method in Danzer et al. (2023) and inspected in multiple ways. Figure A.1 compares the central, forward, and backward method for ERA5 data for annual mean values for the year 2009 over the globe for the ±30° latitude sector. The wind field was created from geopotential data from

ERA5 with the already elaborated equations and compared to the original ERA5 winds. One can see that the central finite difference method performs best for all pressure levels, the absolute error is the smallest.

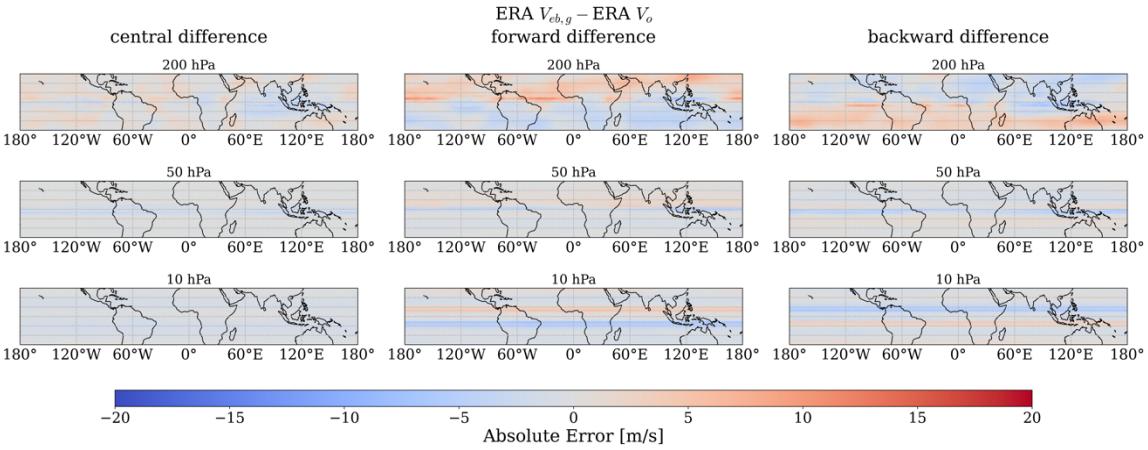

Figure A.1: Comparison of finite difference methods central, forward, and backward for ERA5 data and the annual mean 2009, for three pressure levels (200, 50, 10 hPa).

Furthermore, the central difference is compared to the central difference higher-order O(h^4). Figure A.2 shows only minor differences between the two methods. The results look very similar over all regions and levels. Be aware that the error bar has changed to suit the smaller deviations.

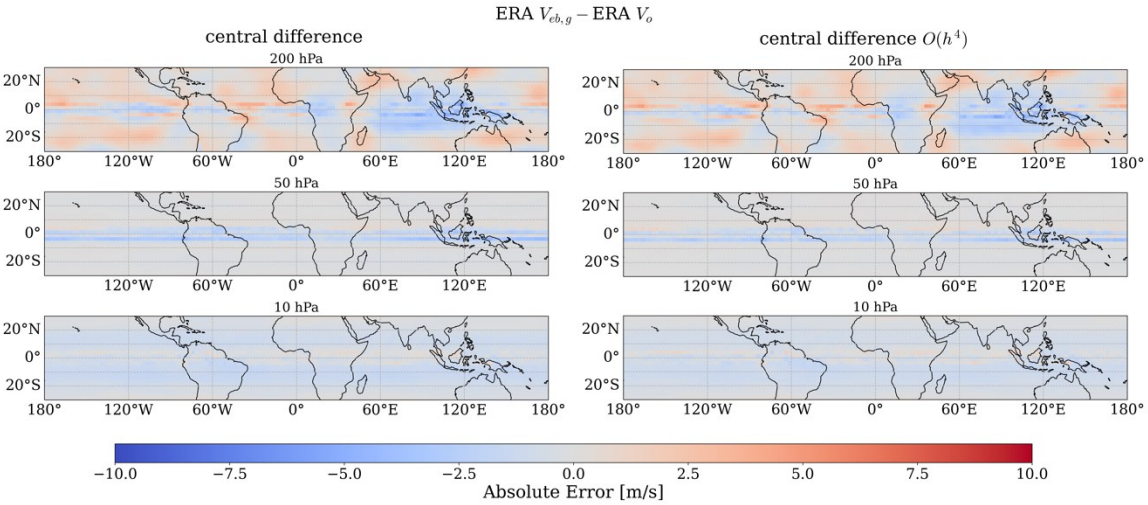

Figure A.2: Comparison of finite difference methods central and central 4th order for ERA5 data and the annual mean 2009, for three pressure levels (200, 50, 10 hPa).

Figure A.3 shows the zonal mean of the derived and original wind field for the equatorial balance equation (left) and the geostrophic equation (right). An indicative wind speed bias threshold of ±2 m/s is introduced (orange dashed lines) to validate the quality of the method. The threshold is equal to the one used in Danzer et al. (2023). In general, the threshold is based on the accuracy

requirements of the WMO, see WMO-OSCAR, 2023 and selected suitable for climate-related winds, with rather strong temporal and spatial averaging.

For the equatorial region one can see that especially for lower pressure levels, the forward and backward method, result in bigger deviations which lie outside the threshold. In comparison, the central and central higher order method are more within the threshold. The results for the geostrophic equations poleward of the equator region looks similar. In general, the methods stay within the threshold except for some deviations of the forward and backward method.

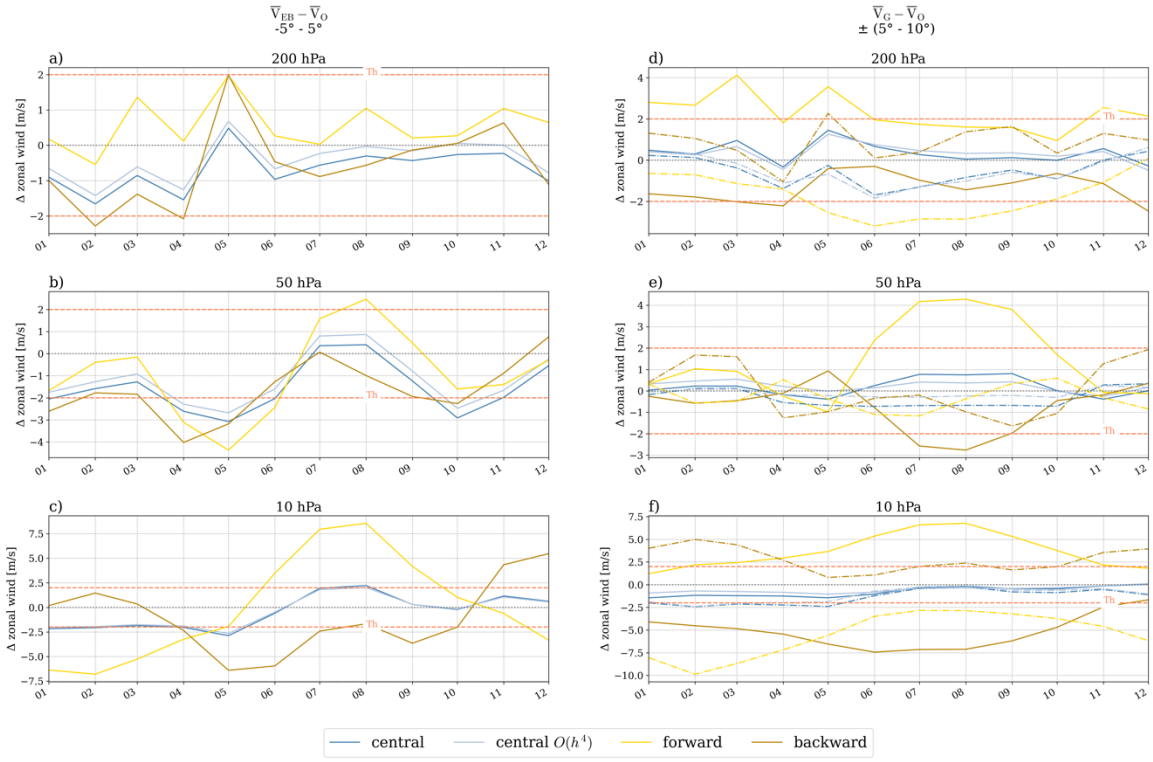

Figure A.3: Comparison of finite difference methods central, forward, backward, and central 4th order for ERA5 data and monthly-mean values 2009. The left column, (a) to (c), shows the equatorial balance equation in its respective equatorial regions ±5° latitude. The right-hand column, (d) to (f) displays the geostrophic wind field from 5° to 10° latitude on each hemisphere. The dash-dot lines indicate the results for the southern hemisphere, the solid lines mark the northern hemisphere results.

The final analysis of the finite difference methods (Figure A.4) is only displayed for the central and central higher order methods but was also assessed for the others. The figure shows the bias from the finite difference method over the tropical latitudes ±10°, over the course of the year 2009 for monthly-mean data. The results of the investigated methods in Figure A.4 are again very similar to one another. The central finite difference method performs ever so slightly better.

Based on this evaluation, the central and central higher-order method provided similar results which clearly outperformed the forward and backward method. Therefore, the simpler solution seems to be the best fit. Furthermore, the central finite difference higher-order considers a wider data interval,

which can be problematic for larger grid sizes. For example the RO data which will be investigated, is binned on a 5° x 5° grid for calculation with the equatorial balance equation. Thus, an 25° slice, or even more, would be necessary to calculate a single datapoint. As the equatorial balance equation is only valid in the equatorial region, applying a central difference higher order could lead to approximation errors. As a result, the central finite difference is selected for derivatives in further investigations, as it is the simpler solution between the two.

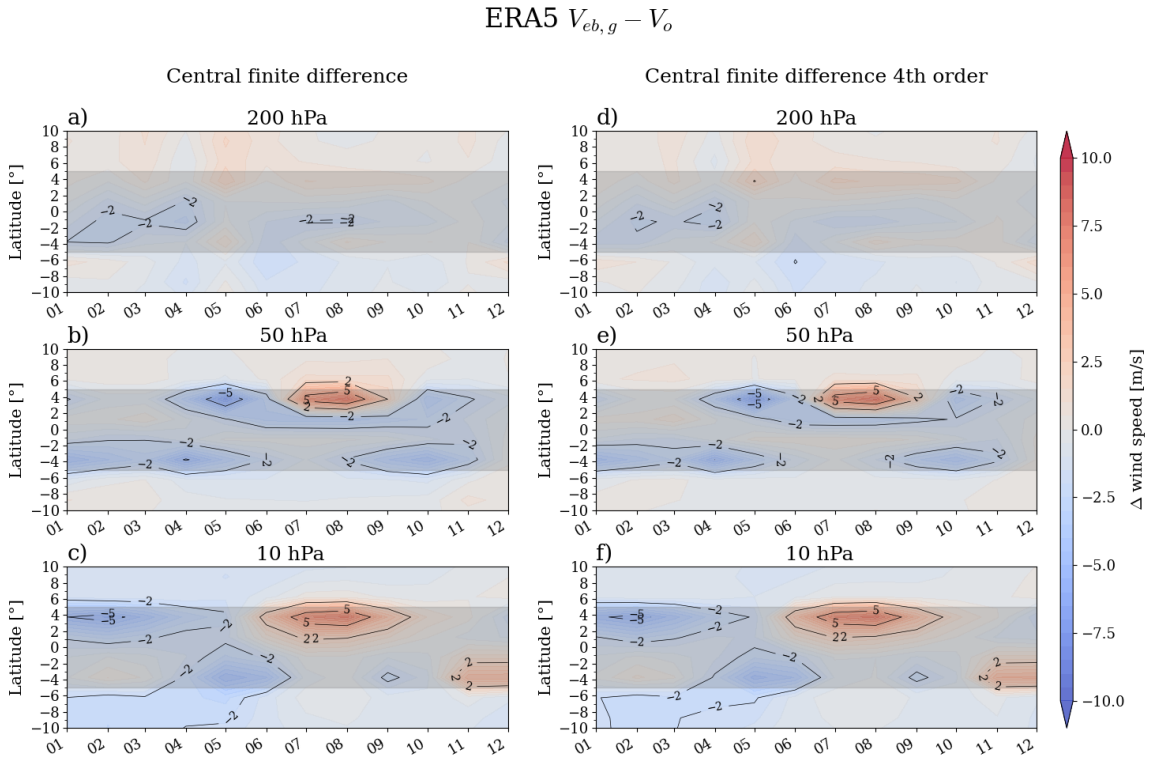

Figure A.4: Comparison of finite difference methods central and central 4th order for ERA5 data over the course of 2009 for monthly-mean data, for three pressure levels (200, 50, 10 hPa). The region of the equatorial balance equation is highlighted with a gray shading.

A.3 Interpolation of the equatorial balance approximation

In the next step, the interpolation method of the equatorial balance approximation was investigated more closely. More specifically, the difference arising from the interpolation of the equatorial balanced wind with the linear and cubic spline interpolation method is compared.

As in the study by Danzer et al. (2023), the geopotential from RO data must be further smoothed in order to get good results from the equatorial balance approximation. Hence, the 2.5° x 2.5° RO data gets transferred onto a 5° x 5° grid via cosine weighted binning before applying the equation. However, in order to create a complete, uniform wind field, these calculated values then must be interpolated back onto the smaller grid.

Figure A.5 shows the difference between the calculated RO wind speed and the ERA5 wind speed for the equatorial region for monthly-mean values in the year 2009. Linear and cubic spline interpolation perform similarly when looking at $\overline{V_{EB}} - \overline{V_O}$, only for the local bias within a grid cell, indicated by $\overline{|V_{EB} - V_O|}$, the linear interpolation performs a bit better. The cubic spline interpolation method reduces the effect of the smoothing, the results are close to the ones from 5° x 5° data. Based on this analysis, the linear interpolation method seems to be the most suitable one.

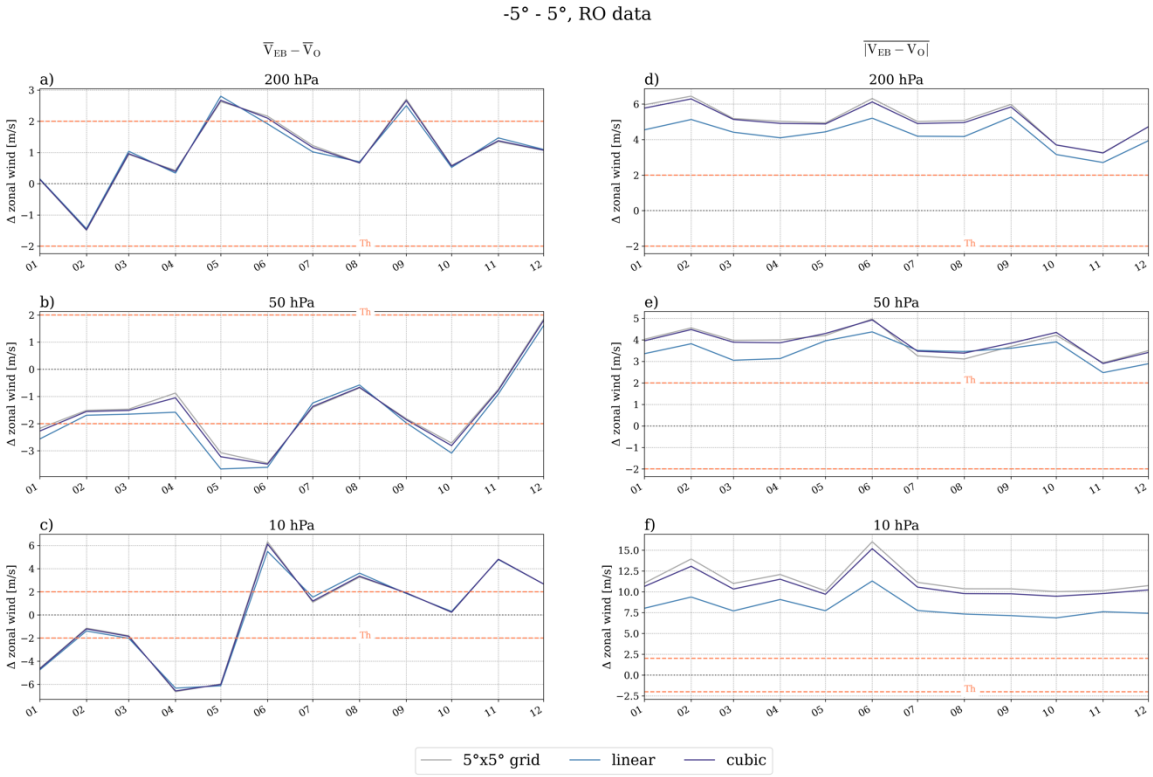

Figure A.5: Bias from the interpolation method, linear versus cubic spline, for RO data. Monthly, zonal mean values for the difference between the calculated wind and ERA5 original wind are plotted over the course of the year 2009. The gray line represents the initial values of the 5° x 5° grid before interpolation.

A.4 Order of calculation

The last step of the wind field analyses inspects the bias in connection to the sequence of operators used. For all analysis so far, the wind field was first calculated and then interpolated, complementary the opposite, as proposed by Healy et al. (2020), interpolation of the data followed by the wind calculations, was performed, and compared. The order sequence, ‘calculation then interpolation’ will be at times referred to as ‘the initial sequence’, the order ‘interpolation then calculation’ as ‘reversed sequence’.

Figure A.6 shows the absolute error of the calculated wind fields versus the original one for both orders of operations. The above defined linear interpolation method for the initial order of calculation (left column) is compared to the reversed calculation sequence, first interpolation then

calculation (right column). For the later one, the cubic spline interpolation method is used, as the subsequently applied central finite difference would make a linear interpolation redundant. From a first glance one can notice that the sequence of operators used has an influence. The bias between the calculated and original wind speed presents different patterns for the two sequences. It appears that the reversed sequence overestimates the winds in comparison to the initial order, although the differences are minor, and an additional figure analysis is needed to make final conclusions.

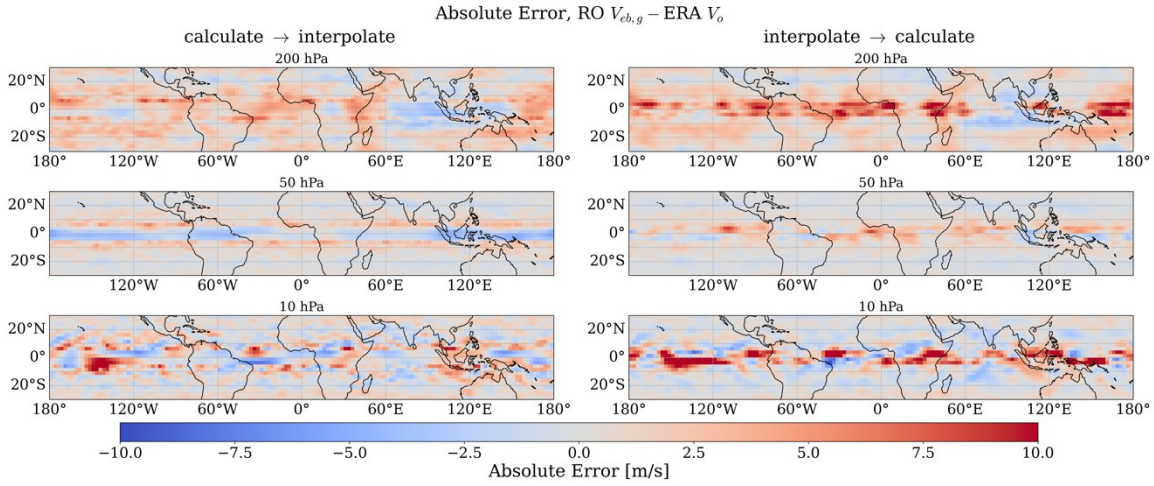

Figure A.6: Absolute error in m/s between the calculated RO and original wind data from ERA5 for the annual mean 2009. The left row shows the results gained from first calculating the wind field and then performing linear interpolation, the right row resembles the reversed sequence using cubic spline interpolation. Both are displayed for multiple pressure levels on a 2.5° x 2.5°grid.

Figure A.7 displays the relative error, linked to the previous one. This graph shows, that although the bias patterns in Figure A.6 vary, the relative error is actually quite small. The reversed method has a stronger error for higher pressure levels. For lower levels the error looks of similar magnitude for both sequences.

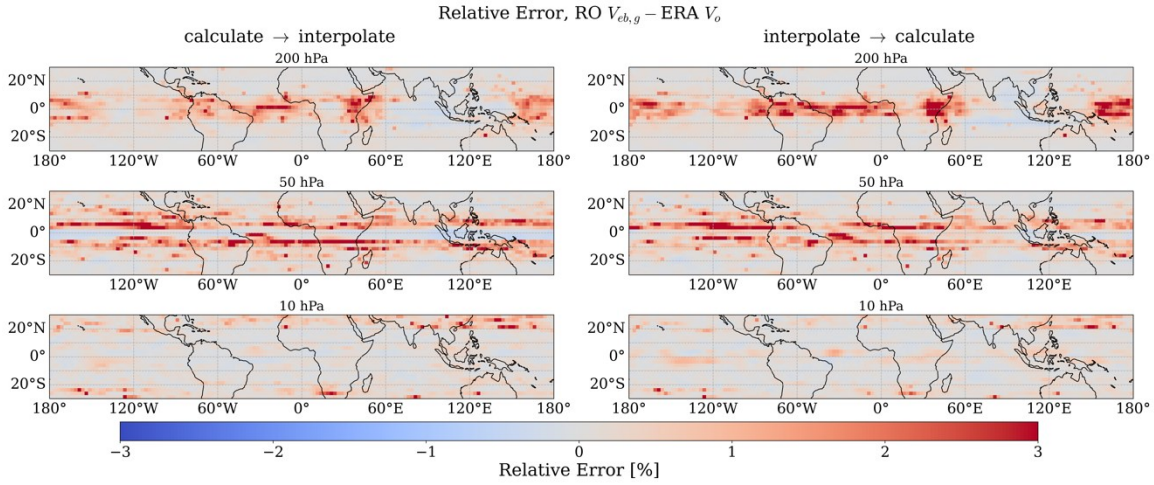

Figure A.7: Relative error in % between the calculated RO and original wind data from ERA5 for the annual mean 2009. The plot is structured as in Figure A.6.

As a final plot for this analysis, Figure A.8, shows the zonal mean (left column) and local bias within a grid cell (right column) for the calculated wind speed for both sequences. For the reversed order, two options are displayed. One shows the results for interpolation onto a 2.5° x 2.5° grid, such as for the initial sequence. The second one is interpolated onto a 0.703° x 5° grid, to allow comparison with the methodology of Healy et al. (2020). From this figure it is clearly visible that while the zonal mean bias provides similar results, with the initial order of Danzer et al. (2023) performing slightly better, the local bias is greater for the reversed order. Indicating that first calculating the winds followed by interpolation yields the best results. As for the reversed sequence itself, Figure A.8 shows that the lower resolution on the latitude axis (0.703° x 5°) results in an overall better performance of this method, compared to the 2.5° x 2.5° grid.

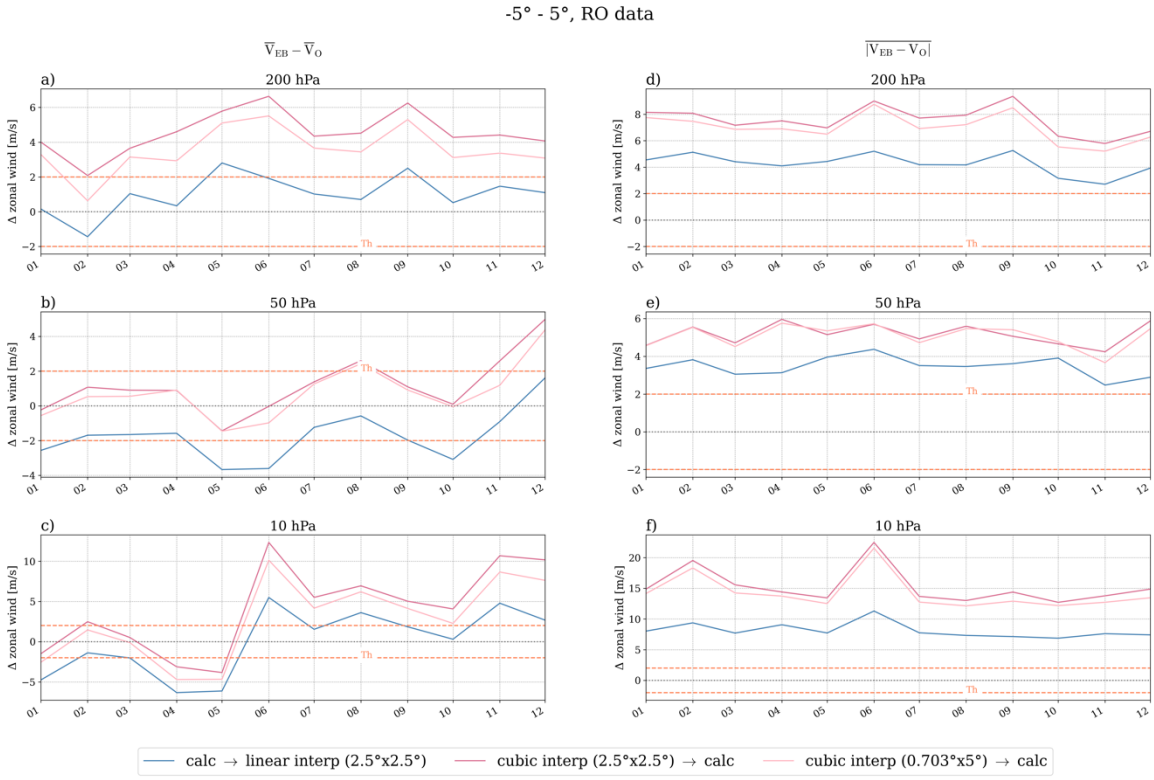

Figure A.8: Bias from the calculation order for the equatorial region for RO data. Monthly, zonal mean values for the difference between the calculated wind and ERA5 original wind are plotted over the course of the year 2009.

The derivation of a wind field was thoroughly investigated in this work. In conclusion, the smallest deviations to the original wind are gained from first calculating the wind field and then applying linear interpolation, using the central finite difference method for the numerical solution of the derivatives. This acquired methodology was used in this thesis to produce a wind field from RO geopotential data, of which in turn the metrics of Hadley cell change were calculated.

B. Lead-lag analysis continued

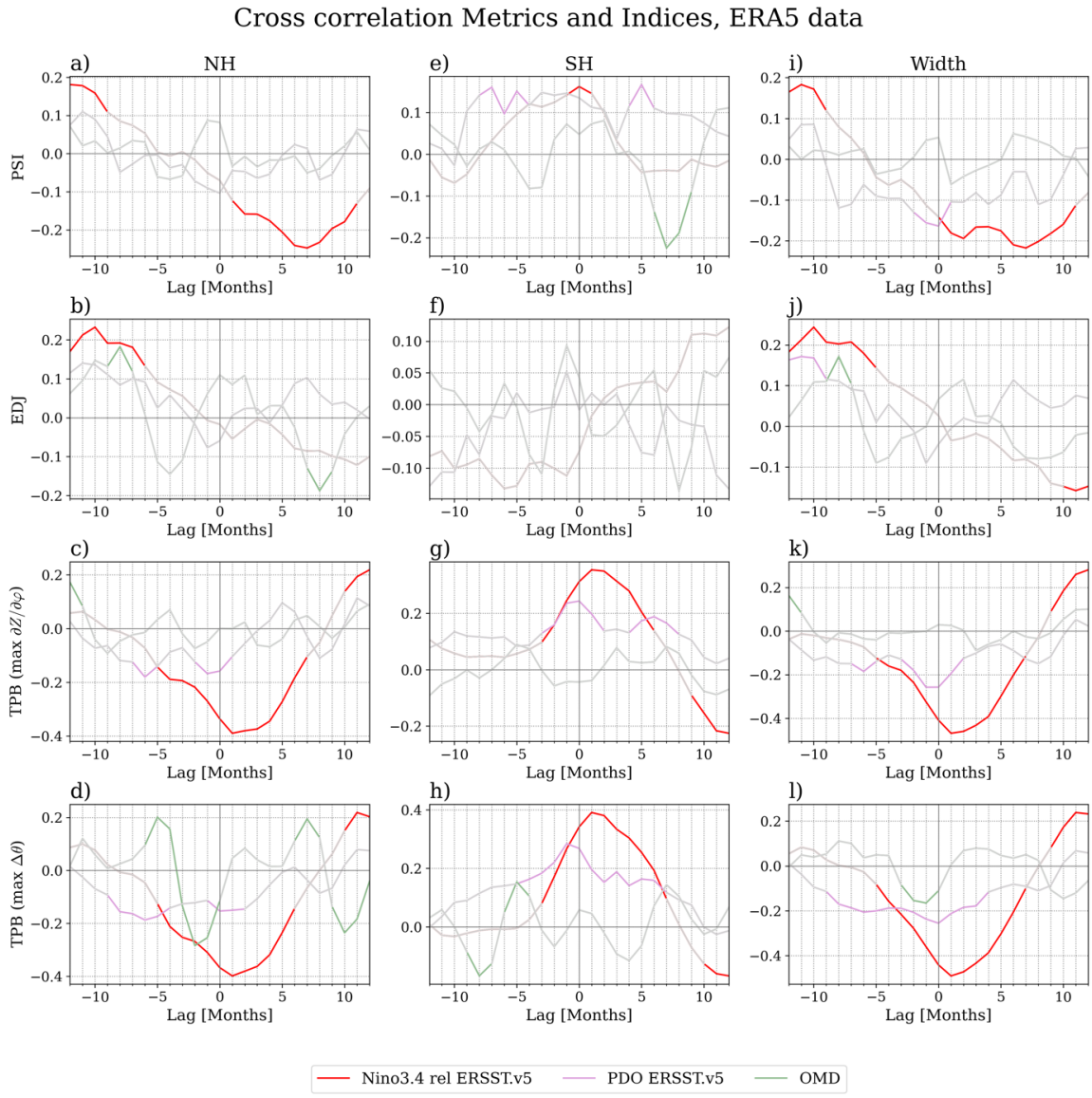

Figure B.1: Cross correlation of the lagged indices for each metric on the northern hemisphere (a-d), southern hemisphere (e-h) and Hadley cell width (i-l). This analysis was performed on ERA5 data for the time period September 2006 to November 2020. The lag correlation span is ±12 months. A positive lag indicates that the index leads the metric, thus the metric lags the index. Correlation values which are not statistically significant at the 95% confidence interval are displayed in a gray color.

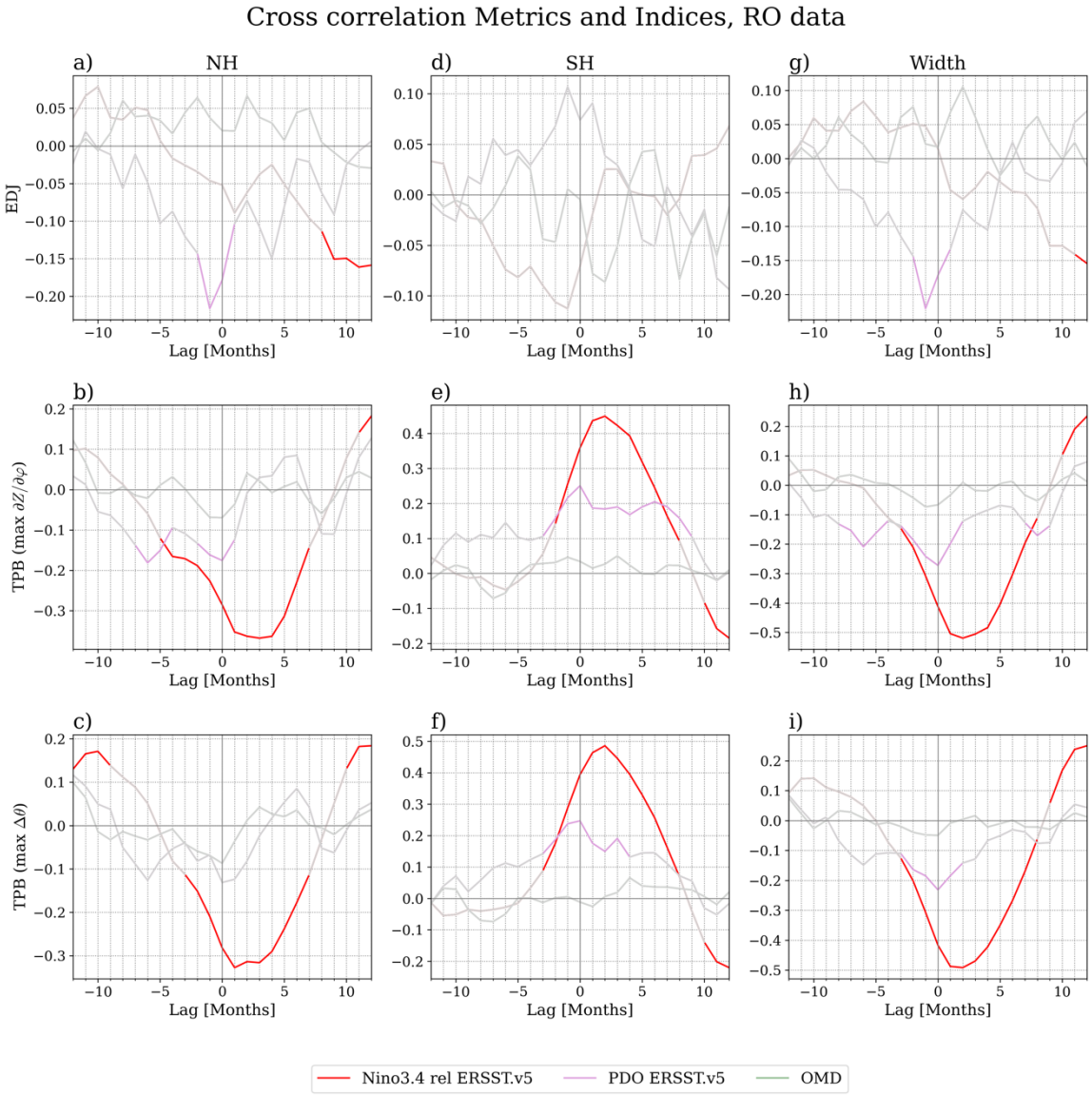

Figure B.2: As in Figure B.1 for RO data over the time period September 2006 to November 2020.

List of figures

List of tables

Bibliography

Adam, O., Grise, K.M., Staten, P., Simpson, I.R., Davis, S.M., Davis, N.A., Waugh, D.W., Birner, T., Ming, A., 2018. The TropD software package (v1): standardized methods for calculating tropical-width diagnostics. Geosci. Model Dev. 11, 4339–4357. https://doi.org/10.5194/gmd-11-4339-2018.

Adam, O., Schneider, T., Harnik, N., 2014. Role of Changes in Mean Temperatures versus Temperature Gradients in the Recent Widening of the Hadley Circulation. J. Clim. 27, 7450–7461. https://doi.org/10.1175/JCLI-D-14-00140.1.

Adames, Á.F., Wallace, J.M., 2017. On the Tropical Atmospheric Signature of El Niño. J. Atmospheric Sci. 74, 1923–1939. https://doi.org/10.1175/JAS-D-16-0309.1.

Allen, R.J., Ajoku, O., 2016. Future aerosol reductions and widening of the northern tropical belt. J. Geophys. Res. Atmospheres 121, 6765–6786. https://doi.org/10.1002/2016JD024803.

Amaya, D.J., Siler, N., Xie, S.-P., Miller, A.J., 2018. The interplay of internal and forced modes of Hadley Cell expansion: lessons from the global warming hiatus. Clim. Dyn. 51, 305–319. https://doi.org/10.1007/s00382-017-3921-5.

Angerer, B., Ladstädter, F., Scherllin-Pirscher, B., Schwärz, M., Steiner, A.K., Foelsche, U., Kirchengast, G., 2017. Quality aspects of the Wegener Center multi-satellite GPS radio occultation record OPSv5.6. Atmospheric Meas. Tech. 10, 4845–4863. https://doi.org/10.5194/amt-10-4845-2017.

Ao, C.O., Hajj, A.J., 2013. Monitoring the width of the tropical belt with GPS radio occultation measurements. Geophys. Res. Lett. 40, 6236–6241. https://doi.org/10.1002/2013GL058203.

Behera, S., Yamagata, T., 2018. Climate Dynamics of ENSO Modoki Phenomena, in: Oxford Research Encyclopedia of Climate Science. https://doi.org/10.1093/acrefore/9780190228620.013.612.

Caballero, R., 2007. Role of eddies in the interannual variability of Hadley cell strength. Geophys. Res. Lett. 34. https://doi.org/10.1029/2007GL030971.

Chandra, S., Fleming, E.L., Schoeberl, M.R., Barnett, J.J., 1990. Monthly mean global climatology of temperature, wind, geopotential height and pressure for 0–120 km. Adv. Space Res. 10, 3–12. https://doi.org/10.1016/0273-1177(90)90230-W.

Chemke, R., Polvani, L.M., 2019. Exploiting the Abrupt 4 × CO2 Scenario to Elucidate Tropical Expansion Mechanisms. J. Clim. 32, 859–875. https://doi.org/10.1175/JCLI-D-18-0330.1.

D'Agostino, R., Lionello, P., Adam, O., Schneider, T., 2017. Factors controlling Hadley circulation changes from the Last Glacial Maximum to the end of the 21st century. Geophys. Res. Lett. 44, 8585–8591. https://doi.org/10.1002/2017GL074533.

Danzer, J., Foelsche, U., Scherllin-Pirscher, B., Schwärz, M., 2014. Influence of changes in humidity on dry temperature in GPS RO climatologies. Atmospheric Meas. Tech. 7, 2883–2896. https://doi.org/10.5194/amt-7-2883-2014.

Danzer, J., Pieler, M., Kirchengast, G., 2023. Closing the gap in the tropics: the added value of radio-occultation data for wind field monitoring across the equator (preprint). Others (Wind, Precipitation, Temperature, etc.)/Remote Sensing/Validation and Intercomparisons. https://doi.org/10.5194/amt-2023-137.

Darrag, M., Jin, S., Calabia, A., Samy, A., 2022. Determination of tropical belt widening using multiple GNSS radio occultation measurements. Ann. Geophys. 40, 359–377. https://doi.org/10.5194/angeo-40-359-2022.

Davis, N., Birner, T., 2017. On the Discrepancies in Tropical Belt Expansion between Reanalyses and Climate Models and among Tropical Belt Width Metrics. J. Clim. 30, 1211–1231.

https://doi.org/10.1175/JCLI-D-16-0371.1.
Davis, N., Birner, T., 2016. Climate Model Biases in the Width of the Tropical Belt. J. Clim. 29, 1935–1954. https://doi.org/10.1175/JCLI-D-15-0336.1.
Davis, N.A., Birner, T., 2022. Eddy-Mediated Hadley Cell Expansion due to Axisymmetric Angular Momentum Adjustment to Greenhouse Gas Forcings. J. Atmospheric Sci. 79, 141–159. https://doi.org/10.1175/JAS-D-20-0149.1.
Davis, N.A., Birner, T., 2013. Seasonal to multidecadal variability of the width of the tropical belt. J. Geophys. Res. Atmospheres 118, 7773–7787. https://doi.org/10.1002/jgrd.50610.
Davis, N.A., Seidel, D.J., Birner, T., Davis, S.M., Tilmes, S., 2016. Changes in the width of the tropical belt due to simple radiative forcing changes in the GeoMIP simulations. Atmospheric Chem. Phys. 16, 10083–10095. https://doi.org/10.5194/acp-16-10083-2016.
Davis, S.M., Rosenlof, K.H., 2012. A Multidiagnostic Intercomparison of Tropical-Width Time Series Using Reanalyses and Satellite Observations. J. Clim. 25, 1061–1078. https://doi.org/10.1175/JCLI-D-11-00127.1.
de Laat, A.T.J., van Weele, M., van der A, R.J., 2017. Onset of Stratospheric Ozone Recovery in the Antarctic Ozone Hole in Assimilated Daily Total Ozone Columns. J. Geophys. Res. Atmospheres 122, 11,880-11,899. https://doi.org/10.1002/2016JD025723.
Dima, I.M., Wallace, J.M., 2003. On the Seasonality of the Hadley Cell. J. Atmospheric Sci. 60, 1522–1527. https://doi.org/10.1175/1520-0469(2003)060<1522:OTSOTH>2.0.CO;2.
Dogar, M.M., 2018. Impact of tropical volcanic eruptions on Hadley circulation using a high-resolution AGCM. Curr. Sci. 114, 1284–1294. https://doi.org/10.18520/cs/v114/i06/1284-1294.
Feng, J., Li, J., 2013. Contrasting Impacts of Two Types of ENSO on the Boreal Spring Hadley Circulation. J. Clim. 26, 4773–4789. https://doi.org/10.1175/JCLI-D-12-00298.1.
Feng, J., Li, J., Jin, F., Liu, Z., Nan, X., Guo, Y., 2016. Contrasting Responses of the Hadley Circulation to Equatorially Asymmetric and Symmetric Meridional Sea Surface Temperature Structures. J. Clim. 29, 8949–8963. https://doi.org/10.1175/JCLI-D-16-0171.1.
Feng, J., Li, J., Jin, F., Zhao, S., Zhu, J., 2018. Relationship between the Hadley Circulation and Different Tropical Meridional SST Structures during Boreal Summer. J. Clim. 31, 6575–6590. https://doi.org/10.1175/JCLI-D-18-0095.1.
Feng, J., Li, J., Xie, F., 2013. Long-Term Variation of the Principal Mode of Boreal Spring Hadley Circulation Linked to SST over the Indo-Pacific Warm Pool. J. Clim. 26, 532–544. https://doi.org/10.1175/JCLI-D-12-00066.1.
Fleming, E.L., Chandra, S., 1989. Equatorial Zonal Wind in the Middle Atmosphere Derived from Geopotential Height and Temperature Data. J. Atmospheric Sci. 46, 860–866. https://doi.org/10.1175/1520-0469(1989)046<0860:EZWITM>2.0.CO;2.
Gleisner, H., Ringer, M.A., Healy, S.B., 2022. Monitoring global climate change using GNSS radio occultation. Npj Clim. Atmospheric Sci. 5, 1–4. https://doi.org/10.1038/s41612-022-00229-7.
Grassi, B., Redaelli, G., Canziani, P.O., Visconti, G., 2012. Effects of the PDO Phase on the Tropical Belt Width. J. Clim. 25, 3282–3290. https://doi.org/10.1175/JCLI-D-11-00244.1.
Grise, K.M., Davis, S.M., Simpson, I.R., Waugh, D.W., Fu, Q., Allen, R.J., Rosenlof, K.H., Ummenhofer, C.C., Karnauskas, K.B., Maycock, A.C., Quan, X.-W., Birner, T., Staten, P.W., 2019. Recent Tropical Expansion: Natural Variability or Forced Response? J. Clim. 32, 1551–1571. https://doi.org/10.1175/JCLI-D-18-0444.1.
Guo, Y.-P., Tan, Z.-M., 2018a. Relationship between El Niño–Southern Oscillation and the Symmetry of the Hadley Circulation: Role of the Sea Surface Temperature Annual Cycle. J. Clim. 31, 5319–5332. https://doi.org/10.1175/JCLI-D-17-0788.1.
Guo, Y.-P., Tan, Z.-M., 2018b. On the Sensitivity of the Relationship Between Hadley Circulation Asymmetry and ENSO in CMIP5 Models. Geophys. Res. Lett. 45, 9253–9259. https://doi.org/10.1029/2018GL079515.
Healy, S.B., Polichtchouk, I., Horányi, A., 2020. Monthly and zonally averaged zonal wind information in the equatorial stratosphere provided by GNSS radio occultation. Q. J. R. Meteorol. Soc. 146, 3612–3621. https://doi.org/10.1002/qj.3870.

Held, I.M., Hou, A.Y., 1980. Nonlinear Axially Symmetric Circulations in a Nearly Inviscid Atmosphere. J. Atmospheric Sci. 37, 515–533. https://doi.org/10.1175/1520-0469(1980)037<0515:NASCIA>2.0.CO;2.

Hersbach, H., Bell, B., Berrisford, P., Hirahara, S., Horányi, A., Muñoz-Sabater, J., Nicolas, J., Peubey, C., Radu, R., Schepers, D., Simmons, A., Soci, C., Abdalla, S., Abellan, X., Balsamo, G., Bechtold, P., Biavati, G., Bidlot, J., Bonavita, M., De Chiara, G., Dahlgren, P., Dee, D., Diamantakis, M., Dragani, R., Flemming, J., Forbes, R., Fuentes, M., Geer, A., Haimberger, L., Healy, S., Hogan, R.J., Hólm, E., Janisková, M., Keeley, S., Laloyaux, P., Lopez, P., Lupu, C., Radnoti, G., de Rosnay, P., Rozum, I., Vamborg, F., Villaume, S., Thépaut, J.-N., 2020. The ERA5 global reanalysis. Q. J. R. Meteorol. Soc. 146, 1999–2049. https://doi.org/10.1002/qj.3803.

Holton, J.R., Hakim, G.J., 2012. An Introduction to Dynamic Meteorology. Academic Press.

Hu, D., Guan, Z., Tian, W., 2019a. Signatures of the Arctic Stratospheric Ozone in Northern Hadley Circulation Extent and Subtropical Precipitation. Geophys. Res. Lett. 46, 12340–12349. https://doi.org/10.1029/2019GL085292.

Hu, D., Guo, Y.-P., Tan, Z.-M., Guan, Z., 2019b. Interannual Relationship between the Boreal Spring Arctic Oscillation and the Northern Hemisphere Hadley Circulation Extent. J. Clim. 32, 4395–4408. https://doi.org/10.1175/JCLI-D-18-0657.1.

Hu, Y., Huang, H., Zhou, C., 2018. Widening and weakening of the Hadley circulation under global warming. Sci. Bull. 63, 640–644. https://doi.org/10.1016/j.scib.2018.04.020.

Huang, B., Thorne, P.W., Banzon, V.F., Boyer, T., Chepurin, G., Lawrimore, J.H., Menne, M.J., Smith, T.M., Vose, R.S., Zhang, H.-M., 2017. Extended Reconstructed Sea Surface Temperature, Version 5 (ERSSTv5): Upgrades, Validations, and Intercomparisons. J. Clim. 30, 8179–8205. https://doi.org/10.1175/JCLI-D-16-0836.1.

IPCC, 2021. Summary for Policymakers. In: Climate change 2021: The Physical Science Basis. Contribution of Working Group I to the Sixth Assessment Report of the Intergovernmental Panel on Climate Change. Intergovernmental Panel on Climate Change.

Johnson, N.C., Kosaka, Y., 2016. The impact of eastern equatorial Pacific convection on the diversity of boreal winter El Niño teleconnection patterns. Clim. Dyn. 47, 3737–3765. https://doi.org/10.1007/s00382-016-3039-1.

Kang, S.M., Polvani, L.M., 2011. The Interannual Relationship between the Latitude of the Eddy-Driven Jet and the Edge of the Hadley Cell. J. Clim. 24, 563–568. https://doi.org/10.1175/2010JCLI4077.1.

Kang, S.M., Polvani, L.M., Fyfe, J.C., Sigmond, M., 2011. Impact of Polar Ozone Depletion on Subtropical Precipitation. Science 332, 951–954. https://doi.org/10.1126/science.1202131.

Kim, H., Lee, S., 2004. The Wave–Zonal Mean Flow Interaction in the Southern Hemisphere. J. Atmospheric Sci. 61, 1055–1067. https://doi.org/10.1175/1520-0469(2004)061<1055:TWMFII>2.0.CO;2.

Kim, Y.-H., Min, S.-K., Son, S.-W., Choi, J., 2017. Attribution of the local Hadley cell widening in the Southern Hemisphere. Geophys. Res. Lett. 44, 1015–1024. https://doi.org/10.1002/2016GL072353.

Kursinski, E.R., Hajj, G.A., Schofield, J.T., Linfield, R.P., Hardy, K.R., 1997. Observing Earth's atmosphere with radio occultation measurements using the Global Positioning System. J. Geophys. Res. Atmospheres 102, 23429–23465. https://doi.org/10.1029/97JD01569.

Li, Y., Xie, S.-P., Lian, T., Zhang, G., Feng, J., Ma, J., Peng, Q., Wang, W., Hou, Y., Li, X., 2023. Interannual Variability of Regional Hadley Circulation and El Niño Interaction. Geophys. Res. Lett. 50, e2022GL102016. https://doi.org/10.1029/2022GL102016.

Lu, J., Chen, G., Frierson, D.M.W., 2008. Response of the Zonal Mean Atmospheric Circulation to El Niño versus Global Warming. J. Clim. 21, 5835–5851. https://doi.org/10.1175/2008JCLI2200.1.

Lu, J., Deser, C., Reichler, T., 2009. Cause of the widening of the tropical belt since 1958. Geophys. Res. Lett. 36. https://doi.org/10.1029/2008GL036076.

Lu, X., Zhang, L., Zhao, Y., Jacob, D.J., Hu, Y., Hu, L., Gao, M., Liu, X., Petropavlovskikh, I., McClure-Begley, A., Querel, R., 2019. Surface and tropospheric ozone trends in the Southern Hemisphere since 1990: possible linkages to poleward expansion of the Hadley

circulation. Sci. Bull. 64, 400–409. https://doi.org/10.1016/j.scib.2018.12.021.
Luan, L., Staten, P.W., Ao, C.O., Fu, Q., 2020. Seasonal and Annual Changes of the Regional Tropical Belt in GPS-RO Measurements and Reanalysis Datasets. J. Clim. 33, 4083–4094. https://doi.org/10.1175/JCLI-D-19-0671.1.
Lucas, C., Nguyen, H., 2015. Regional characteristics of tropical expansion and the role of climate variability. J. Geophys. Res. Atmospheres 120, 6809–6824. https://doi.org/10.1002/2015JD023130.
Lucas, C., Nguyen, H., Timbal, B., 2012. An observational analysis of Southern Hemisphere tropical expansion. J. Geophys. Res. Atmospheres 117. https://doi.org/10.1029/2011JD017033.
Ma, J., Li, J., 2008. The principal modes of variability of the boreal winter Hadley cell. Geophys. Res. Lett. 35. https://doi.org/10.1029/2007GL031883.
Maher, P., Kelleher, M.E., Sansom, P.G., Methven, J., 2020. Is the subtropical jet shifting poleward? Clim. Dyn. 54, 1741–1759. https://doi.org/10.1007/s00382-019-05084-6.
Mantsis, D.F., Sherwood, S., Allen, R., Shi, L., 2017. Natural variations of tropical width and recent trends. Geophys. Res. Lett. 44, 3825–3832. https://doi.org/10.1002/2016GL072097.
Mantua, N.J., Hare, S.R., Zhang, Y., Wallace, J.M., Francis, R.C., 1997. A Pacific Interdecadal Climate Oscillation with Impacts on Salmon Production*. Bull. Am. Meteorol. Soc. 78, 1069–1080. https://doi.org/10.1175/1520-0477(1997)078<1069:APICOW>2.0.CO;2.
Martin, E.R., Homeyer, C.R., McKinzie, R.A., McCarthy, K.M., Xian, T., 2020. Regionally Varying Assessments of Upper-Level Tropical Width in Reanalyses and CMIP5 Models Using a Tropopause Break Metric. J. Clim. 33, 5885–5903. https://doi.org/10.1175/JCLI-D-19-0629.1.
Meng, L., Liu, J., Tarasick, D.W., Randel, W.J., Steiner, A.K., Wilhelmsen, H., Wang, L., Haimberger, L., 2021. Continuous rise of the tropopause in the Northern Hemisphere over 1980–2020. Sci. Adv. 7, eabi8065. https://doi.org/10.1126/sciadv.abi8065.
Menzel, M.E., Waugh, D., Grise, K., 2019. Disconnect Between Hadley Cell and Subtropical Jet Variability and Response to Increased CO2. Geophys. Res. Lett. 46, 7045–7053. https://doi.org/10.1029/2019GL083345.
Menzel, M.E., Waugh, D.W., Orbe, C., 2023. Connections between Upper Tropospheric and Lower Stratospheric Circulation Responses to Increased CO2. J. Clim. 36, 4101–4112. https://doi.org/10.1175/JCLI-D-22-0851.1.
Menzel, M.E., Waugh, D.W., Wu, Z., Reichler, T., 2024. Replicating the Hadley cell edge and subtropical jet latitude disconnect in idealized atmospheric models. Weather Clim. Dyn. 5, 251–261. https://doi.org/10.5194/wcd-5-251-2024.
Min, S.-K., Son, S.-W., 2013. Multimodel attribution of the Southern Hemisphere Hadley cell widening: Major role of ozone depletion. J. Geophys. Res. Atmospheres 118, 3007–3015. https://doi.org/10.1002/jgrd.50232.
Newman, M., Alexander, M.A., Ault, T.R., Cobb, K.M., Deser, C., Lorenzo, E.D., Mantua, N.J., Miller, A.J., Minobe, S., Nakamura, H., Schneider, N., Vimont, D.J., Phillips, A.S., Scott, J.D., Smith, C.A., 2016. The Pacific Decadal Oscillation, Revisited. J. Clim. 29, 4399–4427. https://doi.org/10.1175/JCLI-D-15-0508.1.
Nguyen, H., Evans, A., Lucas, C., Smith, I., Timbal, B., 2013. The Hadley Circulation in Reanalyses: Climatology, Variability, and Change. J. Clim. 26, 3357–3376. https://doi.org/10.1175/JCLI-D-12-00224.1.
Nimac, I., Danzer, J., Kirchengast, G., 2024. The added value and potential of long-term radio occultation data for climatological wind field monitoring. https://doi.org/10.5194/amt-2024-59.
Nimac, I., Danzer, J., Kirchengast, G., 2023. Validation of the geostrophic approximation using ERA5 and the potential of long-term radio occultation data for supporting wind field monitoring. Atmospheric Meas. Tech. Discuss. 1–24. https://doi.org/10.5194/amt-2023-100.
Oort, A.H., Rasmusson, E.M., 1970. ON THE ANNUAL VARIATION OF THE MONTHLY MEAN MERIDIONAL CIRCULATION. Mon. Weather Rev. 98, 423–442. https://doi.org/10.1175/1520-0493(1970)098<0423:OTAVOT>2.3.CO;2.

Polvani, L.M., Previdi, M., Deser, C., 2011a. Large cancellation, due to ozone recovery, of future Southern Hemisphere atmospheric circulation trends. Geophys. Res. Lett. 38. https://doi.org/10.1029/2011GL046712.

Polvani, L.M., Waugh, D.W., Correa, G.J.P., Son, S.-W., 2011b. Stratospheric Ozone Depletion: The Main Driver of Twentieth-Century Atmospheric Circulation Changes in the Southern Hemisphere. J. Clim. 24, 795–812. https://doi.org/10.1175/2010JCLI3772.1.

Rasmusson, E.M., Carpenter, T.H., 1982. Variations in Tropical Sea Surface Temperature and Surface Wind Fields Associated with the Southern Oscillation/El Niño. Mon. Weather Rev. 110, 354–384. https://doi.org/10.1175/1520-0493(1982)110<0354:VITSST>2.0.CO;2.

Rayner, N.A., Parker, D.E., Horton, E.B., Folland, C.K., Alexander, L.V., Rowell, D.P., Kent, E.C., Kaplan, A., 2003. Global analyses of sea surface temperature, sea ice, and night marine air temperature since the late nineteenth century. J. Geophys. Res. Atmospheres 108, 2002JD002670. https://doi.org/10.1029/2002JD002670.

Rollings, M., Merlis, T.M., 2021. The Observed Relationship between Pacific SST Variability and Hadley Cell Extent Trends in Reanalyses. J. Clim. 34, 2511–2527. https://doi.org/10.1175/JCLI-D-20-0410.1.

Santer, B.D., Wehner, M.F., Wigley, T.M.L., Sausen, R., Meehl, G.A., Taylor, K.E., Ammann, C., Arblaster, J., Washington, W.M., Boyle, J.S., Brüggemann, W., 2003. Contributions of Anthropogenic and Natural Forcing to Recent Tropopause Height Changes. Science 301, 479–483. https://doi.org/10.1126/science.1084123.

Scaife, A.A., Austin, J., Butchart, N., Pawson, S., Keil, M., Nash, J., James, I.N., 2000. Seasonal and interannual variability of the stratosphere diagnosed from UKMO TOVS analyses. Q. J. R. Meteorol. Soc. 126, 2585–2604. https://doi.org/10.1002/qj.49712656812.

Scherllin-Pirscher, B., Steiner, A.K., Kirchengast, G., 2014. Deriving dynamics from GPS radio occultation: Three-dimensional wind fields for monitoring the climate. Geophys. Res. Lett. 41, 7367–7374. https://doi.org/10.1002/2014GL061524.

Scherllin-Pirscher, B., Steiner, A.K., Kirchengast, G., Schwärz, M., Leroy, S.S., 2017. The power of vertical geolocation of atmospheric profiles from GNSS radio occultation. J. Geophys. Res. Atmospheres 122, 1595–1616. https://doi.org/10.1002/2016JD025902.

Schneider, T., 2006. The General Circulation of the Atmosphere. Annu. Rev. Earth Planet. Sci. 34, 655–688. https://doi.org/10.1146/annurev.earth.34.031405.125144.

Schwendike, J., Govekar, P., Reeder, M.J., Wardle, R., Berry, G.J., Jakob, C., 2014. Local partitioning of the overturning circulation in the tropics and the connection to the Hadley and Walker circulations. J. Geophys. Res. Atmospheres 119, 1322–1339. https://doi.org/10.1002/2013JD020742.

Seidel, D.J., Randel, W.J., 2007. Recent widening of the tropical belt: Evidence from tropopause observations. J. Geophys. Res. Atmospheres 112. https://doi.org/10.1029/2007JD008861.

Seidl, R., Rammer, W., 2016. Climate change amplifies the interactions between wind and bark beetle disturbances in forest landscapes. Landsc. Ecol. 1485–1498. https://doi.org/10.1007/s10980-016-0396-4.

Seo, K.-H., Yoon, S.-P., Lu, J., Hu, Y., Staten, P.W., Frierson, D.M.W., 2023. What controls the interannual variation of Hadley cell extent in the Northern Hemisphere: physical mechanism and empirical model for edge variation. Npj Clim. Atmospheric Sci. 6, 1–12. https://doi.org/10.1038/s41612-023-00533-w.

Son, S.-W., Gerber, E.P., Perlwitz, J., Polvani, L.M., Gillett, N.P., Seo, K.-H., Eyring, V., Shepherd, T.G., Waugh, D., Akiyoshi, H., Austin, J., Baumgaertner, A., Bekki, S., Braesicke, P., Brühl, C., Butchart, N., Chipperfield, M.P., Cugnet, D., Dameris, M., Dhomse, S., Frith, S., Garny, H., Garcia, R., Hardiman, S.C., Jöckel, P., Lamarque, J.F., Mancini, E., Marchand, M., Michou, M., Nakamura, T., Morgenstern, O., Pitari, G., Plummer, D.A., Pyle, J., Rozanov, E., Scinocca, J.F., Shibata, K., Smale, D., Teyssèdre, H., Tian, W., Yamashita, Y., 2010. Impact of stratospheric ozone on Southern Hemisphere circulation change: A multimodel assessment. J. Geophys. Res. Atmospheres 115. https://doi.org/10.1029/2010JD014271.

Staten, P., Lu, J., Grise, K., Davis, S., Birner, T., 2018. Re-examining tropical expansion. Nat. Clim. Change 8. https://doi.org/10.1038/s41558-018-0246-2.

Staten, P.W., Grise, K.M., Davis, S.M., Karnauskas, K., Davis, N., 2019. Regional Widening of Tropical Overturning: Forced Change, Natural Variability, and Recent Trends. J. Geophys. Res. Atmospheres 124, 6104–6119. https://doi.org/10.1029/2018JD030100.

Staten, P.W., Reichler, T., 2014. On the ratio between shifts in the eddy-driven jet and the Hadley cell edge. Clim. Dyn. 42, 1229–1242. https://doi.org/10.1007/s00382-013-1905-7.

Steiner, A.K., Ladstädter, F., Ao, C.O., Gleisner, H., Ho, S.-P., Hunt, D., Schmidt, T., Foelsche, U., Kirchengast, G., Kuo, Y.-H., Lauritsen, K.B., Mannucci, A.J., Nielsen, J.K., Schreiner, W., Schwärz, M., Sokolovskiy, S., Syndergaard, S., Wickert, J., 2020. Consistency and structural uncertainty of multi-mission GPS radio occultation records. Atmospheric Meas. Tech. 13, 2547–2575. https://doi.org/10.5194/amt-13-2547-2020.

Thompson, D.W.J., Wallace, J.M., 2000. Annular Modes in the Extratropical Circulation. Part I: Month-to-Month Variability. J. Clim. 13, 1000–1016. https://doi.org/10.1175/1520-0442(2000)013<1000:AMITEC>2.0.CO;2.

van Oldenborgh, G.J., Hendon, H., Stockdale, T., L'Heureux, M., Perez, E.C. de, Singh, R., Aalst, M. van, 2021. Defining El Niño indices in a warming climate. Environ. Res. Lett. 16, 044003. https://doi.org/10.1088/1748-9326/abe9ed.

Verkhoglyadova, O.P., Leroy, S.S., Ao, C.O., 2014. Estimation of Winds from GPS Radio Occultations. J. Atmospheric Ocean. Technol. 31, 2451–2461. https://doi.org/10.1175/JTECH-D-14-00061.1.

Walker, G., 1924. Correlations in seasonal variations of weather. VIII, A further study of world weather. Men Indian Meteor Dept 24, 275–332.

Wallace, J.M., Hobbs, P.V., 2006. Atmospheric science: an introductory survey, 2nd ed. ed, International geophysics series. Academic press, Amsterdam Paris.

Wang, C., Deser, C., Yu, J.-Y., DiNezio, P., Clement, A., 2017. El Niño and Southern Oscillation (ENSO): A Review, in: Glynn, P.W., Manzello, D.P., Enochs, I.C. (Eds.), Coral Reefs of the Eastern Tropical Pacific: Persistence and Loss in a Dynamic Environment. Springer Netherlands, Dordrecht, pp. 85–106. https://doi.org/10.1007/978-94-017-7499-4_4.

Ward, B., Pausata, F.S.R., Maher, N., 2021. The sensitivity of the El Niño–Southern Oscillation to volcanic aerosol spatial distribution in the MPI Grand Ensemble. Earth Syst. Dyn. 12, 975–996. https://doi.org/10.5194/esd-12-975-2021.

Waugh, D.W., Grise, K.M., Seviour, W.J.M., Davis, S.M., Davis, N., Adam, O., Son, S.-W., Simpson, I.R., Staten, P.W., Maycock, A.C., Ummenhofer, C.C., Birner, T., Ming, A., 2018. Revisiting the Relationship among Metrics of Tropical Expansion. J. Clim. 31, 7565–7581. https://doi.org/10.1175/JCLI-D-18-0108.1.

Wilhelmsen, H., Ladstädter, F., Schmidt, T., Steiner, A.K., 2020. Double Tropopauses and the Tropical Belt Connected to ENSO. Geophys. Res. Lett. 47, e2020GL089027. https://doi.org/10.1029/2020GL089027.

Wolter, K., Timlin, M.S., 2011. El Niño/Southern Oscillation behaviour since 1871 as diagnosed in an extended multivariate ENSO index (MEI.ext). Int. J. Climatol. 31, 1074–1087. https://doi.org/10.1002/joc.2336.

Wolter, K., Timlin, M.S., 1998. Measuring the strength of ENSO events: How does 1997/98 rank? Weather 53, 315–324. https://doi.org/10.1002/j.1477-8696.1998.tb06408.x.

Wolter, K., Timlin, M.S., 1993. Monitoring ENSO in COADS with a seasonally adjusted principal component index. Aper Present. Proc 17th Clim. Diagn. Workshop Norman OK.

World Meteorological Organization, 2022. Scientific Assessment of Ozone Depletion: 2022 (No. 278), GAW Report. Geneva.

World Meteorological Organization, 1957. Meteorology—A three-dimensional science: Second session of the commission for aerology. WMO Bull. 4, 134–138.

Xian, T., Xia, J., Wei, W., Zhang, Z., Wang, R., Wang, L.-P., Ma, Y.-F., 2021. Is Hadley Cell Expanding? Atmosphere 12, 1699. https://doi.org/10.3390/atmos12121699.

Zeng, J., Sokolovskiy, S., Schreiner, W., Hunt, D., 2019. Representation of vertical atmospheric structures by radio occultation observations in the UTLS: comparison to high resolution radiosonde profiles. J. Atmospheric Ocean. Technol. 36. https://doi.org/10.1175/JTECH-D-18-0105.1.

Zhang, T., Hoell, A., Perlwitz, J., Eischeid, J., Murray, D., Hoerling, M., Hamill, T.M., 2019.

Towards Probabilistic Multivariate ENSO Monitoring. Geophys. Res. Lett. 46, 10532–10540. https://doi.org/10.1029/2019GL083946.

Zhang, Y., Wallace, J.M., Battisti, D.S., 1997. ENSO-like Interdecadal Variability: 1900–93. J. Clim. 10, 1004–1020. https://doi.org/10.1175/1520-0442(1997)010<1004:ELIV>2.0.CO;2.

Zhao, X., Allen, R.J., Wood, T., Maycock, A.C., 2020. Tropical Belt Width Proportionately More Sensitive to Aerosols Than Greenhouse Gases. Geophys. Res. Lett. 47, e2019GL086425. https://doi.org/10.1029/2019GL086425.

Zhou, C., Lu, J., Hu, Y., Zelinka, M.D., 2020. Responses of the Hadley Circulation to Regional Sea Surface Temperature Changes. J. Clim. 33, 429–441. https://doi.org/10.1175/JCLI-D-19-0315.1.

Zhou, W., Xie, S.-P., Yang, D., 2019. Enhanced equatorial warming causes deep-tropical contraction and subtropical monsoon shift. Nat. Clim. Change 9, 834–839. https://doi.org/10.1038/s41558-019-0603-9.

Zurita-Gotor, P., Álvarez-Zapatero, P., 2018. Coupled Interannual Variability of the Hadley and Ferrel Cells. J. Clim. 31, 4757–4773. https://doi.org/10.1175/JCLI-D-17-0752.1.